MODELLING OF PHASE TRANSFORMATIONS IN HOT-ROLLED STEELS

by

Sally Victoria Parker

Queens' College

Cambridge

A dissertation submitted for the degree of

Doctor of Philosophy,

at the University of Cambridge,

September 1997

"Twenty-five,
Don't recall a time I felt this alive."

— *The Boo Radleys*

"Now the stars are burning bright,
Like some mystery uncovered.
I'll keep moving through the dark,
With you in my heart,
My blood brother."

— *Bruce Springsteen*

Preface

This dissertation is submitted for the degree of Doctor of Philosophy at the University of Cambridge. The research described in this dissertation was conducted under the supervision of Dr. H. K. D. H. Bhadeshia in the Department of Materials Science and Metallurgy, Cambridge, between October 1994 and September 1997. This work is to the best of my knowledge original, except where acknowledgement and reference is made to previous work. Neither this, nor any substantially similar dissertation has been or is being submitted for any degree, diploma or other qualification at this, or any other, university. This dissertation contains less than 60,000 words.

Sally Parker

September 1997

Acknowledgements

I would like to thank Professors A.H. Windle and C.J. Humphreys for the provision of laboratory facilities in the Department of Materials Science and Metallurgy at the University of Cambridge.

I am very grateful to my supervisor, Dr. Harry Bhadeshia, who, as always, was a source of boundless enthusiasm, knowledge and encouragement. I would like to thank the past and present members of the Phase Transformations Group over the last three years, especially Mike Lord, Dr. Joe Robson and Dr. Steve Jones, for their help and friendship.

I am indebted to British Steel plc and Dr. K. N. Melton, Research Director, Swinden Technology Centre for the opportunity to undertake this research, as part of a three year project supported by the European Coal and Steel Community (ECSC, Committee D3: Physical Metallurgy of Rolling and Finishing). In particular, special thanks are due to Dr. Andy Howe and Dr. Peter Morris for many stimulating discussions throughout this work, and to Ron Beckitt, Harry Wall and colleagues for assistance with the quantitative metallography.

I would also like to thank the ECSC project partners, led by Professor Sybrand van der Zwaag at the Technical University of Delft; Mr. Tom Hoogendoorn at Hoogovens Groep BV in the Netherlands; Dr. Isabel Guitiérrez at CEIT, San Sebastian; Dr. Carlos Garçia de Andrés at CENIM, Madrid and Dr. Ettore Anelli at CSM, Rome, for the provision of experimental data and helpful feedback regarding the modelling work.

Finally, I would like to express my thanks to my family for their continual support. And to my Queens' College friends of the last 7 wonderful years – Ed, Lynette, Steve, Maria, Chris and Anne-Marie: *"So no-one told you life was gonna be this way."*

Abstract

The microstructure and mechanical properties of a hot-rolled steel depend upon its composition and its thermomechanical history. The purpose of the work presented in this thesis was to predict the effect of changes in composition (C, Mn, Si,...), cooling rate and austenite grain structure on the microstructure, to provide a tool for the design of improved steel products.

As austenite is cooled from a high temperature it can transform into a variety of phases as a function of the undercooling below the equilibrium temperature. These include allotriomorphic ferrite, Widmanstätten ferrite, pearlite, bainite and martensite. The nucleation and growth of each of these transformation products has been treated quantitatively using fundamental metallurgical theory. The only fitting parameters are those which are currently impossible to determine experimentally or theoretically, and are connected with the nucleation process. The interfacial energies, shape and site density are unknown at the nucleation stage and have been determined by comparing theory and experimental data. These parameters, within the limits of experimental error, are intended to apply to the whole class of hot-rolled steels.

Using a recent method for treating reactions which occur simultaneously, all of the important transformations have been incorporated into one grand model which properly accounts for mutual interactions and impingement effects.

It has been possible to predict a vast array of published and newly measured experimental data in a variety of forms. This includes the ferrite grain size, transformation-start temperatures and the evolution of volume fraction as a function of time, temperature, austenite state and chemical composition.

Contents

Nomenclature List

$a_C^\alpha\{x\}$	activity of carbon in ferrite evaluated at the composition x
$a_C^\gamma\{x\}$	activity of carbon in austenite evaluated at the composition x
$a_{Fe}^\alpha\{x\}$	activity of iron in ferrite evaluated at the composition x
$a_{Fe}^\gamma\{\mathrm{x}\}$	activity of iron in austenite evaluated at the composition x
A_{cm}	equilibrium $\gamma/\gamma+$ Fe_3C phase boundary
Ae_1	equilibrium $\gamma+\alpha/\alpha+$ Fe_3C phase boundary
Ae_3	equilibrium $\gamma/\gamma+\alpha$ phase boundary
Ae_3'	paraequilibrium $\gamma/\gamma+\alpha$ phase boundary
b	magnitude of Burgers vector of dislocation
B_s	bainite transformation start temperature
d_A	ASTM austenite grain size
dO_α^e	change in extended area of allotriomorphic ferrite on a plane (m^2)
dV_α	change in actual volume of allotriomorphic ferrite (m^3)
dV_α^e	change in extended volume of allotriomorphic ferrite (m^3)
d_α	allotriomorphic ferrite grain size (μm)
d_γ	austenite grain size (μm)
$\overline{D}$	weighted average diffusivity of carbon in austenite ($m^2\ s^{-1}$)
D_X^b	boundary diffusion coefficient of a substitutional solute X in austenite ($m^2\ s^{-1}$)
D_C	diffusivity of carbon in austenite ($m^2\ s^{-1}$)
D_C^v	volume diffusion coefficient of carbon in austenite ($m^2\ s^{-1}$)
E_{AA}, E_{AB}, E_{BB}	interatomic bond energies for $A-A$, $A-B$ and $B-B$ bonds (J)
G	molar Gibbs free energy (J mol^{-1})
G'	Gibbs free energy of whole system (J)
G^*	critical activation free energy barrier for nucleation (J)
G_f^*, G_e^*, G_c^*	critical activation energy barriers for nucleation on grain boundary faces, edges and corners (J)
G_o^*	activation energy for a dislocation to glide from one equilibrium

	position to another (J)
G_F	free energy of stacking fault plane per unit area (J m^{-2})
G_N	universal nucleation function for displacive nucleation (J mol^{-1})
G_p^b	boundary diffusion-controlled growth rate of pearlite (m s^{-1})
G_p^v	volume diffusion-controlled growth rate of pearlite (m s^{-1})
G_α	growth rate of α phase
G^α	free energy of ferrite (J mol^{-1})
G^γ	free energy of austenite (J mol^{-1})
$G^{\gamma'}$	free energy of enriched austenite (J mol^{-1})
h	Planck constant (6.626×10^{-34} J s)
I_b	allotriomorphic ferrite grain boundary nucleation rate per unit area (m^2 s^{-1})
I_b^f, I_b^e, I_b^c	allotriomorphic ferrite nucleation rate per unit area on grain boundary faces, edges and corners (m^2 s^{-1})
$I_{p,b}$	pearlite nucleation rate per unit boundary area (m^2 s^{-1})
I_v	nucleation rate per unit volume (m^3 s^{-1})
I_α	nucleation rate of α phase per unit volume (m^3 s^{-1})
$I_{w,b}$	Widmanstätten ferrite nucleation rate per unit boundary area (m^2 s^{-1})
I_{α_b}	displacive nucleation rate per unit volume (m^3 s^{-1})
k_B	Boltzmann constant (1.380×10^{-23} J K^{-1})
K_1^f, K_1^e, K_1^c	site factors expressing fraction of active nucleation sites on grain boundary faces, edges and corners
K_2^f, K_2^e, K_c^e	shape factors affecting interfacial energy for nucleation on grain faces, edges and corners
L	width of solute diffusion zone ahead of transformation interface (m)
$\overline{L}$	mean lineal intercept austenite grain size (μm)
M_f	martensite finish temperature
M_s	martensite start temperature
n_c	number of critical size nuclei
n_P	number of close-packed planes in stacking fault
n_s^f, n_s^e, n_s^c	number of active nucleation sites per unit area on grain faces, edges and corners (m^{-2})
n_v	number of active nucleation sites per unit volume (m^{-3})
n_v^f, n_v^e, n_v^c	number of active nucleation sites per unit volume on grain faces, edges and corners (m^{-3})
N	total number of atoms in initial phase
N_A	Avogadro's number (6.022×10^{23} J mol^{-1})
N_m	number of martensite plates per unit volume (m^{-3})

N_s	number of ferrite particles per unit grain boundary area (m^{-2})
N_v	number of ferrite particles per unit volume (m^{-3})
N_α	number of particles of a phase α
N_{α_b}	number of bainite sub-units per unit volume (m^{-3})
O_b	total area of a plane parallel to the grain boundary plane (m^2)
O_p^e	extended area of pearlite on a plane (m^2)
O_α	actual area of allotriomorphic ferrite on a plane (m^2)
O_α^e	extended area of allotriomorphic ferrite on a plane (m^2)
$O_{\alpha_w}^e$	extended area of Widmanstätten ferrite on a plane (m^2)
p	Péclet number
p_{AB}	number of $A-B$ interatomic bonds
q	ferrite allotriomorph half-thickness (m)
q_w	height of Widmanstätten ferrite plate above grain boundary (m)
q_α	height of allotriomorphic ferrite particle above grain boundary (m)
Q	activation energy for atoms crossing matrix/nucleus interface (J)
r	radius of new nucleus during nucleation (m)
r^*	critical nucleus radius for stability during nucleation (m)
r_w	Widmanstätten ferrite plate tip radius (m)
r_{w_c}	critical Widmanstätten ferrite plate tip radius at which growth ceases (m)
r_α	radius of a particle of a phase α (m)
R	universal molar gas constant (8.314 J mol^{-1} K^{-1})
S	entropy (J mol^{-1} K^{-1})
S_p	pearlite interlamellar spacing (m)
S_c	critical pearlite interlamellar spacing (m)
S_v	austenite grain surface area per unit volume (m^{-1})
S_v^{db}	austenite grain surface area per unit volume due to deformation bands (m^{-1})
S_v^{eff}	effective austenite grain surface area per unit volume (m^{-1})
S_v^{gb}	austenite grain surface area per unit volume due to grain boundaries only (m^{-1})
S_v^o	original austenite grain surface area per unit volume (m^{-1})
S_α	thickness of ferrite lamella in pearlite (m)
S_θ	thickness of cementite lamella in pearlite (m)
t	time (s)
t_1	incubation period for Widmanstätten ferrite transformation (s)
T	absolute temperature (K)
T_e	eutectoid temperature (K)
T_h	highest temperature at which displacive transformation is possible (K)
T_o	temperature at which austenite and ferrite of the same composition have

	the same free energy (K)
T_o'	T_o temperature but allowing for 400 J mol^{-1} stored energy (K)
T_q	quench temperature (°C)
u	volume of bainite sub-unit (m^3)
u'	temperature-dependent bainite sub-unit volume (m^3)
v^*	activation volume (m^3)
v_i	velocity of transformation interface (m s^{-1})
v_α	volume of allotriomorphic ferrite particle (m^3)
v_τ	volume of a particle nucleated at a time τ (m^3)
V	total volume of the assembly (m^3)
$\overline{V}$	average volume of martensite plate (m^3)
V_L	Widmanstätten ferrite plate lengthening rate (m s^{-1})
V_m	volume fraction of martensite
V_w	volume fraction of Widmanstätten ferrite
V_α	actual volume of allotriomorphic ferrite (m^3)
V_α^e	extended volume of allotriomorphic ferrite (m^3)
V_α^m, V_γ^m	molar volume of ferrite, austenite (m^3)
$V_{\alpha,b}$	total volume of allotriomorphic ferrite originating from one boundary (m^3)
V_{α_b}	actual volume of bainite (m^3)
V_γ	volume fraction of retained austenite
W	stored energy per unit volume of deformed austenite (J m^{-3})
W_s	Widmanstätten ferrite start temperature
x	mole fraction of carbon
x_m	mole fraction of carbon in ferrite nucleus corresponding to maximum free energy change
x_r	mole fraction of carbon in austenite at Widmanstätten ferrite plate tip
$x_{T_o'}$	mole fraction of carbon at T_o' boundary
x_α	mole fraction of carbon in ferrite
x_γ	mole fraction of carbon in austenite
$x^{\alpha\gamma}$	mole fraction of carbon in ferrite in equilibrium with austenite
$x^{\gamma\alpha}$	mole fraction of carbon in austenite in equilibrium with ferrite
$x_C^{\gamma\alpha}$	mole fraction of carbon in austenite in local equilibrium with ferrite
$x_X^{\gamma\alpha}$	mole fraction of substitutional element in austenite in equilibrium with ferrite
$x_C^{\gamma\theta}$	mole fraction of carbon in austenite in local equilibrium with Fe_3C
$x_X^{\gamma\theta}$	mole fraction of substitutional element in austenite in equilibrium with Fe_3C
$\overline{x}$	mole fraction of carbon in bulk austenite
$\overline{x}'$	mole fraction of carbon in enriched bulk austenite

$\overline{x}_X$	average mole fraction of substitutional element in bulk austenite
X_α	volume fraction of ferrite
y	perpendicular height of plane above austenite grain boundary (m)
z	distance moved by γ/α interface (m)
z_c	coordination number for octahedral interstices
Z	Zeldovich non-equilibrium factor for nucleation
α	allotriomorphic ferrite
α_1	one-dimensional parabolic thickening rate constant (m $s^{-\frac{1}{2}}$)
α_w	Widmanstätten ferrite
β	autocatalysis factor for bainite nucleation
γ	austenite
γ_m	activity coefficient affecting carbon diffusivity
Γ	capillarity constant
δ	atomic spacing (m)
Δf^*	Zener ordering term
ΔF	activation free energy for carbon diffusivity (J)
ΔG_{chem}	chemical free energy change between parent and product phases (J mol^{-1})
ΔG_m	maximum driving force for nucleation (J mol^{-1})
ΔG_s	strain energy change per unit volume (J m^{-3})
ΔG_v	free energy change per unit volume for nucleation (J m^{-3})
$\Delta G^{\gamma\rightarrow\alpha}$	free energy change for transformation from austenite to ferrite of the same composition (J mol^{-1})
$\Delta G^{\gamma\rightarrow\alpha'}$	as $\Delta G^{\gamma\rightarrow\alpha}$ but with Zener ordering
$\Delta G^{\gamma\rightarrow\alpha}_{M_s}$	free energy change for transformation from austenite to ferrite of the same composition at the M_s temperature (J mol^{-1})
$\Delta G^{\gamma\rightarrow\gamma'+\alpha}$	free energy change for transformation from austenite to ferrite (J mol^{-1})
$\Delta G^{\gamma\rightarrow\alpha}_{Fe}$	free energy change for austenite to ferrite transformation in pure iron (J mol^{-1})
$\Delta G^{\gamma\rightarrow\alpha}_{mag}$	magnetic component of austenite to ferrite free energy change (J mol^{-1})
$\Delta G^{\gamma\rightarrow\alpha}_{nm}$	non-magnetic component of austenite to ferrite free energy change (J mol^{-1})
ΔG_{mix}	change in free energy of mixing (J mol^{-1})
ΔH	change in enthalpy (J mol^{-1})
ΔH_{mix}	change in enthalpy of mixing (J mol^{-1})
ΔS	change in configurational entropy (J mol^{-1})
ΔS_{mix}	change in configurational entropy of mixing (J mol^{-1})
Δt	time step (s)
ΔT	temperature displacement or undercooling (K)
ε	strain

η_α, η_w	aspect ratio of allotriomorphic ferrite, Widmanstätten ferrite particle
θ	ratio of number of carbon atoms to total number of solvent atoms
θ_{α_b}	maximum volume fraction of bainite
$\theta_{\gamma\alpha}$	dihedral angle at γ/α interface of ferrite nucleus
λ	spacing of {002} austenite planes (m)
λ_1, λ_2	empirical constants affecting bainitic autocatalysis factor
μ	shear modulus
$\mu_C^\alpha\{x\}$	chemical potential of carbon in ferrite evaluated at composition x (J mol^{-1})
$\mu_C^\gamma\{x\}$	chemical potential of carbon in austenite evaluated at composition x (J mol^{-1})
$\mu_{Fe}^\alpha\{x\}$	chemical potential of iron in ferrite evaluated at composition x (J mol^{-1})
$\mu_{Fe}^\gamma\{x\}$	chemical potential of iron in austenite evaluated at composition x (J mol^{-1})
ν	collision frequency of atoms with critical nucleus (s^{-1})
ξ_p	extent of pearlite reaction
ξ_α	extent of allotriomorphic ferrite reaction
ξ_{α_b}	extent of bainite reaction
ξ_{α_w}	extent of Widmanstätten ferrite reaction
ρ	dislocation density (m^{-2})
ρ_A	density of atoms in close-packed planes (mol m^{-2})
ρ_j	density of sites factor for nucleation
σ	interfacial energy per unit area (J m^{-2})
σ_y	yield strength (N m^{-2})
$\sigma_{\alpha\theta}$	ferrite/cementite interfacial energy per unit area (J m^{-2})
$\sigma_{\gamma\alpha}$	austenite matrix/ferrite nucleus interfacial energy per unit area (J m^{-2})
$\sigma_{\gamma\gamma}$	austenite/austenite interfacial energy per unit area (J m^{-2})
τ	incubation period for nucleation (s)
τ_d	energy per unit length of dislocation line (J m^{-1})
τ_o	magnitude of lattice frictional shear stress resisting dislocation motion
τ_μ	athermal resistance to dislocation motion
ω_α	carbon-carbon interaction energy in ferrite (J mol^{-1})
ω_γ	carbon-carbon interaction energy in austenite (J mol^{-1})
$\Omega_\alpha, \Omega_\gamma$	equilibrium ferrite, austenite fraction, from lever rule

Chapter 1

Introduction

Steel is one of the most important materials produced in the world. It is used to manufacture a wide range of goods, from ships and cars, construction beams and piling, to household appliances and drinks cans. There are many complex and interacting metallurgical requirements which must be taken into consideration when processing steel. A small alteration to composition, grain structure or heat treatment can have a significant impact on the final microstructure and properties. Therefore, it is imperative that these effects are fully understood before introducing a new steel grade or process route. However, mill trials to test new or modified steel grades and rolling schedules are expensive and time consuming, costing thousands of pounds and interrupting the normal commercial operations.

There has thus been much research over the past 20 years aimed at the development of mathematical models that will predict the phase transformations that occur during thermomechanical processing. Off-line calculations can then be performed to minimise the number of actual mill trials required. There are many empirical and semi-empirical models to predict microstructures or grain sizes, created by fitting equations to experimental data and these work very successfully [1–6]. However, their applicability is restricted to the range of steel compositions and process routes for which they were designed and calibrated, and they cannot necessarily be extended to the design of new steels. To this end, many researchers have created models based on the fundamental physical and metallurgical principles of phase transformations, utilising thermodynamics and nucleation and growth kinetic theories with the aim of developing a generally applicable model for a wide range of steels. This is precisely the purpose of the present work.

1.1 The Hot Rolling Process

The steel plate, strip and "sections" from which many products are manufactured are produced by the hot-rolling process, Figure 1.1. In this process, a cast steel billet or ingot is re-heated in a furnace to a temperature of around 1100-1250 °C (the exact temperature varies with the steel composition), at which it is fully austenitic. It is then passed through a series of rolling mill stands which reduce the billet to its final shape and cross-section whilst still at high temperature in the austenitic state, and, importantly, refine the microstructure of the austenite. This occurs by a process of deformation, recovery and recrystallisation of the austenite grains (Figure 1.2). The rolling deformation elongates or 'pancakes' the original grains and introduces a high density of dislocations. New grains are nucleated at these high energy defects and grow to replace the deformed structure with a finer one. Repeated deformation and recrystallisation can occur during the rolling schedule and the resultant austenite can be either fully recrystallised, or, if the final rolling passes occur below the recrystallisation stop temperature of the austenite, still deformed [7]. After the steel exits from the finishing stands of the mill it enters the run-out table or cooling banks, where it is sprayed with water jets or air-cooled. Interrupted cooling schedules can be applied, whereby the cooling sprays are withheld in a particular temperature range for a specified time interval before continued processing. It is the austenite microstructure and the cooling schedule which determine the final room temperature microstructure of the steel. This microstructure in turn defines the mechanical properties of the material, such as yield stress, ultimate tensile strength (UTS) and fracture toughness. The combination of microstructure and properties determines the suitability of different steels for different applications. Thus, careful control of the hot-rolling process is essential to ensure the correct combination of austenite deformation and cooling is applied at the appropriate temperatures to achieve the desired final microstructure.

1.2 The Iron-Carbon Phase Diagram

The equilibrium phases present in the steel at each temperature as a function of composition can be represented by the phase diagram for the alloy. Figure 1.3 illustrates the iron-rich section of the binary Fe-C phase diagram. In pure iron, at temperatures between 910 °C and 1390 °C, the iron is fully austenitic. As it is alloyed with increasing amounts of carbon, the austenite is stabilised to lower temperatures, reaching a minimum at the eutectoid composition, 0.78 wt.% carbon. This phase boundary is known as the Ae_3 line. Below the Ae_3 temperature, ferrite (α) starts to form from the austenite (γ), the ferrite fraction increasing as temperature decreases until all the austenite has transformed at the

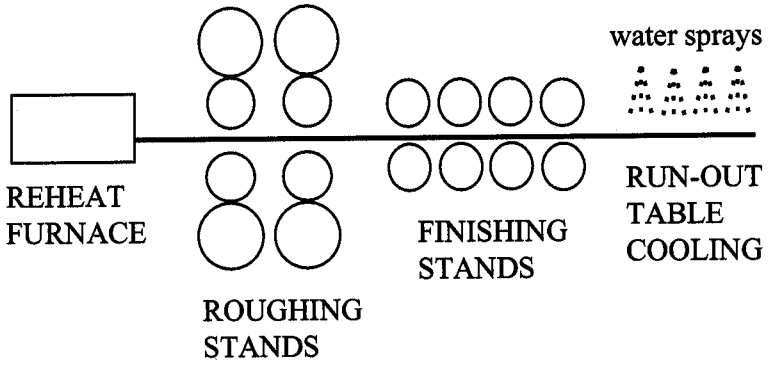

Figure 1.1: Schematic layout of a hot-rolling mill, showing the reheating furnace, rolling stands and run-out table. The roughing stands impart large initial reductions in thickness.

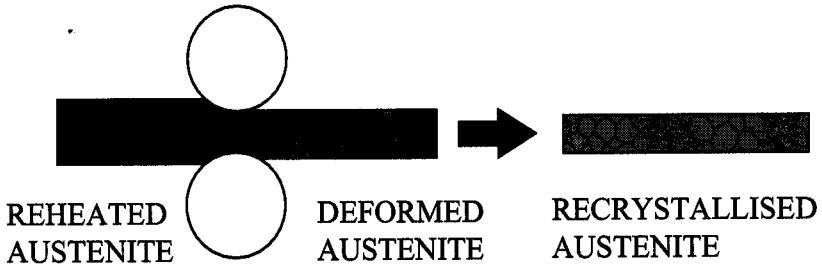

Figure 1.2: Illustration of austenite deformation and recrystallisation during hot-rolling.

Ae_1 temperature (723 °C in the Fe-C system). The solubility of carbon in ferrite is very low, with a maximum of 0.02 wt.% at 723 °C. At higher carbon levels, the excess carbon is rejected from the ferrite into the austenite. Below Ae_1 any remaining austenite transforms to pearlite, a lamellar mixture of ferrite and cementite (Fe_3C). Thus, at room temperature the equilibrium microstructure of a hypo-eutectoid steel (< 0.78 wt.% carbon) consists of a mixture of ferrite and pearlite, the exact proportions dependent upon the carbon content of the steel.

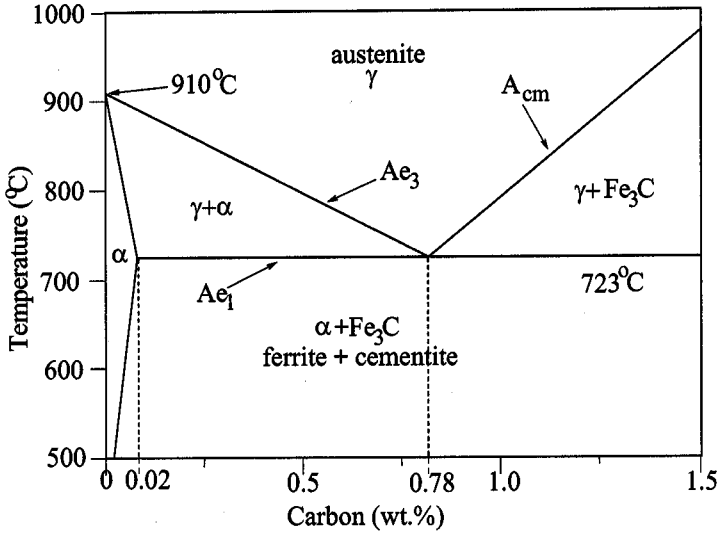

Figure 1.3: Schematic of the iron-rich section of the equilibrium iron-carbon phase diagram (cementite is metastable with respect to graphite).

Steels are alloyed with many elements other than carbon in order to achieve the wide range of properties demanded by different applications. Some examples include the improvement of hardenability by the addition of Mn, Cr and Mo which retard the transformation of austenite and the enhancement of corrosion resistance with Cr, Ni and Cu. Nb and V aid grain refinement and provide precipitation strengthening. All these solutes, like carbon, also affect the free energies of the phases so that the multi-component phase diagram will differ from the basic Fe-C diagram. The relative stabilities of austenite and ferrite are affected and consequently the solutes either accelerate or retard the rate at which austenite decomposes. Those which accelerate transformation (such as Co, Al) are "ferrite stabilisers" whereas those which retard it (such as C, Mn) are "austenite stabilisers".

1.3 Phase Transformations

The phase fields illustrated by the phase diagram are for equilibrium conditions only. The cooling rates encountered during steel processing are usually too fast for true equilibrium to be achieved, and thus several non-equilibrium phases can also form, which are often desirable in certain steels. Two types of phase transformation are possible – reconstructive and displacive. In reconstructive transformations, there is the diffusion of all atoms since the crystal lattice changes by an uncoordinated movement of atoms ('civilian') to form the product structure. Reconstructive transformations occur at temperatures close to the Ae_3, where atomic mobility is sufficiently high for diffusion to occur readily. The diffusion of the solute atoms during the transformation is generally the rate-controlling process. Allotriomorphic ferrite and pearlite both form in this manner.

Displacive transformations involve a coordinated ('military') motion of atoms to generate the product phase crystal structure. They occur at lower temperatures where diffusion is very slow and are favoured during rapid cooling when there is insufficient time for atoms to diffuse. The transformation is actually a deformation, as no atomic bonds are broken, and thus there is a strain energy which must be overcome for growth of the phase to occur. Bainite and martensite form by this mechanism. Widmanstätten ferrite is also considered to form displacively, but carbon diffusion is required for its growth.

These five phases are commonly observed in hot-rolled steels and different combinations of them are preferred for different applications. Pearlite and allotriomorphic ferrite are adequate for many situations, such as structural plates and sections, providing good strength at low cost, whereas the higher strength bainite and martensite phases are required for more demanding applications, such as creep-resistant steels for the power industry. High strength, low alloy (HSLA) or microalloyed steels, used for plate and strip production, comprise predominantly allotriomorphic ferrite which is controlled-rolled, a process which is designed to produce a fine grain size and thus high strength, whilst the low carbon and alloy content improves weldability and ductility.

1.4 Importance of Grain Size

The scale of the microstructure is important with respect to mechanical properties. A fine ferrite grain size produces a higher yield strength, σ_y, according to the Hall-Petch relation [8, 9]:

$$\sigma_y = \sigma_0 + k_y d_\alpha^{-\frac{1}{2}} \tag{1.1}$$

where σ_0 is the friction stress required to move dislocations in the pure crystal lattice, k_y is a constant, and d_α is a measure of the ferrite grain size. The aim of thermomechanical processing is to produce a fine ferrite grain size, *via* austenite grain refinement or fast cooling. Ferrite generally nucleates at the austenite grain boundaries and thus a finer austenite structure produces fine ferrite grains. However, there appears to be a limit as to the smallest recrystallised austenite grain size that can be achieved in commercial practice and thus to the ferrite grain size that can be obtained [10]. Further ferrite refinement can be achieved by transformation from deformed austenite grains. The thickness of the pancaked austenite grains then controls the ferrite grain size, which can be reduced down to 2-3 μm [7]. The residual deformation in the austenite also refines the ferrite structure by increasing the nucleation rate. Faster cooling increases the amount of undercooling below the Ae_3 and hence the driving force for transformation. Thus, a knowledge of the kinetics of the transformation during cooling, coupled with the thermodynamics, is essential for an understanding of the how the hot-rolling process affects the final microstructure of the steel.

1.5 Aim of This Work

In this thesis, a new mathematical transformation model has been developed for the purpose of simulating the phase transformations which occur during cooling of hot-rolled austenite. The model is quite general but was targetted at modern HSLA steel compositions, which typically contain 0.05-0.12 wt.% C, < 0.25 wt.% Si, 1.4-1.7 wt.% Mn, plus other small additions including the microalloying elements Nb, V and Ti [11]. It can also be applied to some more highly alloyed steels. A flowchart of the approach to developing the model is provided in Figure 1.4. The thermodynamic and kinetic metallurgical theory underlying the transformation of austenite to allotriomorphic ferrite, pearlite, Widmanstätten ferrite, bainite and martensite is reviewed and a number of existing transformation models are discussed. The development of the new model is then described, and the individual models for each of the phases are combined using recent theory which enables the simultaneous, competitive formation of the phases to be considered. A series of laboratory experiments to validate the model are described and the results discussed. Then, the thorough validation and application of the model, both of the individual phases and the combined program, is detailed. Comparisons are made with both new and published experimental data. The adaptation of the model to account for the important effects of residual deformation in the austenite after hot-rolling is discussed. Finally, the successful application and the limitations of the model are highlighted and suggestions for expansion and improvement are proposed.

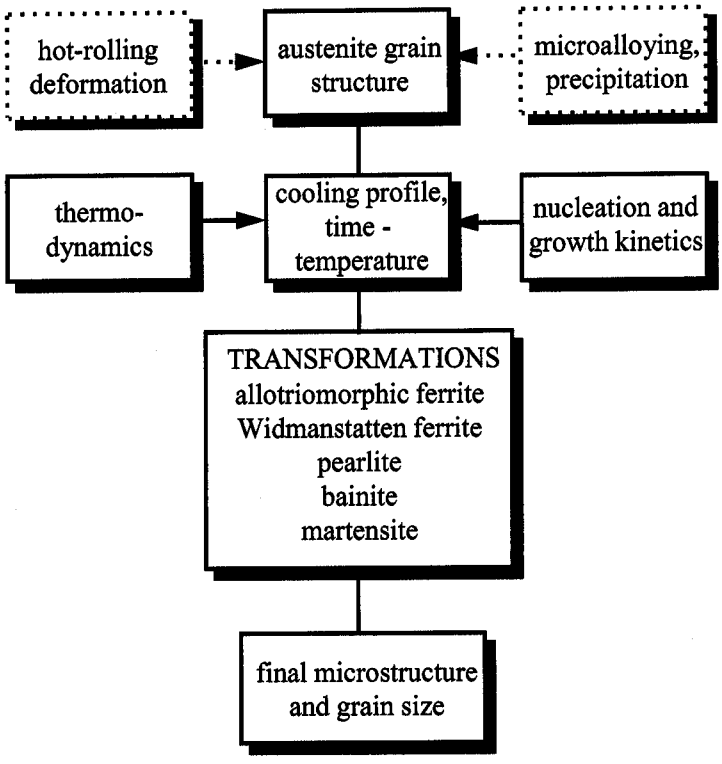

Figure 1.4: Flowchart illustrating the basic layout of the phase transformation model. The dashed boxes refer to areas of research not addressed in the present work, but which could provide input data to a phase transformation model.

Chapter 2

Review of Thermodynamics of Solutions

The basic theory of the thermodynamics of solid solutions is reviewed briefly in this chapter, in order to introduce the concepts of free energy, chemical potential and activity used later in this thesis.

2.1 Free Energy and Solid Solutions

The Gibbs free energy, G, of a system is defined as [12]:

$$G = H - TS \tag{2.1}$$

where H is the enthalpy, T the absolute temperature and S the entropy of the system. During an allotropic transformation, the most stable phase at a particular temperature will be the one with the lowest free energy. The driving force for a transformation from a phase α to another phase β at a temperature T is:

$$\begin{aligned} \Delta G &= G^{\beta} - G^{\alpha} = (H^{\beta} - H^{\alpha}) - T(S^{\beta} - S^{\alpha}) \\ &= \Delta H - T\Delta S \end{aligned} \tag{2.2}$$

In a system containing more than one component, the free energy is also a function of composition as well as variables such as temperature and pressure. Consider a binary solution of A and B atoms, where one mole of homogeneous solid solution is created by mixing x_A moles of A with x_B moles of B, such that $x_A + x_B = 1$. The molar free energy of the system is determined from the energies of the components plus the change in free energy due to mixing of the atoms, ΔG_{mix}:

$$G = x_A G_A + x_B G_B + \Delta G_{mix} \tag{2.3}$$

where G_A and G_B are the molar free energies of pure A and pure B at the same temperature and pressure. From equation 2.2 it follows that:

$$\Delta G_{mix} = \Delta H_{mix} - T\Delta S_{mix} \tag{2.4}$$

ΔH_{mix} is the enthalpy of mixing and represents the difference in internal energy of the system before and after mixing of the components (ignoring any volume changes). ΔS_{mix} is the difference in entropy – the degree of randomness of the atoms in the system – before and after mixing assuming that other contributions to entropy can be neglected. In the simplest case, $\Delta H_{mix} = 0$, and the free energy change on mixing depends only on the entropy of mixing. This is an *ideal solution.* If A and B atoms mix to form a substitutional solid solution where all configurations of A and B are equally probable, then for one mole of solution it can be shown that [12, 13]:

$$\Delta S_{mix} = -R(x_A \ln x_A + x_B \ln x_B) \tag{2.5}$$

where R is the universal gas constant. Therefore, the free energy of mixing becomes:

$$\Delta G_{mix} = RT(x_A \ln x_A + x_B \ln x_B) \tag{2.6}$$

Figure 2.1 illustrates the variation in ΔG_{mix} with composition for an ideal solution. The total free energy of the solution is then:

$$G = x_A G_A + x_B G_B + RT(x_A \ln x_A + x_B \ln x_B) \tag{2.7}$$

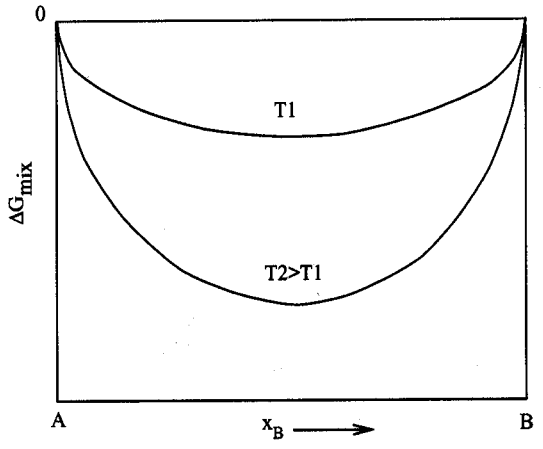

Figure 2.1: Free energy of mixing for an ideal solution.

In reality, ΔH_{mix} is not zero as heat is often evolved or absorbed during mixing. The zeroth approximation of the *quasichemical model*, (often known as the regular solution model), takes ΔH_{mix} to be non-zero and due only to the bond energies between nearest neighbour atoms. The three possible types of interatomic bonds in binary solutions are $A-A$, $B-B$ and $A-B$, having energies E_{AA}, E_{BB} and E_{AB}, respectively. The change in enthalpy of mixing is given by:

$$\Delta H_{mix} = p_{AB}E \tag{2.8}$$

where p_{AB} is the number of $A-B$ bonds and

$$E = E_{AB} - \frac{1}{2}(E_{AA} + E_{BB}) \tag{2.9}$$

If $E = 0$ then we have an ideal solution where the atomic arrangement is completely random. In such a solution it can be shown that,

$$p_{AB} = N_A z x_A x_B \tag{2.10}$$

where N_A is Avogadro's number and z is the number of bonds per atom. The enthalpy of mixing is then:

$$\Delta H_{mix} = N_A z E x_A x_B = \Omega x_A x_B \tag{2.11}$$

The free energy change on mixing for a regular solution is obtained by assuming that the entropy of mixing is ideal:

$$\Delta G_{mix} = \Omega x_A x_B + RT(x_A \ln x_A + x_B \ln x_B) \tag{2.12}$$

Figure 2.2 illustrates the variation of ΔG_{mix} with different compositions, values of Ω and temperature. When $\Omega < 0$, $A-B$ bonds and ordering are favoured, whereas $\Omega > 0$ is due to more $A-A$ and $B-B$ bonds and clustering. The total free energy of the regular solution is given by:

$$G = x_A G_A + x_B G_B + \Omega x_A x_B + RT(x_A \ln x_A + x_B \ln x_B) \tag{2.13}$$

The austenite (Fe-C) solid solution shows large deviations from an ideal configurational entropy and thus the above equation is inappropriate. Instead, the first order approximation of the quasichemical theory can be used in which a random distribution of atoms is no longer assumed. The free energy of the solution is determined from the pairwise interaction energies between nearest neighbour atoms, as before. However, the probability of occupation of a proportion of nearest neighbour interstitial sites is reduced due to a finite repulsive interaction between the carbon atoms. Certain atomic sites are more likely to be occupied whilst others are excluded. McLellan and Dunn [14], in particular, have applied this quasichemical model to carbon in austenite and successfully modelled the activity of carbon in austenite as a function of carbon concentration.

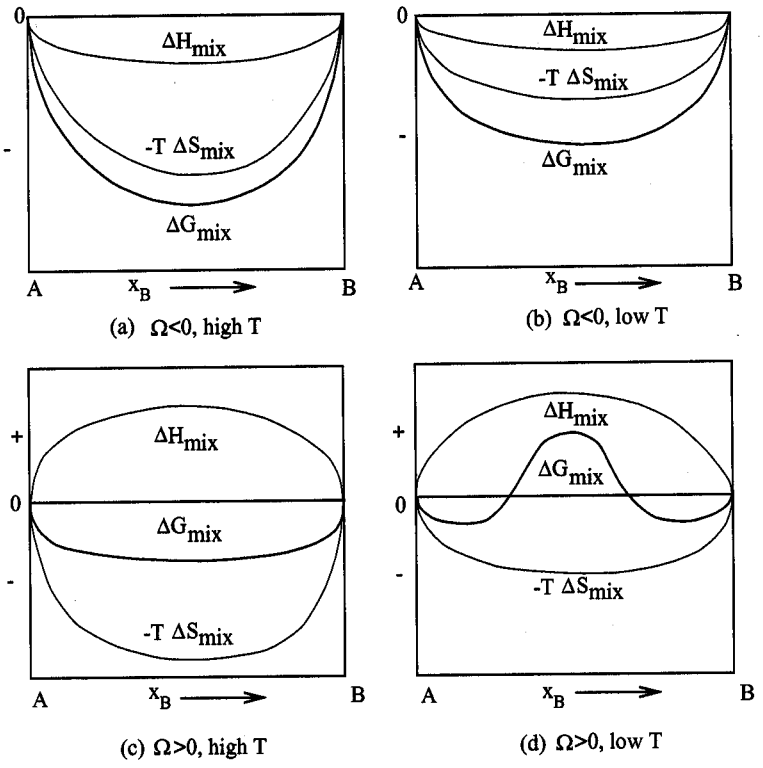

Figure 2.2: Free energy of mixing for a regular solution, showing the effect of different values of ΔH_{mix} (after [12]).

2.2 Chemical Potential and Activity

The chemical potential, μ_A, of a component A in a phase is defined as [12]:

$$\mu_A = \left(\frac{\partial G'}{\partial n_A}\right)_{T,P} \tag{2.14}$$

where G' is the free energy of the whole system. μ_A is the proportionality constant relating a small quantity of A, dn_A moles, added to a large amount of a phase at constant temperature and pressure, to the small increase in the total free energy of the system, dG', it generates. dn_a must be sufficiently small that the composition of the phase is not significantly altered, because μ_A is composition dependent. In a binary solution, the separate additions of small amounts of A and B can be summed to give:

$$dG' = \mu_A dn_A + \mu_B dn_B \tag{2.15}$$

The size of the system can be increased without altering its overall composition if A and B atoms are added in proportions according to $x_A + x_B = 1$, *i.e* such that $dn_A : dn_B = x_A : x_B$. If the size of the system is increased by exactly one mole then the free energy

change will be the molar free energy, G. Therefore,

$$G = \mu_A x_A + \mu_B x_B \quad \text{J mol}^{-1} \tag{2.16}$$

Comparing equation 2.16 with the expression for the free energy of an ideal solution (equation 2.7) produces the following equations for the chemical potentials in an ideal solution, illustrated on the free energy–composition diagram in Figure 2.3:

$$\begin{aligned} \mu_A &= G_A + RT \ln x_A \\ \mu_B &= G_B + RT \ln x_B \end{aligned} \tag{2.17}$$

The chemical potential of each component at a particular composition can be obtained from the free energy diagram by drawing a tangent to the free energy curve and determining its intersection with the component axes. Points e and f in Figure 2.3 correspond to μ_A and μ_B, respectively.

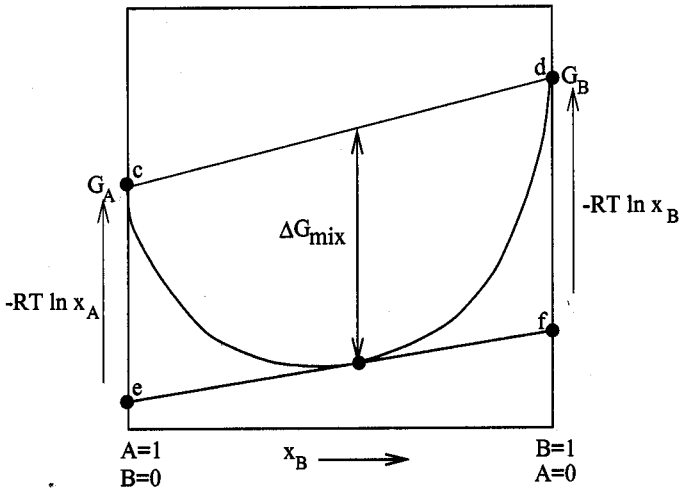

Figure 2.3: Chemical potentials and free energy curve for a binary ideal solution.

It is necessary to use the *activity* of a component for non-ideal solutions. The activity is defined such that the distances ce and df in Figure 2.3 are $-RT \ln a_A$ and $-RT \ln a_B$, respectively, where a_A and a_B are the activities of A and B atoms, and points c and d correspond to the free energies of pure A, G_A, and pure B, G_B, respectively. Therefore,

$$\begin{aligned} \mu_A &= G_A + RT \ln a_A \\ \mu_B &= G_B + RT \ln a_B \end{aligned} \tag{2.18}$$

The relationship between activity and mole fraction will vary with the composition of the solution. For a regular solution it is given by [12]:

$$\ln\left(\frac{a_A}{x_A}\right) = \frac{\Omega}{RT}(1 - x_A)^2 \tag{2.19}$$

and

$$\ln\left(\frac{a_B}{x_B}\right) = \frac{\Omega}{RT}(1 - x_B)^2 \tag{2.20}$$

In an ideal solution, $\Omega = 0$, so $a_A = x_A$ and $a_B = x_B$.

2.3 Summary

The concepts of the free energy of a solid solution and the chemical potential and activity of a component in that solution have been introduced. The free energy contains contributions from the enthalpy and entropy of mixing of the solution which depend upon the atomic configuration. Three solution models have been considered: ideal, where $\Delta H_{mix} = 0$ and a completely random atomic arrangement is assumed; regular, where $\Delta H_{mix} \neq 0$ but the atoms are still considered to be randomly arranged; and finally the first order quasichemical model, where $\Delta H_{mix} \neq 0$ and a non-random configuration is accommodated. The latter model can be applied to the solution of carbon in austenite.

Chapter 3

Reconstructive Transformations

3.1 The Allotriomorphic Ferrite Transformation

Allotriomorphic ferrite is an important phase in low alloy steels. It is the first phase to form from austenite at temperatures below the Ae_3 and thus it determines the amount and composition of austenite remaining for subsequent transformation to other phases. Ferrite allotriomorphs usually nucleate at the prior austenite grain boundaries [15], as these are higher energy sites than the interiors of the grains. The allotriomorphs both lengthen along the boundaries and thicken into the grain interiors to form equiaxed ferrite grains. Both the thermodynamics and kinetics of the ferrite transformation must be considered.

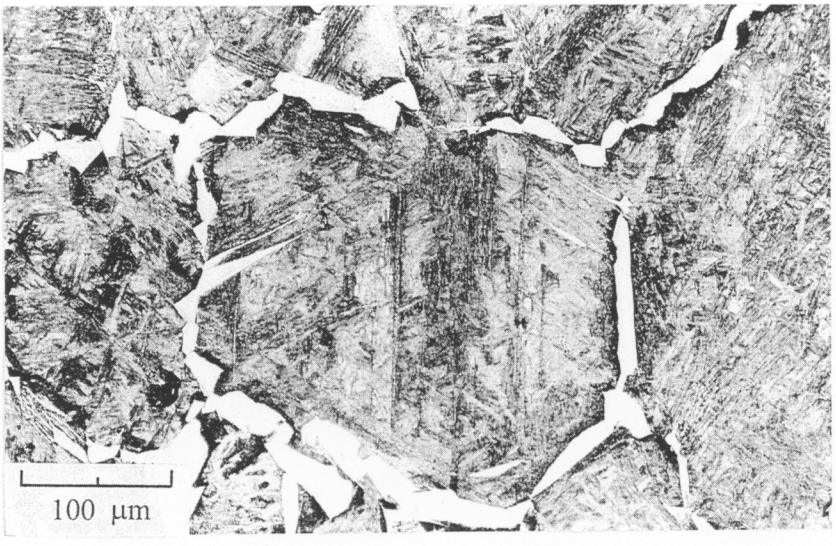

Figure 3.1: Micrograph of a low alloy steel, showing allotriomorphic ferrite (white phase) decorating the prior austenite grain boundaries.

3.1.1 Thermodynamics

The driving force for the transformation from austenite to ferrite is the reduction in the free energy of the system obtained when the face-centred cubic (fcc) austenite lattice transforms to the more stable body-centred cubic (bcc) ferrite structure. The free energy diagram in Figure 3.2 shows that at a particular temperature, T_1, austenite of bulk composition $\overline{x}$ can lower its overall free energy by forming ferrite of composition $x^{\alpha\gamma}$ leaving the austenite with composition $x^{\gamma\alpha}$. The austenite is enriched by the carbon partitioned as the ferrite grows. As the temperature continues to decrease, under equilibrium conditions the austenite composition will follow the Ae_3 line until the eutectoid temperature is reached, when all the remaining austenite transforms to pearlite. $x^{\alpha\gamma}$ is the mole fraction of carbon in ferrite which is in equilibrium with austenite of composition $x^{\gamma\alpha}$.

The equilibrium mole fractions of ferrite and austenite present at each temperature between Ae_3 and Ae_1 can be determined from the phase diagram by the lever rule. The mole fraction of ferrite is:

$$\Omega_\alpha = \frac{x^{\gamma\alpha} - \overline{x}}{x^{\gamma\alpha} - x^{\alpha\gamma}} \tag{3.1}$$

and the mole fraction of austenite is:

$$\Omega_\gamma = \frac{\overline{x} - x^{\alpha\gamma}}{x^{\gamma\alpha} - x^{\alpha\gamma}} \tag{3.2}$$

The equilibrium between the two phases means that the tangent determining the chemical potential of the components in each phase is common to both free energy curves. Therefore, the chemical potentials of iron and carbon are the same in both phases:

$$\begin{aligned} \mu^\alpha_{Fe} &= \mu^\gamma_{Fe} \\ \mu^\alpha_C &= \mu^\gamma_C \end{aligned} \tag{3.3}$$

The driving force; $\Delta G^{\gamma\rightarrow\gamma'+\alpha}$, can be determined by subtracting the free energy of the original austenite phase, G^γ, from that of the product phases, ferrite, G^α, and enriched austenite, $G^{\gamma'}$, weighted by the mole fractions of each phase present:

$$\Delta G^{\gamma\rightarrow\gamma'+\alpha} = G^{\gamma'}\Omega_\gamma + G^\alpha\Omega_\alpha - G^\gamma \tag{3.4}$$

From equation 2.16, we can write:

$$\begin{aligned} G^\gamma &= \overline{x}\mu^\gamma_C\{\overline{x}\} + (1-\overline{x})\mu^\gamma_{Fe}\{\overline{x}\} \\ G^{\gamma'} &= x^{\gamma\alpha}\mu^\gamma_C\{x^{\gamma\alpha}\} + (1-x^{\gamma\alpha})\mu^\gamma_{Fe}\{x^{\gamma\alpha}\} \\ G^\alpha &= x^{\alpha\gamma}\mu^\alpha_C\{x^{\alpha\gamma}\} + (1-x^{\alpha\gamma})\mu^\alpha_{Fe}\{x^{\alpha\gamma}\} \end{aligned} \tag{3.5}$$

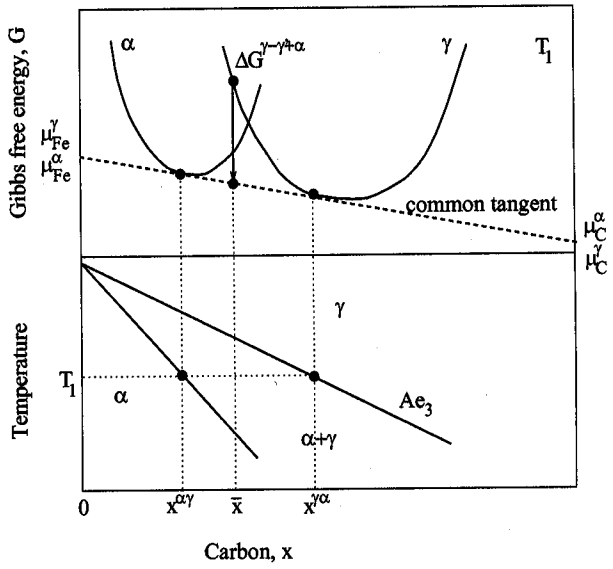

Figure 3.2: Free energy *versus* composition diagram at temperature T_1 and the corresponding section of the Fe-C phase diagram.

where $\mu_C^\gamma\{\overline{x}\}$ represents the chemical potential of carbon in austenite evaluated at the carbon concentration $\overline{x}$, and similarly for the other chemical potentials. Substituting into equation 3.4 and noting the equality of the chemical potentials for ferrite in equilibrium with austenite (from the common tangent construction), it can be shown that [20]:

$$\Delta G^{\gamma\rightarrow\gamma'+\alpha} = \overline{x}(\mu_C^\gamma\{x^{\gamma\alpha}\} - \mu_C^\gamma\{\overline{x}\}) + (1-\overline{x})(\mu_{Fe}^\gamma\{x^{\gamma\alpha}\} - \mu_{Fe}^\gamma\{\overline{x}\}) \tag{3.6}$$

Expanding $\mu = G + RT\ln a$ as in equation 2.18 produces the result:

$$\Delta G^{\gamma\rightarrow\gamma'+\alpha} = \overline{x}RT\ln\frac{a_C^\gamma\{x^{\gamma\alpha}\}}{a_C^\gamma\{\overline{x}\}} + (1-\overline{x})RT\ln\frac{a_{Fe}^\gamma\{x^{\gamma\alpha}\}}{a_{Fe}^\gamma\{\overline{x}\}} \tag{3.7}$$

where $a_C^\gamma\{x^{\gamma\alpha}\}$ is the activity of carbon in austenite evaluated at the concentration $x^{\gamma\alpha}$, and likewise for the other activity terms. Values for the equilibrium phase boundary compositions and activites therefore must be determined to enable calculation of the free energy change for the $\gamma \rightarrow \alpha$ transformation. The $\gamma/\gamma+\alpha$ and $\alpha/\alpha+\gamma$ phase boundaries need to be evaluated both at equilibrium in their normal temperature regimes and extrapolated below the eutectoid temperature into regions where the phases are in metastable equilibrium. The latter enables continued modelling of the phases as temperature decreases, into the displacive transformation regime. Experimental data are available for the equilibrium boundary compositions in Fe-C alloys, but appear to be inaccessible below the eutectoid, so accurate extrapolation is essential. Many models represent the thermodynamic

functions with empirical equations, but these cannot be extrapolated into the lower temperature regime with much confidence. Commercial packages, such as MTDATA [16] and Thermocalc [17], contain large, rigorously evaluated databases from which the equilibrium thermodynamic values can be extracted. These can be coupled with phase transformation models, as is the case with the DICTRA package [18]. An alternative approach is to calculate the necessary thermodynamic parameters within the phase transformation model, using published theory. Models for the thermodynamic behaviour of interstitial solid solutions (such as Fe-C) include the regular solution model and the quasichemical model, as introduced in the previous chapter. The latter attempts to model deviations from an ideal entropy of mixing (non-random atomic arrangement), unlike regular solution models, and can be applied to interstitial solutions with more confidence [19].

Aaronson, Domian and Pound applied three solid solution models to the $\gamma \rightarrow \alpha$ transformation for Fe-C solutions [20]. They found that the first-order quasichemical model of Lacher, Fowler and Guggenheim [21, 22] produced usable equations with which to calculate the activities of carbon and iron in both ferrite and austenite, and thus the free energy change for the transformation. Such a model must be extended to at least ternary systems including a substitutional element, X, to be of practical value for real steels. An approach due to Zener [23] was combined with the Fe-C model to allow for Fe-C-X alloys [24]. Zener proposed that the free energy change for the $\gamma \rightarrow \alpha$ transformation in pure iron could be divided into a magnetic and non-magnetic component, $\Delta G_{nm}^{\gamma \rightarrow \alpha}$ and $\Delta G_{mag}^{\gamma \rightarrow \alpha}$ respectively. Thus,

$$\Delta G_{Fe}^{\gamma \rightarrow \alpha} = \Delta G_{nm}^{\gamma \rightarrow \alpha} + \Delta G_{mag}^{\gamma \rightarrow \alpha} \tag{3.8}$$

He considered that an alloying element would affect these two components separately and assumed that the free energy *versus* temperature curves for pure iron and Fe-X alloys differed only by a displacement of the curves parallel to the temperature axis. The magnitude and direction of this displacement for many common alloying elements was determined [23, 24] and thus the effect of substitutional elements on the free energy change could be incorporated.

3.1.1.1 Driving Force for Ferrite Nucleation

Once the free energy change for the overall austenite to ferrite transformation has been determined, the driving force specifically for nucleation must be considered. In a binary solution, it can be obtained from the free energy–composition diagram using the double tangent construction due to Hillert as illustrated in Figure 3.3. It is assumed that the formation of the ferrite nucleus produces an infinitessimally small change in the bulk austenite composition, as the nucleus volume is very small. In the limit, as this small

change tends to zero, the austenite composition tends toward the bulk composition, $\overline{x}$. A tangent is drawn to the austenite curve at $\overline{x}$ and a second tangent is then constructed to the ferrite curve to determine the driving force for nucleation, ΔG_m, at the nucleus composition x_m. The most likely nucleus composition will be that which maximises the free energy change, and this can be shown to occur when the two tangents are parallel [25]. The differences in the chemical potentials of iron in ferrite at the nucleus composition and in austenite at the bulk composition, $\mu^{\alpha}_{Fe}\{x_m\} - \mu^{\gamma}_{Fe}\{\overline{x}\}$, and of carbon in ferrite at the nucleus composition and in austenite at the bulk composition, $\mu^{\alpha}_{C}\{x_m\} - \mu^{\gamma}_{C}\{\overline{x}\}$, can be seen from the diagram to be equal.

The nucleus composition and the driving force can be obtained by simultaneous, numerical solution of the following two equations [25]:

$$\Delta G^{\gamma\rightarrow\alpha}_{Fe} + RT \ln \frac{a^{\alpha}_{Fe}\{1-x\}}{a^{\gamma}_{Fe}\{1-\overline{x}\}} - RT \ln \frac{a^{\alpha}_{C}\{x\}}{a^{\gamma}_{C}\{\overline{x}\}} = 0 \tag{3.9}$$

$$\Delta G_m = RT \ln \frac{a^{\alpha}_{C}\{x_m\}}{a^{\gamma}_{C}\{\overline{x}\}} \tag{3.10}$$

where $\Delta G^{\gamma\rightarrow\alpha}_{Fe}$ is the free energy change accompanying the $\gamma \rightarrow \alpha$ transformation in pure iron, and $a^{\alpha}_{Fe}\{1-x\}$ refers to the activity of iron in ferrite evaluated at the concentration $(1-x)$, and likewise for the other activity terms.

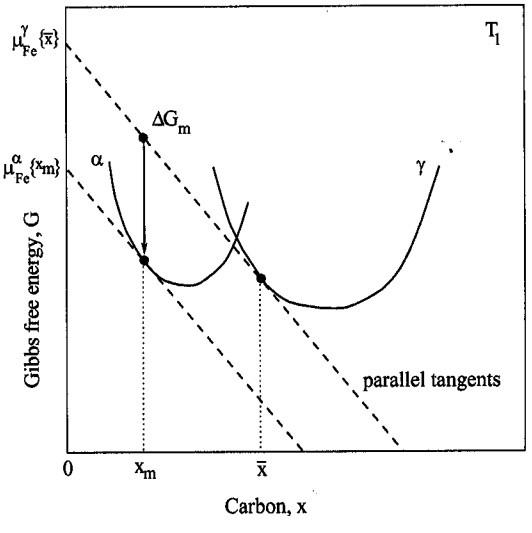

Figure 3.3: Free energy *versus* composition diagram illustrating the use of the parallel tangent construction to determine the driving force for nucleation, ΔG_m.

3.1.2 Modes of Equilibrium

In homogeneous phases, equilibrium exists when the chemical potential of each component is the same in all phases [12]. During diffusional transformations, however, complete homogeneity throughout an entire phase is unlikely, so equilibrium may then occur locally at the interface between two phases. The compositions of the phases at the interface are such as to enable equality of the chemical potentials to be achieved if the transformation is diffusion-controlled. Several modes of local equilibrium have been identified, according to the degree of supersaturation of the parent phase with solute. *Partitioning local equilibrium*, or PLE [26, 27], occurs at small supersaturations, when the bulk austenite composition is close to the $\gamma/\gamma+\alpha$ phase boundary. The activity of the carbon is almost constant in the austenite and thus the driving force for carbon diffusion is close to zero. There is long-range diffusion of the substitutional solute ahead of the interface (Figure 3.4). At large supersaturations, *negligible partitioning local equilibrium* (NPLE), occurs [28]. The iron plus substitutional solute composition of the ferrite is practically equal to that of the bulk austenite, so little partitioning of substitutional solute can occur. A 'spike' of substitutional solute concentration occurs at the interface.

Finally, *paraequilibrium*, a term first used by Hultgren [29], describes a constrained mode of equilibrium where the slower-diffusing substitutional elements are completely unable to partition between the phases but the interstitial carbon partitions to an extent which allows its chemical potential to become identical in both phases. It is a metastable mode of transformation, in which ferrite growth is carbon-diffusion controlled. The ratio of Fe to X atoms remains constant across the interface. A paraequilibrium $\gamma/\gamma+\alpha$ phase boundary, Ae_3', can be defined, below which growth without substitutional solute partitioning may occur. Between the Ae_3 and Ae_3' curves, however, it is a thermodynamic necessity that growth occurs with partitioning [24]. The compositions $x_p^{\gamma\alpha}$ and $x_p^{\alpha\gamma}$ in Figure 3.4 represent the carbon concentrations of the austenite and ferrite respectively, during paraequilibrium transformation.

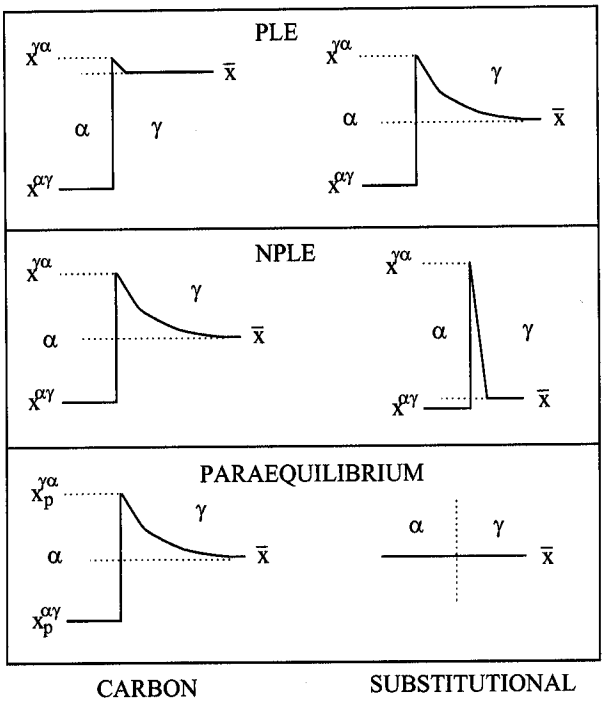

Figure 3.4: Schematic illustration of the variation in carbon and substitutional solute composition across the transformation interface for different modes of equilibrium (after Bhadeshia [30]).

3.1.3 Growth Kinetics

3.1.3.1 Diffusivity of Carbon in Austenite

The growth of ferrite in dilute steels is considered generally to be controlled by the diffusion of carbon, as it is partitioned ahead of the moving transformation interface into the untransformed austenite. An expression describing the rate at which carbon diffuses in austenite is thus required. Carbon diffusivity is known to be strongly concentration dependent, and Kaufman, Radcliffe and Cohen [31] developed the following equation:

$$D_C = \frac{1}{2}\exp\{-30x_\gamma\}\exp\left\{-\frac{Q_D}{RT}\right\} \tag{3.11}$$

where Q_D is a function of x_γ, the mole fraction of carbon in austenite. However, this equation is based on an empirical representation of diffusivity as a function of mole fraction and temperature, and as such is not really suitable for extension to lower temperatures or higher carbon contents than intended.

The theoretical approach of Siller and McLellan [32] considered both the kinetic and thermodynamic behaviour of carbon in austenite in Fe-C alloys. It accounts for the concentration dependence of the activity of carbon in austenite and the existence of a finite repulsive interaction between nearest neighbour carbon atoms in octahedral sites, which reduces the probability of occupation for adjoining sites. The diffusivity is divided into concentration dependent and independent terms and is written as:

$$D\{x,T\} = D'\xi(\theta) \tag{3.12}$$

where

$$D' = \frac{k_B T}{h}\left(\frac{\lambda^2}{3\gamma_m}\right)\exp\left\{-\frac{\Delta F}{k_B T}\right\} \tag{3.13}$$

and

$$\xi(\theta) = a_C^\gamma\left[1 + \frac{z_c(1+\theta)}{1-(1+\frac{\theta}{2})\theta + \frac{z_c}{2}(1+\frac{z_c}{2})(1-\exp\left\{-\frac{\omega_\gamma}{k_B T}\right\})\theta^2}\right] + (1+\theta)\frac{da_C^\gamma}{d\theta} \tag{3.14}$$

where k_B and h are the Boltzmann and Planck constant, respectively, λ is the spacing of the $\{002\}$ austenite planes, γ_m is an activity coefficient, ΔF is an activation free energy, z_c is the coordination number for octahedral interstices (12) and θ is the ratio of the number of carbon atoms to the total number of solvent atoms. Bhadeshia [33] subsequently extended this approach, accounting for the influence of substitutional elements via the carbon-carbon interaction energy in austenite, ω_γ, and the activity and determined values of $\Delta F/k_B = 21230$ K and $\ln(\gamma_m/\lambda^2) = 31.84$, respectively. A recent investigation [34] applied this theory to ternary Fe-C-X alloys, where the substitutional solute X has been

shown to have a significant effect on carbon diffusivity. It was concluded that the diffusivity was well predicted by the theory, the only discrepancy occurring for Fe-C-Cr alloys.

3.1.3.2 Ferrite Growth Rate Constant

Ferrite has been found to grow at a parabolic rate, its growth slowing down with increasing time as the carbon rejected ahead of the interface has further to diffuse. It often forms allotriomorphs growing with an aspect ratio for lengthening to thickening of 3:1 [35, 36].

The growth velocity can be evaluated by consideration of the carbon diffusion profile at the transformation interface, Figure 3.5. In a binary Fe-C alloy, the interface compositions at a particular temperature (of carbon in austenite, $x^{\gamma\alpha}$, and in ferrite, $x^{\alpha\gamma}$, in equilibrium) are fixed by the tie-line on the phase diagram. Carbon partitioned from the ferrite diffuses down the concentration gradient built up ahead of the interface until the bulk alloy composition, $\overline{x}$, is achieved in the austenite away from the interface. The diffusion flux of carbon atoms across a unit area of the interface in unit time can be obtained from Fick's first law as:

$$J_C = -D_C \frac{dx}{dz} \tag{3.15}$$

At the same time, the quantity of carbon partitioned per unit time is given by $(x^{\gamma\alpha} - x^{\alpha\gamma})v_i$, where $v_i = \frac{dz}{dt}$, the velocity of the interface. This is equal to the flux, and thus the interface velocity is [37]:

$$\frac{dz}{dt} = \frac{D_C}{(x^{\gamma\alpha} - x^{\alpha\gamma})} \left.\frac{dx_\gamma}{dz}\right|_{z=z*} \tag{3.16}$$

A simple treatment is to approximate the distribution of carbon as a straight line, such that:

$$\frac{dx_\gamma}{dz} = \frac{x^{\gamma\alpha} - \overline{x}}{L} \tag{3.17}$$

The shaded areas 'A' and 'B' in the diagram are equal, due to conservation of solute, and thus it can be shown that:

$$\frac{dz}{dt} = \frac{D_C}{(x^{\gamma\alpha} - x^{\alpha\gamma})} \frac{(x^{\gamma\alpha} - \overline{x})^2}{2z(\overline{x} - x^{\alpha\gamma})} \tag{3.18}$$

Integrating with respect to time and substituting $z = \alpha_1 t^{\frac{1}{2}}$, the one-dimensional parabolic rate constant, α_1, can be obtained as [38]:

$$\alpha_1 = \frac{D_C^{\frac{1}{2}}(x^{\gamma\alpha} - \overline{x})}{[2(x^{\gamma\alpha} - x^{\alpha\gamma})(\overline{x} - x^{\alpha\gamma})]^{\frac{1}{2}}} \tag{3.19}$$

In reality, the concentration gradient of carbon away from the interface is not constant. It is better represented rigorously by an error function solution to the diffusion equation:

$$x_\gamma = \overline{x} + (x^{\gamma\alpha} - \overline{x})\mathrm{erf}\left\{\frac{z}{2(D_C t)^{\frac{1}{2}}}\right\} \tag{3.20}$$

Differentiating this equation provides $\frac{dx_\gamma}{dz}$ for substitution into equation 3.16, from which the following expression for the one-dimensional parabolic rate constant can be derived [37, 39]:

$$\Omega_\alpha = \sqrt{\pi}\left(\frac{\alpha_1}{2D_C^{\frac{1}{2}}}\right) \text{erfc}\left\{\frac{z}{2(D_C t)^{\frac{1}{2}}}\right\} \exp\left\{\frac{\alpha_1^2}{4D_C}\right\} \tag{3.21}$$

where the supersaturation $\Omega_\alpha = \frac{x^{\gamma\alpha}-\overline{x}}{x^{\gamma\alpha}-x^{\alpha\gamma}}$ and erfc is the error function complement. Values of α_1 can be found by iterative solution of this equation.

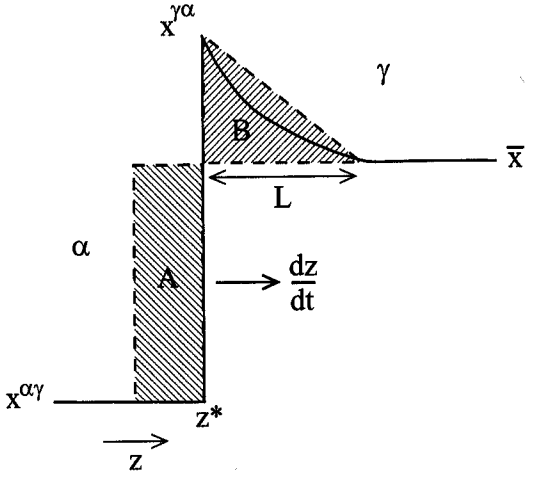

Figure 3.5: Schematic diagram of the carbon diffusion profile at the γ/α interface, which is moving at a rate $\frac{dz}{dt}$ in the direction indicated. The shaded areas show the solute partitioned from the ferrite into the austenite.

For multicomponent steels, the calculation of the growth rate is complicated by the diffusion of both interstitial and substitutional elements. The diffusivity of the interstitial carbon is typically many orders of magnitude greater than that of the substitutional elements, so to choose a suitable tie-line at the interface either the concentration gradient of the carbon must be reduced, or that of the substitutional element must be increased [39]. This corresponds to the PLE and NPLE modes of growth, respectively (Figure 3.4). Alternatively, paraequilibrium can be assumed, whereby the substitutional elements do not partition and are hypothetically combined with the Fe atoms into a "super-element". The growth can then be treated as for the binary Fe-C, but the interface compositions differ from the Fe-C equilibrium due to the effect of the substitutionals on the γ/α transformation thermodynamics.

The operational equilibrium mode during ferrite growth will depend on the steel composition and temperature. Reynolds and co-workers [40] found that the early stages of

growth of ferrite allotriomorphs in Fe-C-X alloys appeared to take place under paraequilibrium conditions. Aaronson *et al.* [41] compared experimental allotriomorph thickening kinetics with local equilibrium and paraequilibrium models. They found that paraequilibrium better accounted for the kinetics, but could still not accurately reproduce the experimental data. ADP [24] investigated the effect of different alloying elements on the position of the $\gamma/\gamma+\alpha$ curve under NPLE. They found that the width of the region where partitioning does occur between the partition and no-partition curves varied with alloying element, with manganese and nickel producing the widest band. This was consistent with their experiments on Fe-C-X alloys, where only Mn and Ni were observed to partition close to the Ae_3 temperature during the early stages of transformation. The same conclusions were reached by Enomoto in a more recent review of literature data on alloy element partitioning in nine Fe-C-X systems [42].

3.1.4 Nucleation Kinetics

3.1.4.1 Classical Nucleation Theory

The classical theory of nucleation was first formulated by Volmer and Weber in 1926, and was subsequently extended by many researchers, but primarily Becker and Döring in 1935. The theory considers random fluctuations in a metastable assembly of atoms and was initially formulated for the condensation of a pure vapour into a liquid. Fluctuations in density and concentration lead to small volumes of the initial phase acquiring new atomic arrangements, thus a local phase transformation has occurred. These are termed *heterophase fluctuations.* A very thorough review of this work is provided by Christian [43].

For a pure system, the overall driving force for the nucleation to occur is provided by the difference in the free energies of the initial and final states of the assembly, but intermediate metastable states may occur. The volume free energy of the nucleus and that of the initial phase it is replacing must be considered, along with the energies of the new surfaces created between the two phases. If the nucleus is constrained by the phase in which it nucleates then there will be an additional strain energy component to the overall free energy. In homogeneous nucleation of a new phase α in a solid matrix γ, assuming a spherical nucleus of radius r, the net free energy change is:

$$\Delta G = -\frac{4\pi}{3}r^3\Delta G_v + \frac{4\pi}{3}r^3\Delta G_s + 4\pi r^2\sigma_{\gamma\alpha} \tag{3.22}$$

where $\sigma_{\gamma\alpha}$ is the interfacial energy per unit area between the two phases, ΔG_v is the magnitude of the chemical driving force per unit volume for formation of α from γ and

ΔG_s is the strain energy per unit volume. The critical free energy barrier to nucleation that must be supplied by thermal fluctuations, G^*, occurs at a critical radius r^* when the free energy change ΔG is a maximum. Thus:

$$\frac{d(\Delta G)}{dr} = -4\pi r^2(\Delta G_v - \Delta G_s) + 8\pi r\sigma_{\gamma\alpha} = 0 \tag{3.23}$$

Therefore,

$$r^* = \frac{2\sigma_{\gamma\alpha}}{(\Delta G_v - \Delta G_s)} \tag{3.24}$$

and the critical free energy barrier is:

$$G^* = \frac{16\pi\sigma_{\gamma\alpha}^3}{3(\Delta G_v - \Delta G_s)^2} \tag{3.25}$$

Figure 3.6 illustrates the competing energy terms as a function of nucleus radius.

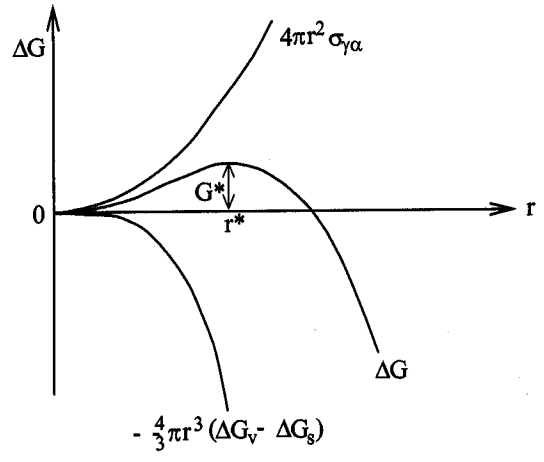

Figure 3.6: The free energy change associated with the homogeneous nucleation of a spherical nucleus of radius r. The critical radius and free energy barrier for nucleation are r^* and G^*, respectively.

Below the critical radius, the free energy can be reduced by dissolution of the nucleus, whilst nuclei larger than r^* can reduce their free energy by growth, the volume free energy change more than compensating for the increased surface energy. Volmer and Weber made the assumption that a stationary distribution of nuclei exists of size $r < r^*$. The number of critical size nuclei present, n_c, is the probability of such a nucleus being formed multiplied by the total number of atoms in the initial (vapour) phase, N:

$$n_c = N \exp\left\{-\frac{G^*}{k_B T}\right\} \tag{3.26}$$

n_c is a statistical distribution function for nuclei of critical size. The rate of nucleation is then n_c multiplied by the probability of a vapour atom condensing onto a critical nucleus in unit time (a collision frequency). The nucleation rate per unit volume, I_v, is thus:

$$I_v = \nu n_v \exp\left\{-\frac{G^*}{k_B T}\right\} \tag{3.27}$$

where ν is the collision frequency and n_v is the number of atoms per unit volume.

There is a problem with Volmer and Weber's steady state distribution in that they assumed that once a nucleus exceeded r^* in size it would grow rapidly and could be removed from the assembly. The number of critical nuclei would then drop abruptly to zero once $r > r^*$. This scenario is unrealistic, as critical nuclei can grow or shrink with equal probability, so Becker and Döring suggested that the distribution function should decrease gradually to zero once $r > r^*$. This resulted in multiplication of the pre-exponential factor in equation (3.27) by a parameter Z, known as the Zeldovich factor, where:

$$Z = \frac{1}{r^*}\left(\frac{G^*}{3\pi k_B T}\right)^{\frac{1}{2}} \tag{3.28}$$

This result for the nucleation rate per unit volume has formed the basis of almost all subsequent work, the main differences between developments of the Becker–Döring theory being the choice of the pre-exponential factor. For the nucleation of a solid phase, the kinetics of gaseous collisions used in the above approach are no longer applicable, so the frequency term for collisions between atoms and critical nuclei must be modified accordingly. It can be considered as the product of an atomic vibration frequency and an exponential term containing the activation energy for the transfer of atoms across the nucleus/matrix interface, Q. From reaction rate theory [44], the vibration frequency is $k_B T/h$. Therefore, the rate at which an atom in contact with a nucleus will transfer into it is:

$$\frac{k_B T}{h}\exp\left\{-\frac{Q}{k_B T}\right\} \tag{3.29}$$

and thus:

$$I_v = \frac{k_B T}{h} n_v Z \exp\left\{-\frac{(G^* + Q)}{k_B T}\right\} \tag{3.30}$$

3.1.4.2 Heterogeneous Nucleation Sites

The basic theory described above considers nucleation as a homogeneous process, occurring with equal probability in all regions of the assembly. In reality, nucleation will be favoured on inhomogeneities within the material, such as defects, grain boundaries and impurities. These are high energy sites due to the surface area created between them and the matrix, and nucleation of more coherent particles in their place can lead to a reduction in free

energy. In the case of ferrite nucleating from austenite, prior austenite grain boundaries are the favoured sites. If the effects of strain energy are unimportant or neglected, (Lee *et al.* [45] demonstrated that strain energy would only influence the critical nucleus shape if it was a large fraction of the volume free energy change for nucleation), then the driving force for nucleation at a particular site will depend on the reduction in free energy due to removal of the high energy grain boundary surface. Destruction of this surface provides the energy for formation of the new nucleus surface and volume. There are three types of grain boundary site to consider: grain faces, edges and corners (Figure 3.7). For each type of site, the two most important factors are the density of sites and the probability of nucleation at that site (in other words, how energetically favourable it would be to form a nucleus). The first theoretical treatment of this was due to Cahn in 1956 [46], who utilised the geometrical calculations of Clemm and Fisher [47]. Cahn justified a nucleation rate per unit volume of the form:

$$I_v = \frac{k_B T}{h} n_v \rho_j \exp\left\{-\frac{(K_2^j G^* + Q)}{k_B T}\right\} \tag{3.31}$$

where ρ_j is a density of sites factor, representing the number of sites of a particular type available for nucleation, and K_2^j is a "shape factor" for the sites of different dimensionality, j. $j = 3$ for homogeneous nucleation, 2 for faces, 1 for edges and 0 for corners. ρ_j is approximately equal to $(\delta/d_\gamma)^{3-j}$, where δ is the effective grain boundary thickness and d_γ is the austenite grain size. (Cahn assumes the grains to be tetrakaidecahedra, with d_γ being defined specifically as the distance between the square faces in (100) planes). The number of atoms per unit volume on the three types of sites can be expressed as [48]:

$$\begin{aligned} n_v^f &= n_v \left(\frac{\delta}{d_\gamma}\right) \\ n_v^e &= n_v \left(\frac{\delta}{d_\gamma}\right)^2 \\ n_v^c &= n_v \left(\frac{\delta}{d_\gamma}\right)^3 \end{aligned}$$

where the superscripts f, e and c indicate faces, edges and corners, respectively. This will obviously always give a greater number of face sites than edges and then corners, as would be expected from consideration of an ideal equiaxed grain shape and also reflects the decrease in the number of possible sites per unit volume as austenite grain size increases (and thus boundary area per unit volume decreases).

The shape factor is a function of the ratio of the free energy required to form a grain boundary nucleus to that needed for homogeneous nucleation. Sites of lower dimensionality lead to smaller ratios (Figure 3.8), so that corner sites are more favourable than edges,

which are more favourable than faces. Corners are the junctions of four grain boundaries, so there will be the greatest reduction in the free energy if this region of boundary is removed. Homogeneous nucleation is the least energetically favourable process.

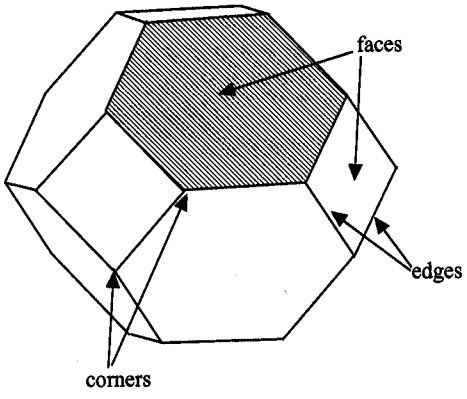

Figure 3.7: Schematic diagram of an austenite grain, showing the three types of nucleation site (after Tamura [49]).

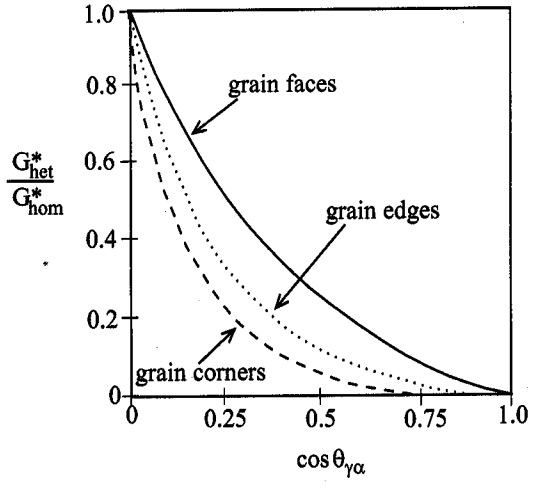

Figure 3.8: Ratio of free energy needed to form a heterogeneous, grain boundary nucleus to that required for homogeneous nucleation, for different nucleation sites, plotted as a function of the ratio of the interfacial energies, $\cos\theta_{\gamma\alpha} = \frac{\sigma_{\gamma\gamma}}{2\sigma_{\gamma\alpha}}$ [46, 43].

3.1.4.3 Heterogeneous Nucleation Shape Factors

The shape factors for the three types of site, as derived by Clemm and Fisher and later verified by Christian, are determined as follows. For nucleation on a boundary, the area of boundary between two γ grains eliminated by the α nucleus is ar^2 where r is the radius of curvature of the nucleus surfaces. The new surface area formed between grains of γ and α is br^2 and the volume of the new nucleus is cr^3 where a, b and c are functions of the grain boundary energies and shape. G^* now becomes:

$$G^* = \frac{4(b\sigma_{\gamma\alpha} - a\sigma_{\gamma\gamma})^3}{27c^2\Delta G_v^2} \tag{3.32}$$

where $\sigma_{\gamma\gamma}$ is the interfacial energy between two γ grains. The values of a, b and c need to be determined for each type of boundary site.

At faces or two-grain junctions, an isotropic nucleus in an isotropic matrix will have the shape of a symmetrical lens, the dihedral angle, $\theta_{\gamma\alpha}$, being determined by the static equilibrium of the interfacial energies (Figure 3.9):

$$\sigma_{\gamma\gamma} = 2\sigma_{\gamma\alpha}\cos\theta_{\gamma\alpha} \tag{3.33}$$

All the interfacial energies are assumed to be isotropic. Clemm and Fisher found that:

$$\begin{aligned} a &= \pi(1-\cos^2\theta_{\gamma\alpha}) \\ b &= 4\pi(1-\cos\theta_{\gamma\alpha}) \\ c &= \frac{2\pi}{3}(2-3\cos\theta_{\gamma\alpha}+\cos^3\theta_{\gamma\alpha}) \end{aligned}$$

The ratio of the activation energy of a critical nucleus on a grain face, G_f^*, to that for homogeneous nucleation is then:

$$\frac{G_f^*}{G^*} = K_2^f = \frac{1}{2}(2-3\cos\theta_{\gamma\alpha}+\cos^3\theta_{\gamma\alpha}) \tag{3.34}$$

where K_2^f is the shape factor for face nucleation.

At edges or three-grain junctions, the nucleus is bounded by three spherical surfaces, and the dihedral angle is determined as before at the edge between two $\gamma-\alpha$ surfaces and a $\gamma-\gamma$ surface. The ratio of the edge and homogeneous activation energies is:

$$\frac{G_e^*}{G^*} = K_2^e = \frac{9\pi}{4}\cos^{-1}\left\{\frac{\cos\theta_{\gamma\alpha}}{[3(1-\cos^2\theta_{\gamma\alpha})]^{\frac{1}{2}}}\right\}(1-\cos^2\theta_{\gamma\alpha})-\cos\theta_{\gamma\alpha}(3-4\cos^2\theta_{\gamma\alpha})^{\frac{1}{2}} \tag{3.35}$$

At corners or four-grain junctions, the nucleus may have the shape of a spherical tetrahedron, and the equations for a, b and c become yet more complex [47]. The ratio of

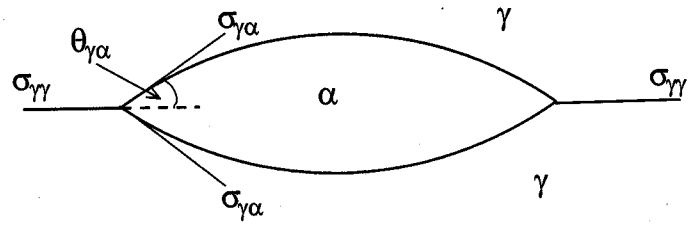

Figure 3.9: Formation of an α nucleus on a γ grain boundary face, illustrating the interfacial energies and the dihedral angle, $\theta_{\gamma\alpha}$ (after Clemm and Fisher [47]).

the corner and homogeneous activation free energies becomes:

$$\frac{G_c^*}{G^*} = K_2^c = \frac{9\pi}{4}\left[2\sin^{-1}\left\{\frac{q}{2(1-\cos^2\theta_{\gamma\alpha})^{\frac{1}{2}}}\right\}(1-\cos^2\theta_{\gamma\alpha}) - q\left[\left(1-\cos^2\theta_{\gamma\alpha}-\frac{q^2}{4}\right)^{\frac{1}{2}} - \frac{q}{\sqrt{8}}\right]\right] \tag{3.36}$$

where

$$q = \frac{4}{3}\left(\frac{3}{2} - 2\cos^2\theta_{\gamma\alpha}\right)^{\frac{1}{2}} - \frac{2\cos\theta_{\gamma\alpha}}{3} \tag{3.37}$$

The shape factor in the exponential part of the nucleation rate equation is balanced by the density of sites term, ρ_j, which clearly reflects the greater number of face sites, followed by edges and then corners. Cahn used the ratio of these two opposing factors to investigate which type of sites would contribute most to the overall nucleation rate for particular values of K_2^j.

$$R_K = \frac{\ln(d_\gamma/\delta)}{G^*/k_BT} \tag{3.38}$$

He found that corners have the highest nucleation rate when $R_K < K_2^e - K_2^c$, edges when $K_2^e - K_2^c < R_K < K_2^f - K_2^e$, faces when $K_2^f - K_2^e < R_K < 1 - K_2^f$ and finally homogeneous nucleation dominates when $R_K > 1 - K_2^f$. Figure 3.10 shows a plot of these regions and it can be seen that the type of nucleation site which dominates is strongly dependent on the ratio $2\cos\theta_{\gamma\alpha} = \sigma_{\gamma\gamma}/\sigma_{\gamma\alpha}$. If $\cos\theta_{\gamma\alpha}$ is too small, then certain types of site will nucleate too slowly to ever be observed and nucleation on a site of higher dimension will dominate. So the choice of a value for $\theta_{\gamma\alpha}$ (or the ratio of the interfacial energies) is important.

Precise evaluation of the shape and sites factors is practically impossible, but estimates have been made by several researchers. Reed and Bhadeshia modified Cahn's equation for I_v to describe the rate of nucleation per unit grain boundary area, I_b [50]. They replaced the terms n_v and ρ_j with a term N_j, representing the number of sites per unit area of boundary actively supporting nucleation. N_j is defined as the total possible number of sites per unit area, $1/\delta^2$ (with the interatomic spacing δ taken as 2.5 Å), which assumes

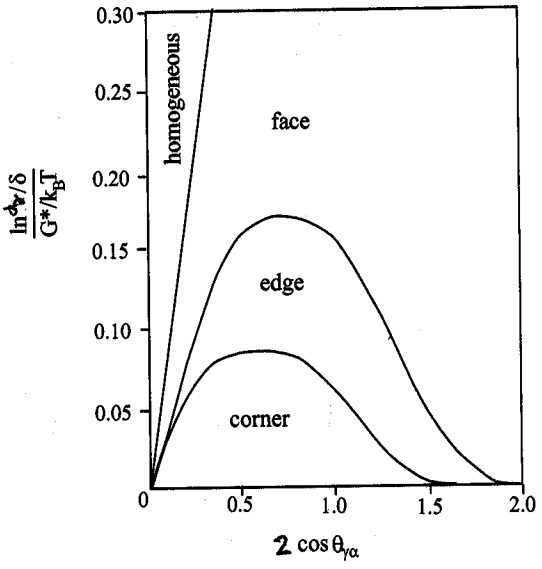

Figure 3.10: Illustration of the types of site which make the greatest contribution to the initial nucleation rate as a function of the ratio of the interfacial energies for each type of site (after Cahn [46]).

that every atom on the boundary is a potential site, modified by a factor which allows for "poisoning" of sites, K_1^j. This represents the fraction of these which are actually active. Therefore:

$$I_b^j = \frac{k_B T}{h} \frac{K_1^j}{\delta^2} \exp\left\{-\frac{(K_2^j G^* + Q)}{k_B T}\right\} \tag{3.39}$$

where K_2^j is the shape factor described previously and the superscript j denotes grain face, edge or corner sites (f, e or c, respectively). The overall nucleation rate is given by the sum of the individual rates at each site:

$$I_b = I_b^f + I_b^e + I_b^c \tag{3.40}$$

Reed and Bhadeshia used these equations in a model to predict TTT diagram C-curves. To determine the unknown parameters Q, K_1^j and K_2^j, they fitted their equations to a standard set of experimental TTT curves [51], investigating both equilibrium and paraequilibrium models for nucleation and growth. They concluded that paraequilibrium must be the operating mode, as the equilibrium results produced physically unrealistic values for the shape factors and less accurately predicted the shape of the TTT curves, particularly around the C-curve nose. The interfacial energy per unit area, $\sigma_{\gamma\alpha}$ was taken as 0.2 J m^{-2}. A value for Q, the activation energy for atoms crossing the austenite/ferrite nucleus interface, of 350 kJ mol^{-1} was determined. Table 3.1 shows their values for the site and shape factors.

Site	Site factor, K_1^j	Shape factor, K_2^j
Face	6.9×10^{-8}	2.6×10^{-3}
Edge	1.3×10^{-8}	1.0×10^{-3}
Corner	1.2×10^{-10}	3.3×10^{-3}

Table 3.1: Values of site and shape factors for nucleation rate equation [50].

3.1.5 Ferrite Grain Size

One of the most important steel parameters resulting from the hot-rolling process and subsequent phase transformations is the size of the allotriomorphic ferrite grains. In fact, refinement of the grain size is the rationale for much of the processing in the first place, as the grain size has a major influence on the mechanical properties of the final steel product. The Hall-Petch equation (1.1) relates the yield strength of the material to the inverse square root of the grain size – thus finer grains produce a large increase in strength. Grain sizes of only a few micrometres are often desirable and so any models attempting to predict this parameter must be accurate, as small variations at these sizes will lead to relatively large discrepancies in yield strength prediction. There are many empirical equations to compute grain size, as a function of cooling rate, austenite grain size and strain (the latter is important for transformations from deformed austenite) [4, 5, 6, 52, 53]. Although these can make reasonably accurate predictions there can also be large variations in results from different equations for the same conditions [4]. The main problem with such equations is that they don't properly account for steel composition. The fitting constants are only truly valid over the particular range of steels for which they were derived and cannot be relied upon to produce accurate results for other compositions. They are also limited to continuous cooling conditions, whereas modern steel processing routes often employ interrupted cooling schedules. Thus, a more theoretical approach is required, using the nucleation and growth theories described in this chapter which can take full account of the composition and cooling profile *via* thermodynamic parameters.

Ferrite grains nucleate at prior austenite grain boundaries and subsequently grow into the grains under carbon diffusion control. The final ferrite grain size will therefore be dependent on the austenite grain size, nuclei density (nucleation rate) and growth kinetics. Assuming that each ferrite grain occupies an equal volume, the nominal ferrite grain size (diameter) can be expressed as [54]:

$$d_\alpha = \left(\frac{2}{3N_v}\right)^{\frac{1}{3}} \tag{3.41}$$

where N_v is the total number of ferrite particles per unit volume. The problem is thus

reduced to correct determination of N_v. When homogeneous nucleation occurs, then the number of nuclei formed per unit volume in a time interval dt can be calculated from the nucleation rate per unit volume, I_v. The total number of nuclei can then be found by integration over the total transformation. Allowance must be made for "phantom nucleation" occurring in regions already transformed. Thus [49],

$$N_v = \int_0^\infty I_v(1 - X_\alpha)\, dt \tag{3.42}$$

where X_α is the volume fraction of transformed ferrite. In the case of heterogeneous nucleation, the number of nuclei per unit area of austenite grain boundary, N_s, can be similarly determined, by substituting the boundary nucleation rate per unit area and the area fraction of transformed ferrite at the boundary for I_v and X_α respectively in the above equation. This can be converted into N_v by multiplication with the austenite grain boundary area per unit volume, S_v:

$$N_v = N_s S_v \tag{3.43}$$

Hence, the ferrite grain size around the austenite grain boundary can be calculated. However, this assumes that all grains are of equal size, which is clearly not the case in practice. The above method makes no allowance for a *distribution* of ferrite grain sizes. Indeed, the Avrami extended volume analysis commonly used to determine overall transformation kinetics (Section 3.2.1) does not allow the progress of individual particles to be followed, it only computes the transformation behaviour of the whole system. Abbruzzese [55] developed further an existing statistical distribution model for ferrite grain development. The grains are divided into classes according to the size of their radii. The number of new grains in the first class in each time interval is determined from the nucleation rate per unit volume. A flow of grains between adjacent classes is permitted as new grains nucleate and existing ones grow. It is assumed that the array of grains is completely random, and that the surroundings of each grain are homogeneous [56]. The mean radius and frequency of each class is determined, which reduces the number of differential equations required. Application of the continuity equation enables the evolution of the grain size distribution with time to be calculated numerically. This method was incorporated by Anelli and co-workers into their transformation model [57].

A key assumption in all of the ferrite grain size calculations discussed above is that one ferrite nucleus grows to form one grain in the final microstructure. However, recent experimental work by Priestner and Hodgson, particularly in deformed austenite, suggested that the number of ferrite nuclei actually decreases as transformation proceeds, due to coalescence between adjacent grains [58]. The driving force for a ferrite grain to continue growing into untransformed austenite is normally higher than that for consumption of other ferrite grains, so the reason for these observations is still unclear.

3.2 Overall Transformation Kinetics

3.2.1 Introduction

The basic theory that is currently used to describe the overall kinetics of a phase transformation was formalised in the 1930s and 40s by Johnson and Mehl [59] and Avrami [60, 61, 62]. The starting points are the nucleation concepts introduced in Section 3.1.4, of heterophase fluctuations in the existing phase leading to regions (nuclei) of a new phase forming. The distribution of these nuclei possesses a critical size, r^*. Those nuclei of size $r < r^*$ are more likely to shrink and redissolve whereas those with $r > r^*$ will continue growing to form particles or grains of the new phase. Avrami considered the new phase to be nucleated by "germ nuclei" which already existed in the old phase as a function of its prior treatment (*e.g.* inclusions, defects, grain boundary junctions). Activation of some proportion of these nuclei beyond the critical size led to the formation of "growth nuclei", or grains of the new phase, and a decrease in the number density of "germ nuclei". Avrami also introduced the idea of a *characteristic time scale* for the transformation process, which enables the kinetics to be described independently of temperature and concentration and thus general solutions to a range of reaction kinetics problems can be found. He considered that the variation of the nucleation rate per potential nucleus per unit time and the average growth rate per unit time with external factors such as temperature and concentration was similar. Thus, the nucleation rate and the growth rate are approximately proportional over a range of temperatures and concentrations known as the *isokinetic range.* This allows easier solution of expressions for the number density of transformed particles and the volume fraction of transformed material, as will be demonstrated later.

To avoid complex statistical considerations, it is assumed that the centres of the new grains are distributed completely randomly within the volume of material. Avrami also notes [61] that a random distribution should be "applicable with a good approximation" to situations where the nuclei tend to segregate to boundaries in the structure of the old phase, such as solid-solid phase changes in metals.

3.2.2 Basic Theory

3.2.2.1 Homogeneous Nucleation

Consider a single new phase, α, nucleating randomly in an existing phase, γ, at a constant nucleation rate per unit volume, I_α, and growing isotropically at a constant rate G_α to form spherical particles. The radius of a particle, nucleated at a time τ, at a later time t

can be written as:

$$r_\alpha = G_\alpha(t-\tau) \tag{3.44}$$

and thus the volume of the particle is,

$$v_\alpha = \begin{cases} \frac{4\pi}{3}G_\alpha^3(t-\tau)^3, & (t>\tau) \\ 0, & (t\leq\tau) \end{cases} \tag{3.45}$$

The number of particles formed in the time interval from $t=\tau$ to $t=\tau+d\tau$ is

$$N_\alpha = I_\alpha V\, d\tau \tag{3.46}$$

where V represents the total volume of the assembly. Thus, the total contribution to the transformed volume of α for all particles nucleated in the time interval between τ and $\tau+d\tau$ can be expressed as:

$$dV_\alpha^e = v_\alpha N_\alpha = \frac{4\pi}{3}G_\alpha^3(t-\tau)^3 I_\alpha V\, d\tau \tag{3.47}$$

The change in volume of α, dV_α^e, in equation 3.47 is designated the change in *extended* volume of α. At the early stages of transformation, whilst the individual nuclei are well-spaced (Figure 3.11a), the above theory adequately describes the transformation kinetics. However, once the growing particles start to impinge (Figure 3.11b) then allowances for this must be made. Avrami [60] introduced the concept of an "extended volume" to describe the volume of the particles had their growth not been impeded by impingement upon other particles. Particles are permitted to overlap and grow through each other. New nuclei forming in regions already transformed to α, dubbed "phantom nuclei", are also included in the extended volume calculation.

The *actual* change in volume, dV_α, can be determined from the change in extended volume by allowing for the probability that some transformation has occurred in previously transformed material:

$$dV_\alpha = \frac{4\pi}{3}G_\alpha^3(t-\tau)^3 I_\alpha V\left(1-\frac{V_\alpha}{V}\right) d\tau \tag{3.48}$$

where V_α is the volume of matrix already transformed to α. From 3.47 and 3.48 it follows that:

$$dV_\alpha = \left(1-\frac{V_\alpha}{V}\right) dV_\alpha^e \tag{3.49}$$

Separating the variables and integrating, we get:

$$V_\alpha^e = -V\ln\left(1-\frac{V_\alpha}{V}\right) \tag{3.50}$$

therefore

$$-\ln\left(1-\frac{V_\alpha}{V}\right) = \frac{4\pi}{3}\int_0^t I_\alpha G_\alpha^3(t-\tau)^3\, d\tau \tag{3.51}$$

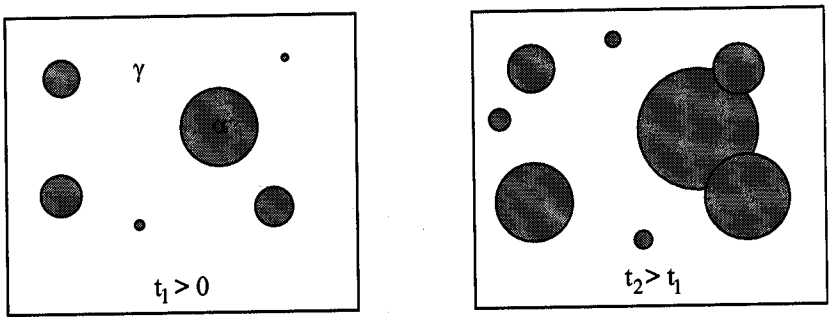

(a) (b)

Figure 3.11: Schematic illustration of growing particles of a single phase α transforming from a parent phase γ, (a) early stages, before impingement, and (b) after particle impingement.

Over the total time of transformation, for all particles nucleated after all incubation times τ, the extent of reaction, ξ_α, can be determined as:

$$\xi_\alpha = \frac{V_\alpha}{V} = 1 - \exp\left\{-\frac{4\pi}{3}\int_0^t I_\alpha G_\alpha^3 (t-\tau)^3\, d\tau\right\} \tag{3.52}$$

For I_α and G_α constant with respect to time, this expression can be readily evaluated, thus enabling the progress of the phase transformation with time to be followed.

3.2.2.2 Heterogeneous Nucleation

The above theory can be extended to heterogeneous transformations, such as the nucleation of ferrite at austenite grain boundaries. Consider spherical particles of α forming as above. To determine the volume of α formed due to nucleation and growth from a grain boundary, we consider a series of planes parallel to the boundary and spaced a distance dy apart. If the radius of a particle exceeds the distance y of a plane from the boundary, then the area of intersection of that particle with the plane is determined (Figure 3.12). The total of such areas of intersection on one plane for all particles growing from the boundary is the *extended area* of transformation on that plane.

If the area of intersection is $\pi r_\alpha^2 = \pi\left[G_\alpha^2(t-\tau)^2 - y^2\right]$, then the change in extended area of α on one plane due to particles emanating from one boundary in the time interval from τ to $\tau + d\tau$ can be expressed as:

$$dO_\alpha^e = \pi O_b I_{\alpha,b}[G_\alpha^2(t-\tau)^2 - y^2]\, d\tau \tag{3.53}$$

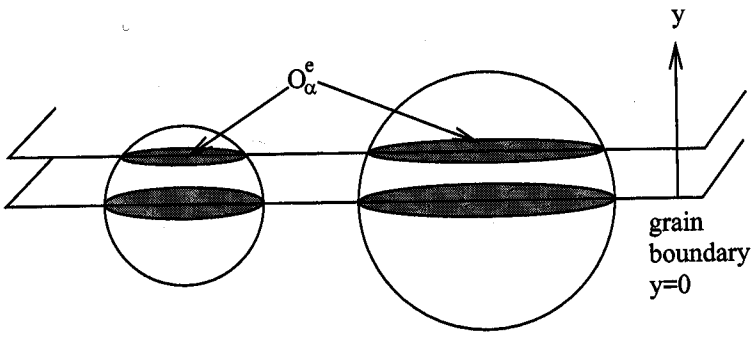

Figure 3.12: Schematic illustration of spherical particles growing from a grain boundary and intersecting a parallel plane a distance y from the boundary.

for $r_\alpha > y$, otherwise $dO^e_\alpha = 0$. O_b is the total area of the plane and $I_{\alpha,b}$ is the nucleation rate of α per unit area of boundary. Assuming that $I_{\alpha,b}$ is constant, substituting $\phi = \frac{y}{G_\alpha t}$, and integrating over all incubation times, from $\tau = 0$ to $\tau = t - y/G_\alpha$, the total extended area of α on one plane is obtained:

$$O^e_\alpha = \frac{\pi}{3} O_b I_{\alpha,b} G^2_\alpha t^3 (1 - 3\phi^2 - 2\phi^3) \tag{3.54}$$

If it is assumed that there is no interference from particles emanating from other grain boundaries, then the total volume of α originating from one boundary, $V_{\alpha,b}$, can be calculated by integrating the extended area over all the planes y from zero to (positive) infinity ($\phi = 0$ to $\phi = 1$).[1] Thus,

$$V_{\alpha,b} = O_b G_\alpha t \left[\int_0^1 1 - \exp\left\{ -\frac{\pi}{3} I_{\alpha,b} G^2_\alpha t^3 (1 - 3\phi^2 - 2\phi^3) \right\} d\phi \right] \tag{3.55}$$

If the total area of all the grain boundaries is O_B, then by substituting this for O_b in the equation above we get the total *extended* volume transformed from all boundaries – extended because no allowance has been made for the overlap of regions emanating from different boundaries, so-called "hard impingement". If V is the total volume of the assembly as before and S_v the grain boundary surface area per unit volume, then:

$$\frac{V^e_\alpha}{V} = \frac{V_{\alpha,b} S_v}{O_b} \tag{3.56}$$

From equation 3.50:

$$\frac{V_\alpha}{V} = 1 - \exp\left\{ -\frac{V^e_\alpha}{V} \right\} \tag{3.57}$$

[1] This assumes that the particle only grows from one side of the boundary. In some instances (such as allotriomorphic ferrite), the particle can grow from both sides, thus the integration over y is performed from negative to positive infinity, which effectively introduces a factor of 2 before O_b in equation 3.55.

The extent of reaction, ξ_α, is therefore:

$$\xi_\alpha = \frac{V_\alpha}{V} = 1 - \exp\left\{-S_v G_\alpha t \left[\int_0^1 1 - \exp\left\{-\frac{\pi}{3} I_{\alpha,b} G_\alpha^2 t^3 (1 - 3\phi^2 - 2\phi^3)\right\} d\phi\right]\right\} \quad (3.58)$$

The volume fraction of a single phase forming spherical particles, with constant nucleation and linear growth rates, homogeneously or heterogeneously within a matrix phase can now be calculated. In practice, particles can have many different morphologies and modes of growth. The shape of the particle, be it a sphere, plate, disc, ellipsoid, *etc.*, affects the geometrical factor in the exponential term in equation 3.58. The mode of growth alters the exponents of the growth rate and time t. Consider for example the parabolic growth of disc-shaped particles of α with aspect ratio (radius to thickness) η_α, nucleated at a time τ on a grain boundary, and growing such that the thickness q_α of a disc perpendicular to the boundary at a later time t is given by:

$$q_\alpha = G_\alpha (t - \tau)^{\frac{1}{2}} \quad (3.59)$$

and its radius r_α parallel to the boundary is:

$$r_\alpha = \eta_\alpha G_\alpha (t - \tau)^{\frac{1}{2}} \quad (3.60)$$

The contribution to the extended area of α on the plane at y due to particles nucleated between τ and $\tau + d\tau$ is then:

$$dO_\alpha^e = \pi O_b I_{\alpha,b} \eta_\alpha^2 G_\alpha^2 (t - \tau)\, d\tau \quad (3.61)$$

Substituting $\phi = \frac{y}{G_\alpha t^{\frac{1}{2}}}$ and proceeding as before, we now obtain:

$$\xi_\alpha = 1 - \exp\left\{-S_v G_\alpha t^{\frac{1}{2}} \left[\int_0^1 1 - \exp\left\{-\frac{\pi}{2} I_{\alpha,b} \eta_\alpha^2 G_\alpha^2 t^2 (1 - \phi^4)\right\} d\phi\right]\right\} \quad (3.62)$$

Note the differences in the factor of π, and the exponents of t and ϕ compared with equation 3.58.

3.3 The Pearlite Transformation

Pearlite is a lamellar structure of ferrite and cementite (Fe_3C), which forms below the eutectoid temperature (723 °C in plain carbon steels). The austenite transforms by a reconstructive mechanism, in which carbon and substitutional alloying elements redistribute between the ferrite and cementite. Pearlite nodules can nucleate on austenite grain boundaries, allotriomorphic ferrite grains or on cementite particles, depending upon the steel composition. In low alloy steels, nucleation on γ/α boundaries predominates as allotriomorphic ferrite is usually the first phase to develop on cooling before pearlite, whereas in eutectoid steels pearlite nucleates on the austenite grain boundaries.

3.3.1 Thermodynamics of the Pearlite Transformation

The pearlite transformation can start once the eutectoid temperature, T_e, has been reached (Ae_1 on the Fe-C phase diagram, Figure 1.3). This temperature can be raised or lowered by ferrite stabilising (Cr, Mo, Si) or austenite stabilising (Ni) elements, respectively. A second criterion for the start of transformation during non-equilibrium cooling is that the carbon content of the austenite exceeds that required for cementite formation, $x^{\gamma\theta}$. This latter value can be deduced using the Hultgren extrapolation of the austenite/cementite (γ/θ) phase boundary (A_{cm}) to the required temperature [63, 64]. Unlike ferrite, pearlite never forms by a paraequilibrium mechanism, so local equilibrium must be maintained. It is suggested that if PLE predominates, then the alloying elements partition into the cementite and therefore the diffusivity of X in austenite is the rate-controlling step. On the other hand, austenite stabilisers with a low solubility in cementite encourage NPLE, and carbon diffusion in austenite is rate-controlling [65]. An important pearlite parameter is the spacing of the lamellae, S, because this has a direct effect on the strength of the steel, larger spacing leading to lower yield strength and UTS [38]. The lamellar spacing is inversely proportional to the degree of undercooling below T_e, a large undercooling thus producing a finer pearlite. The spacing is related to a balance between the free energy for the transformation, the increase in surface energy due to the creation of new ferrite/cementite interfaces and perhaps the stability of the moving interface.

3.3.2 Kinetics of the Pearlite Transformation

The pearlite/austenite interface is incoherent, the pearlitic ferrite and cementite having no orientation relationship with the austenite grain into which they are growing. There is a well-defined orientation relationship between the ferrite and cementite crystals within a pearlite nodule, however [65]. For growth to occur, carbon and substitutional elements may redistribute ahead of the transformation interface by volume diffusion in austenite or by diffusion along the transformation interface. The Zener-Hillert growth model [66, 67] assumes that the austenite has periodic compositional variations along the interface, corresponding to the ferrite and Fe_3C lamellae. The following expression for the growth rate of pearlite controlled by volume diffusion of carbon in austenite ahead of the interface was deduced:

$$G_p^v = \frac{D_C^v}{g}\left[\frac{S^2\left(x_C^{\gamma\alpha} - x_C^{\gamma\theta}\right)}{S_\alpha S_\theta\left(x_C^{\theta\gamma} - x_C^{\alpha\gamma}\right)}\frac{1}{S}\left(1 - \frac{S_c}{S}\right)\right] \tag{3.63}$$

where D_C^v is the volume diffusion coefficient of carbon in austenite, g is a geometric factor (equal to 0.72 in a eutectoid steel), S_c is the critical interlamellar spacing at which the growth rate becomes zero, S_α and S_θ are the thicknesses of the ferrite and cementite

lamellae, and $x_C^{\gamma\alpha}$ and $x_C^{\gamma\theta}$ are the carbon concentrations in austenite in local equilibrium with Fe_3C at the γ/α interface and the γ/θ interface, respectively.

The growth rate in the case where boundary diffusion of a substitutional element X is the rate-controlling step is [68]:

$$G_p^b = 12KD_X^b\delta\left[\frac{S^2(x_X^{\gamma\alpha} - x_X^{\gamma\theta})}{S_\alpha S_\theta \overline{x}_X}\frac{1}{S^2}\left(1 - \frac{S_c}{S}\right)\right] \tag{3.64}$$

where: K is the boundary segregation coefficient of X (the ratio between the alloying element concentration in austenite near the boundary to that in the boundary), D_X^b is the boundary diffusion coefficient of X, δ is the width of the boundary, $x_X^{\gamma\alpha}$ and $x_X^{\gamma\theta}$ are the concentrations of X in austenite at the γ/α and γ/θ interfaces, respectively, and $\overline{x}_X$ is the average substitutional alloying element concentration in the alloy.

The values of S and S_c can be estimated empirically [64] and it is assumed that S adopts a value consistent with the maximum growth rate [67], such that $S = 2S_c$ with $S_c = \frac{2\sigma_{\alpha\theta}T_e}{\Delta H \Delta T}$. $\sigma_{\alpha\theta}$ is the ferrite/cementite interfacial energy, ΔH is the change in enthalpy between parent and product phases and ΔT is the undercooling below the eutectoid temperature, T_e.

The nucleation rate of pearlite can be treated using the classical theory of heterophase fluctuations as described in Section 3.1.4. The density of available nucleation sites will depend upon the amount of prior austenite grain boundary and also the γ/α interface area. This can be evaluated from the fraction of allotriomorphic ferrite transformed and the extended area covered by the ferrite grains per unit volume [57, 69, 70]. The shape of a pearlite nodule can be idealised as a hemisphere, the flat face coincident with the grain boundary, the incoherent curved interface growing into the austenite grain [38]. Other morphologies such as spheres have been considered [70]. Umemoto also included the additional restriction on nucleation that the γ/α interface must be moving sufficiently slowly for cementite to nucleate upon it. This is equivalent to the incubation time for cementite nucleation being shorter than the time taken for the interface to move a distance equal to the radius of the critical nucleus [70].

The overall kinetics of the pearlite transformation can once again be treated using the Johnson-Mehl-Avrami analysis for homogeneous and heterogeneous nucleation discussed in Section 3.2.1. Pearlite transforms by a typical nucleation and growth process, the nodules nucleating at preferential sites in the austenite and then growing until impingement. Cahn and Hagel [71] pointed out that grain corners were the most effective sites, which nucleated rapidly leading to early site saturation. The rest of the transformation would then be controlled by the radial growth of the pearlite nodules. Assuming a constant growth velocity and saturation of corner sites, the fraction of austenite transformed is:

$$\xi_p = 1 - \exp\left\{-\frac{4\pi}{3}n_v^c G_p^3 t^3\right\} \tag{3.65}$$

where n_v^c is the number of grain corner sites per unit volume. Note that once rapid site saturation has occurred, the nucleation rate no longer plays a part in the transformation.

3.4 Summary

The theory of reconstructive phase transformations as applicable to allotriomorphic ferrite and pearlite has been reviewed. The origins of the driving forces for the austenite to ferrite transformation and for ferrite nucleation have been outlined. Methods for determination of the diffusivity of carbon in austenite and the growth rate constant of allotriomorphic ferrite have been described. In multicomponent steels, the kinetics can be simplified by assuming that growth occurs under paraequilibrium conditions, where there is no redistribution of the substitutional solutes.

The classical nucleation theory of heterophase fluctuations and the derivation of the nucleation rate equation have been explained. The theory can be adapted to cater for the variety of austenite grain boundary sites at which allotriomorphic ferrite nucleates by modification of the matrix/nucleus interfacial energy and the density of active sites. The ferrite grain size can be calculated by following the evolution of ferrite nuclei throughout the transformation.

Pearlite can form below the eutectoid temperature once the composition of the austenite reaches the cementite phase boundary. It grows under local equilibrium conditions with either volume diffusion of carbon or boundary diffusion of a substitutional element as the rate-controlling step. Classical nucleation theory is again applicable, with both γ/γ and γ/α interfaces providing potential nucleation sites.

The Johnson-Mehl-Avrami theory of overall transformation kinetics has been described in detail, for both homogeneous and heterogeneous nucleation with linear and parabolic growth rates. This theory is a key component of the transformation model which has been developed in this work and will be expanded further in Chapter 7.

Chapter 4

Displacive Transformations

As the degree of undercooling, $\Delta T = Ae_3 - T$, below the Ae_3 temperature increases, different transformation products can form from the austenite. The driving force for the transformation increases with ΔT, and so the formation of phases with larger strain energies or non-equilibrium compositions can be accommodated. Diffusion of solute elements becomes sluggish at lower temperatures and therefore displacive transformations predominate. Widmanstätten ferrite, bainite and martensite can all be classified as displacive transformation products.

4.1 Widmanstätten Ferrite and Bainite Transformations

4.1.1 Widmanstätten Ferrite

Widmanstätten ferrite (α_w) is a phase formed by the transformation of austenite below the Ae_3 temperature. It often forms simultaneously and competitively with allotriomorphic ferrite and pearlite.. However, Widmanstätten ferrite can also occur at temperatures where the reconstructive transformations are sluggish due to the very low mobility of atoms. It nucleates heterogeneously, either directly from the austenite grain boundaries, (*primary* Widmanstätten ferrite), or on the austenite/allotriomorphic ferrite interfaces (*secondary* Widmanstätten ferrite). When examined optically, it takes the form of long, thin pointed plates, often emanating in parallel packets from the grain boundaries (Figure 4.1a), or as plates growing from alternate sides of the boundary (Figure 4.1b). The growth of Widmanstätten ferrite leads to an invariant-plane strain (IPS) shape change with a large shear component. This indicates that the substitutional lattice is displaced during transformation. However, in order to minimise strain energy, pairs of plates grow together in a mutually accommodating formation [72]. The interstitial carbon atoms are able to

diffuse during growth without affecting the shape change. The elastically accommodated strain energy accompanying growth is relatively small (compared with that for bainite or martensite), consistent with the low undercooling below the Ae_3 at which α_w can form. The strain energy has been evaluated as about 50 J mol^{-1} [72]. This has the effect of raising the ferrite free energy curve and thus lowering the temperature below which Widmanstätten ferrite growth can in principle occur, Ae_3^w (Figure 4.2). As the only diffusion during transformation is that of carbon ahead of the advancing plate tip, the Widmanstätten ferrite transformation is said to occur by a paraequilibrium mode in which the lattice change is achieved by a deformation.

4.1.2 Bainite

Bainite consists of a non-lamellar aggregate of ferrite and carbides and generally forms at temperatures lower than Widmanstätten ferrite. It is usually classified into two forms. *Upper bainite* forms at relatively high temperatures and consists of fine, bainitic ferrite laths surrounded by carbide particles, the latter having formed from the carbon-enriched residual austenite surrounding the laths. *Lower bainite* forms at lower temperatures where a fine dispersion of carbides can also precipitate directly within the ferrite laths.

The decomposition of austenite to bainite can be considered to occur by a displacive mechanism, giving rise once again to an IPS shape change in the transformed region [30]. The stored strain energy due to this shape deformation, which is a single IPS, is larger than for Widmanstätten ferrite, and has been evaluated as 400 J mol^{-1} [72]. Umemoto *et al.* using their own thermodynamic program re-calculated the stored energy values as 300 and 600 J mol^{-1}, respectively, for Widmanstätten ferrite and bainite [70]. Bainite transformation usually initiates at the prior austenite grain boundaries, where sheaves of bainitic ferrite nucleate and grow into the austenite grains. Each sheaf consists of clusters of parallel platelets called *sub-units* (Figure 4.3) which grow very rapidly once nucleated and, it is suggested, without diffusion [74]. Any excess carbon in the bainitic ferrite is partitioned soon after the growth is arrested, into the residual austenite between the plates.

The driving force for the diffusionless growth of bainite can be determined from the difference in the free energies of austenite and ferrite of the same composition, $\Delta G^{\gamma\rightarrow\alpha}$, at a particular temperature. The locus of points on the Fe-C phase diagram at which $\Delta G^{\gamma\rightarrow\alpha} = 0$ and thus the composition at which bainite growth must cease describes the T_o line. Allowing for the stored energy shifts this line to lower temperatures and it is labelled T_o' (Figure 4.4). The diffusionless growth of bainitic ferrite becomes impossible when the carbon concentration of the residual austenite reaches the T_o' composition. The maximum volume fraction of bainite that can form at a particular temperature, determined

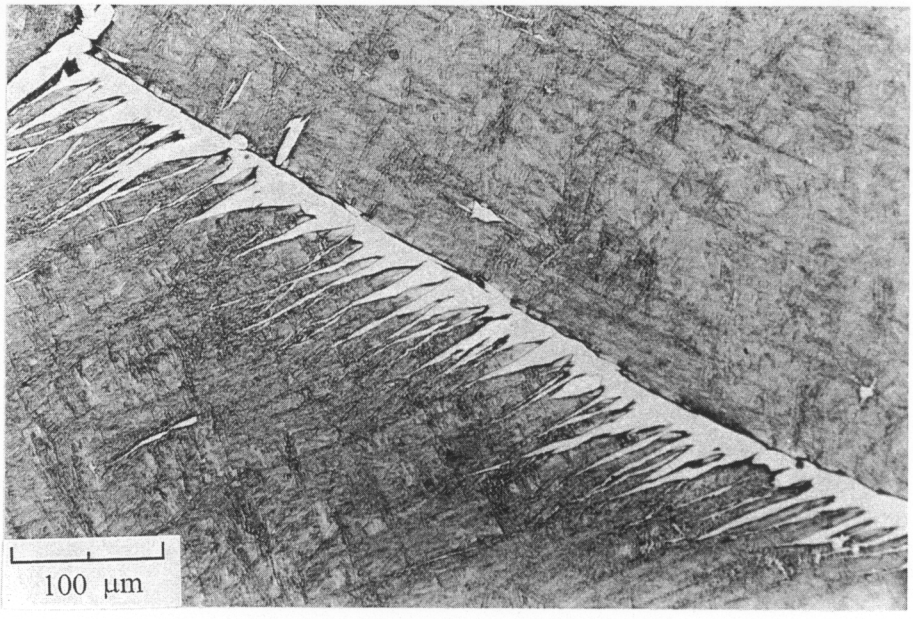

(a)

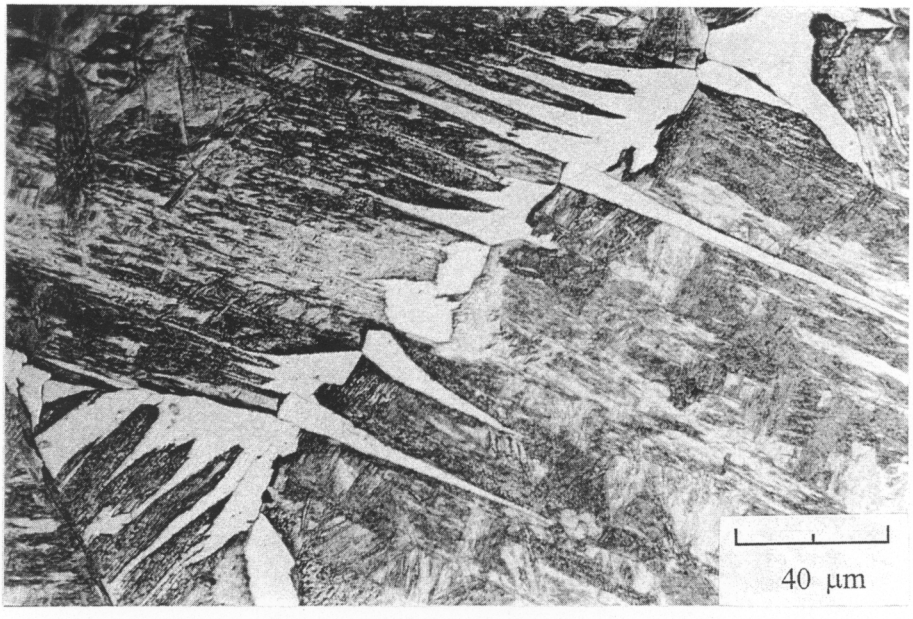

(b)

Figure 4.1: Optical micrographs showing the morphology of Widmanstätten ferrite, (a) parallel wedge-shaped plates emanating from one side of the austenite grain boundary, (b) plates growing from alternate sides of the boundary.

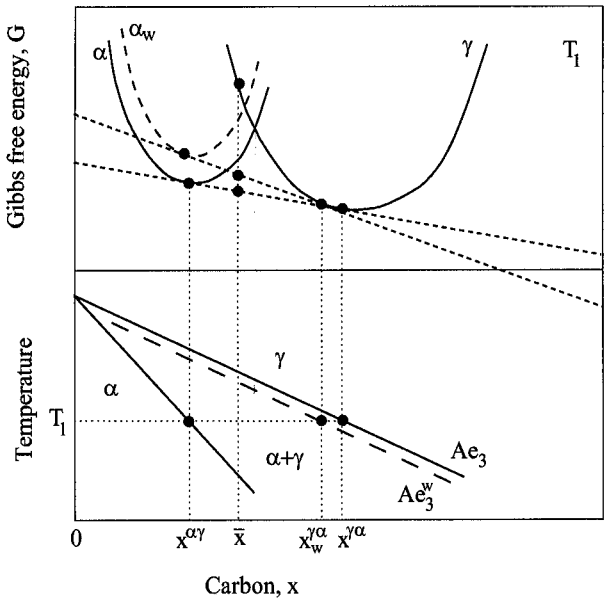

Figure 4.2: Free energy curves and corresponding phase boundaries for allotriomorphic ferrite (solid line) and Widmanstätten ferrite (dashed line) showing the effect of the 50 J mol^{-1} stored energy.

from the phase diagram is:

$$\theta_{\alpha_b} = \frac{x_{T_o'} - \overline{x}}{x_{T_o'} - x^{\alpha\gamma}} \tag{4.1}$$

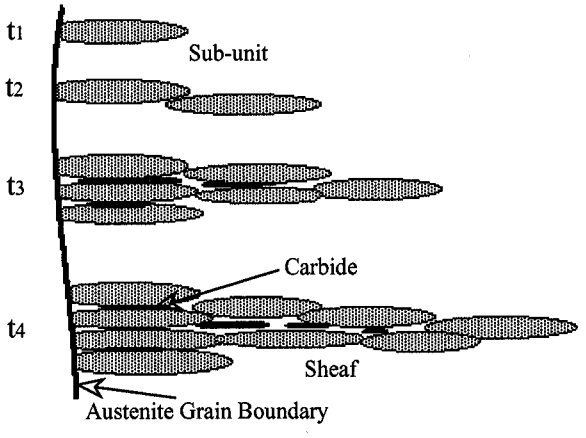

Figure 4.3: Schematic illustration of a bainite sheaf showing the repeated nucleation of sub-units at increasing times, t_1 to t_4 (after Bhadeshia [30]).

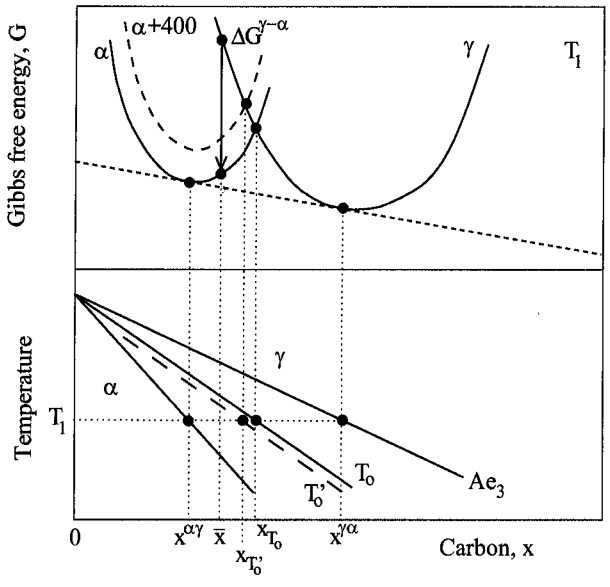

Figure 4.4: Calculated phase boundaries illustrating the T_o and T_o' curves and the driving force for diffusionless transformation, $\Delta G^{\gamma \rightarrow \alpha}$.

4.1.3 Displacive Nucleation

4.1.3.1 Nucleation Thermodynamics

The maximum driving force, ΔG_m, available for the formation of a Widmanstätten ferrite or bainite nucleus is the same as for an allotriomorphic ferrite nucleus, Section 3.1.1.1, and can be evaluated using the parallel tangent construction. A criterion must then be found to determine exactly when this driving force is sufficient for nucleation to begin. A time-temperature-transformation (TTT) diagram can be considered to consist of two overlapping C-curves – the upper curve representing reconstructive transformation and the lower one displacive reactions [25]. This lower curve has a characteristic flat top, representing the highest temperature, T_h, at which displacive transformation of austenite to ferrite is possible in a particular steel. Thus, T_h could correspond to either the Widmanstätten ferrite or bainite start temperature. The transformation start temperature is usually defined as the highest temperature at which a phase is observed to form at a detectable rate [30]. Bhadeshia calculated ΔG_m as a function of steel composition at T_h for a wide range of different steels for which the "bainite" start temperature had been carefully determined [73]. It was found that a plot of ΔG_m against T_h produced a straight line [72]. This curve was designated the *universal nucleation function*, G_N, and has the form:

$$G_N = 3.637T - 1537 \quad \text{J mol}^{-1} \tag{4.2}$$

It was also noted that if the driving force was calculated assuming no partitioning of carbon then for some compositions the driving force was positive, indicating that there must be redistribution of carbon during nucleation. Ali [75] further tested this theory on a standard set of TTT curves [51] and other published data [76, 77]. Regardless of whether T_h corresponded to the start of Widmanstätten ferrite or bainite formation, the same linear dependence of ΔG_m on temperature was found. Thus, it was considered that the nucleation mechanism of Widmanstätten ferrite and bainite is identical, subsequent growth conditions determining into which phase a potential nucleus develops. The first criterion that must be satisfied for a displacive transformation to occur is thus that the driving force for nucleation must exceed that required to obtain a detectable degree of transformation (point A on Figure 4.5):

$$\Delta G_m < G_N \tag{4.3}$$

If Widmanstätten ferrite is to form, then the driving force available for its growth must be sufficient to overcome the stored energy of 50 J mol^{-1}. The second criterion is, therefore:

$$\Delta G^{\gamma\rightarrow\gamma'+\alpha} < -50 \quad \text{J mol}^{-1} \tag{4.4}$$

where $\Delta G^{\gamma\rightarrow\gamma'+\alpha}$ is the chemical free energy change for transformation from austenite to a mixture of austenite and ferrite (point B). Alternatively, bainite will form instead if there is sufficient free energy available for the diffusionless formation of ferrite from austenite of the same composition, $\Delta G^{\gamma\rightarrow\alpha}$, below the T_o' temperature, allowing for the 400 J mol^{-1} stored energy. The second criterion then becomes (point C):

$$\Delta G^{\gamma\rightarrow\alpha} < -400 \quad \text{J mol}^{-1} \tag{4.5}$$

The temperature at which the two criteria are first satisfied defines the the Widmanstätten-start temperature, W_s, or the bainite-start temperature, B_s, respectively, Figure 4.5.

4.1.3.2 Nucleation Mechanism

The universal nucleation function G_N is directly proportional to temperature, and this fact can be used to shed some light on a possible mechanism for displacive transformation [30]. Equation 3.27 shows that the nucleation rate per unit volume varies with temperature as:

$$I_v \propto \nu \exp\left\{-\frac{G^*}{k_B T}\right\} \tag{4.6}$$

Rearrangement gives:

$$-G^* \propto \kappa T \tag{4.7}$$

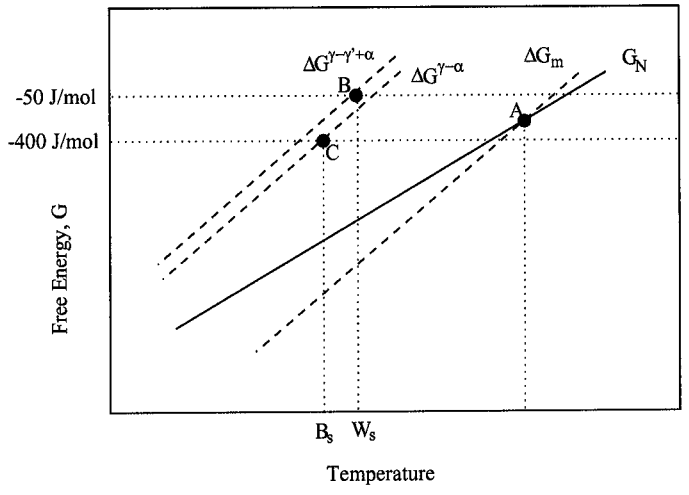

Figure 4.5: Schematic illustration of the driving forces for nucleation and growth of Widmanstätten ferrite and bainite, and how they define W_s and B_s.

where

$$\kappa = k_B \ln\{I_v/\nu\} \tag{4.8}$$

In the derivation of the G_N function, T_h corresponds to a temperature where the same detectable nucleation rate is obtained for all steels. It follows that κ is a constant for all steels and is negative, as the nucleation rate must be less than the attempt frequency ν, thus:

$$G_N \propto \kappa T \tag{4.9}$$

Therefore:

$$G^* \propto G_N \tag{4.10}$$

In classical nucleation theory there is an inverse square relationship between the activation energy and driving force for nucleation:

$$G^* \propto \frac{1}{\Delta G_v^2} \tag{4.11}$$

It can be clearly seen that this is not consistent with the nucleation of Widmanstätten ferrite and bainite described above. An alternative approach is provided by martensitic nucleation theory [78, 30], in which pre-existing embryos in the austenite become activated and develop into the new phase. In martensite, the embryos are considered to be a closely spaced group of stacking faults formed by the dissociation of other defects already present in the austenite. The nucleation event occurs when these defects become unstable and

dissociate, causing stacking faults on the close-packed planes and eventually forming a region of product phase. The nucleation kinetics are controlled by the movement of the embryo/matrix interface, which requires the passage of dislocations. The matrix opposes the dislocation motion by a frictional force, but the stacking fault energy (which normally opposes dissociation) becomes negative at the transformation temperatures concerned and thus actually drives the transformation by pushing the dislocations against the lattice resistance.

The free energy of the fault plane per unit area, G_F, is given by [30]:

$$G_F = n_P \rho_A (\Delta G_{chem} + \Delta G_s) + 2\sigma_{\gamma\alpha}\{n_P\} \tag{4.12}$$

where ΔG_{chem} is the chemical free energy difference between the parent and product phases, ΔG_s is the strain energy and $\sigma_{\gamma\alpha}$ is the embryo/matrix interfacial energy per unit area, a function of n_P, the number of close-packed planes involved in the faulting process. ρ_A is the density of atoms in the close-packed planes in moles per unit area. The force acting per unit length of the array of n_P dislocations bounding a fault embryo is $n_P \tau_o b$, where b is the Burgers vector and τ_o is the magnitude of the frictional shear stress in the lattice resisting the dislocation movement. The friction opposes the faulting, and thus the limiting condition at which a defect becomes unstable and "nucleation" occurs is:

$$G_F = -n_P \tau_o b \tag{4.13}$$

From the theory of thermally activated plastic deformation, in the absence of an applied shear stress, the activation energy for a dislocation to glide from one equilibrium position to another is given by G_o^* [30]. The application of a shear stress τ_o reduces this barrier to G^*:

$$G^* = G_o^* - (\tau_o - \tau_\mu) v^* \tag{4.14}$$

where v^* is an "activation volume" and τ_μ is the athermal resistance to dislocation motion. Combining equations (4.12) and (4.13) and substituting for τ_o into equation (4.14), the activation energy can be expressed as a function of the chemical driving force:

$$G^* = G_o^* + \left[\tau_\mu + \left(\frac{\rho_A}{b}\right)\Delta G_s + \left(\frac{2\sigma_{\gamma\alpha}}{n_P b}\right)\right] v^* + \left(\frac{\rho_A v^*}{b}\right)\Delta G_{chem} \tag{4.15}$$

It follows that G^* is directly proportional to the chemical driving force, in contrast to the classical nucleation theory of heterophase fluctuations. This suggests that the mechanism for Widmanstätten ferrite and bainite nucleation is displacive and similar to that of martensite, rather than reconstructive like allotriomorphic ferrite, although it still requires the partitioning of carbon.

4.1.4 Displacive Nucleation Rate

The classical equation for the nucleation rate per unit volume,

$$I_v = K_1 \exp\left\{-\frac{G^*}{RT}\right\} \tag{4.16}$$

can be modified in view of the linear dependence of G^* on driving force, ΔG_m, to give the displacive nucleation rate per unit volume:

$$I_{\alpha_b} = K_1 \exp\left\{-\frac{(K_2 + K_3 \Delta G_m)}{RT}\right\} \tag{4.17}$$

where K_i are empirical constants [79]. This original model of Bhadeshia was corrected and extended by Rees and Bhadeshia [80] to be consistent with the assumption made when deriving G_N that all steels have identical nucleation rates at W_s:

$$I_{\alpha_b} = K_1 \exp\left\{-\frac{K_2}{RT}\left(1 + \frac{\Delta G_m}{K_4}\right)\right\} \tag{4.18}$$

where K_1 is a constant expressing the density of nucleation sites as a function of austenite grain size,

$$K_1 = (\overline{L} K_1')^{-1} \tag{4.19}$$

$\overline{L}$ is the mean lineal intercept austenite grain size, K_1' is an empirical constant (see Table 4.1), $K_2 = 2065$ J mol^{-1} and $K_4 = 2540$ J mol^{-1}. ΔG_m was calculated allowing for the change in carbon concentration of the austenite as transformation proceeds, by varying it between its initial value, ΔG_m^o, and final value as a function of the extent of transformation, ξ_{α_b}:

$$\Delta G_m = \Delta G_m^o - \xi_{\alpha_b}(\Delta G_m^o - G_N) \tag{4.20}$$

The sub-unit model first proposed by Oblak and Hehemann [81] suggested that bainite sheaves grow by repeated nucleation of small sub-units with sympathetic nucleation of new sub-units occurring at the tips of existing ones. Transmission electron microscopy evidence for this was presented by Bhadeshia and Edmonds [82]. Each sub-unit grows rapidly to its maximum size, but the overall growth rate of the sheaf is slower, restricted by the incubation time between nucleation of successive sub-units. The size of each sub-unit is thought to be restricted by dislocation jamming at the interface [82]. As the sub-units can nucleate on previously formed bainite plates as well as the austenite grain boundaries, the nucleation rate of bainite is enhanced by a function of the extent of reaction $(1 + \beta\theta_{\alpha_b}\xi_{\alpha_b})$, where θ_{α_b} is the maximum bainite volume fraction as defined earlier and β is the *autocatalysis factor* [80], a function of the carbon content of the alloy:

$$\beta = \lambda_1(1 - \lambda_2 \overline{x}) \tag{4.21}$$

K_1'	K_2	λ_1	λ_2
6.78×10^{-10}	2.065×10^4	139.00	25.46

Table 4.1: Optimised values of constants in original bainite model.

and λ_1 and λ_2 are empirical constants (see Table 4.1). Thus, the autocatalytic nucleation is inhibited by the carbon build-up as the austenite enriches, and is less significant in higher carbon steels than in lower carbon steels. Autocatalysis is common in martensitic transformations where extra defects are required to explain the rapid transformation rates [83].

4.1.5 Growth Kinetics

The growth of Widmanstätten ferrite plates is controlled by carbon diffusion in the austenite ahead of the plate tip. If the extent of the carbon diffusion field ahead of the particle/matrix interface increases with particle size then the particle will grow at a parabolic rate, the growth rate decreasing with time as the distance over which the solute must diffuse increases (*e.g.* allotriomorphic ferrite). However, the diffusion controlled lengthening of plate or needle-shaped particles such as Widmanstätten ferrite can occur at a constant rate, because solute can be rejected to the sides of the particle and thus the plate tip is always growing into unenriched austenite. Trivedi [84] proposed a shape-preserving solution for the diffusion-controlled growth of plates, assuming their shape was that of a parabolic cylinder. The steady-state plate lengthening rate, V_L, at a temperature T is obtained by solving:

$$f_1 = (\pi p)^{\frac{1}{2}} \exp\{p\}\mathrm{erfc}\{p^{\frac{1}{2}}\} \left[1 + \left(\frac{r_{w_c}}{r_w}\right) f_1 S_2\{p\}\right] \tag{4.22}$$

where

$$f_1 = \frac{x_r - \overline{x}}{x_r - x^{\alpha\gamma}} \tag{4.23}$$

and the Péclet number, p, is given by:

$$p = \frac{V_L r_w}{2\overline{D}} \tag{4.24}$$

In these equations, r_w is the plate tip radius, r_{w_c} the critical radius at which growth ceases (see below), S_2 is a function of p numerically evaluated by Trivedi to correct for the change in composition with curvature along the interface, x_r is the mole fraction of carbon in austenite at the plate tip, $\overline{x}$ is the mean carbon mole fraction of the bulk austenite away from the tip and $x^{\alpha\gamma}$ is the carbon concentration of ferrite in equilibrium with austenite of composition $x^{\gamma\alpha}$. The diffusion coefficient of carbon in austenite, $D\{x,T\}$, is strongly

carbon concentration dependent, and will vary between the plate tip and the bulk austenite compositions. Thus, a weighted average diffusivity value, $\overline{D}$, is used [85]:

$$\overline{D} = \int_{x_r}^{\overline{x}} \frac{D\{x,T\}}{\overline{x} - x_r} dx \tag{4.25}$$

The model of Siller and McLellan [32], can be used to calculate $D\{x,T\}$. x_r can differ significantly from $x^{\gamma\alpha}$ due to the Gibbs-Thomson capillarity effect [37]. Capillarity allows for the change in equilibrium concentration at the interface due to the curvature of the interface – as curvature increases, x_r decreases, until at a critical plate tip radius $x_r = \overline{x}$ and plate growth ceases. For finite r_w,

$$x_r = x^{\gamma\alpha}\left[1 + \left(\frac{\Gamma}{r_w}\right)\right] \tag{4.26}$$

where Γ is the capillarity constant:

$$\Gamma = \left(\frac{\sigma_{\gamma\alpha} V_\alpha^m}{RT}\right)\left[\frac{(1 - x^{\gamma\alpha})}{(x^{\alpha\gamma} - x^{\gamma\alpha})}\right] \frac{1}{\left[1 + \frac{d(\ln a_C^\gamma)}{d(\ln x^{\gamma\alpha})}\right]} \tag{4.27}$$

Here, $\sigma_{\gamma\alpha}$ is the interfacial energy per unit area (0.2 J m^{-2}), a_C^γ is the activity of carbon in austenite and V_α^m is the molar volume of ferrite. V_L passes through a maximum as r_w increases. At small radii, the excess carbon can diffuse away from the plate rapidly, but there is also a larger surface/volume ratio which means higher energy in creating the plate surface. At larger radii, the energy will be reduced but diffusion will be less rapid. The Trivedi model provides a relationship between plate tip radius and growth velocity, but without assigning a specific velocity to an alloy composition. To fix a value for V_L, Zener's assumption that the plate will tend to adopt a tip radius such that its velocity is maximised is used. Thus, the "maximum" radius can be determined by differentiation, and V_L^{max} obtained by substitution of this value back into the equations. There is no experimental justification for this assumption, but it provides an upper bound on the growth rate.

Experimentally measured Widmanstätten ferrite growth rates have been compared with those calculated using the above theory, allowing for a stored energy of 50 J mol^{-1} [72, 75]. It was found that the measured rates were generally an order of magnitude higher than the calculated values, even when using Zener's maximum growth rate hypothesis. Applying the same theory to experimental bainite growth rates determined by a large number of researchers and incorporating a higher stored energy of 400 J mol^{-1} revealed much larger discrepancies between experiment and theory [75, 86]. It was evident that the growth of bainite sheaves always exceeded that calculated on the basis of carbon-diffusion controlled transformation. This provided further indication that the bainite transformation is diffusionless, with the excess carbon being rejected from the ferrite after the transformation is complete.

4.1.6 Overall Transformation Kinetics

4.1.6.1 Widmanstätten Ferrite

The overall kinetics of the Widmanstätten ferrite transformation can be modelled using the classical Johnson-Mehl-Avrami analysis as described in Section 3.2.1. An alternative model, targeted at weld microstructures, was created by Bhadeshia *et al.* [87]. The austenite grains were approximated as hexagonal prisms, with a layer of allotriomorphic ferrite initially formed around the boundaries. The half-thickness, q, of this layer was found by integration:

$$q = \int_{t=0}^{t_1} \frac{1}{2}\alpha_1 t^{-\frac{1}{2}}\, dt \tag{4.28}$$

where t is the time since the start of the transformation, t_1 is an incubation period after which Widmanstätten ferrite formation becomes feasible and α_1 is the rate constant for parabolic thickening of allotriomorphs under carbon diffusion-controlled growth. The resulting ferrite volume fractions were a factor of two smaller than experimental results and so a corrected half-thickness, q', was determined to allow for this.

Widmanstätten ferrite was assumed to nucleate at allotriomorphic ferrite/austenite boundaries and grow into the austenite grains as packets of thin, lath-like triangular prisms. Its formation is encouraged by large austenite grains, which reduce the likelihood of impingement of the grain boundary ferrite allotriomorphs, providing more room for the Widmanstätten ferrite to grow. The amount of γ/α boundary area per unit length of austenite grain was $3(\overline{L} - 4q'C_1)$, where C_1 is a geometrical factor. The fraction of this area which can actually nucleate was designated C_2 and was a constant for all steels. The plate volume was considered proportional to the length in the direction of growth, the other two dimensions being fixed by sideways impingement between adjacent plates within a packet. The high plate lengthening rate, as discussed in the preceding section, justifies the assumption made that Widmanstätten ferrite forms approximately isothermally, even under continuous cooling conditions, because the transformation reaches completion in a fraction of a second. The model assumed that allotriomorphic ferrite growth ceased at a temperature T_l to give way to Widmanstätten ferrite, and does not deal with the simultaneous formation of both phases, which is what happens in reality. The volume of a plate nucleated at a time τ at a later time t was:

$$v_\tau = C_3 V_L (t - \tau - t_1) \tag{4.29}$$

Assuming that there was no interference between plates growing from other areas of the γ/α boundary, then the volume fraction of Widmanstätten ferrite formed from $\tau = 0$ to

$\tau = t$ was:

$$V_w = \frac{3C_2(\overline{L} - 4q'C_1)}{(3\overline{L}^2/4C_1)} \int_{\tau=0}^{t-t_1} C_3 V_L(t - t_1 - \tau) I_{w,b}\, d\tau \tag{4.30}$$

where $I_{w,b}$ is the nucleation rate per unit area of γ/α interface, and C_3 is a constant.

4.1.6.2 Bainite

The standard Johnson-Mehl-Avrami approach to transformation kinetics has been applied to the bainite reaction with limited success, even when empirically fitting the equation to experimental results [30]. There is also the problem that the bainite reaction usually comprises the simultaneous formation of the bainitic ferrite and carbides. The two reactions have different transformation mechanisms and until recently there has been no method for modelling such behaviour. Bhadeshia [79] proposed a model for the overall transformation kinetics of upper bainite, aimed at steels where the carbide (cementite) precipitation reaction is retarded due to alloying with elements such as silicon. The model uses the universal nucleation function and displacive nucleation rate equation derived earlier in this chapter to determine the thermodynamics and kinetics of the transformation. Enrichment of austenite with carbon is permitted and the transformation is stopped at the T_o' boundary. The autocatalytic sub-unit model is utilised, each sub-unit having a fixed volume u, taken as $0.2 \times 10.0 \times 10.0\,\mu\text{m}^3$ [88]. The number of bainite sub-units nucleated per unit volume in a time dt is given by:

$$N_{\alpha_b} = (1 + \beta\theta_{\alpha_b}\xi_{\alpha_b}) I_{\alpha_b}\, dt \tag{4.31}$$

where ξ_{α_b} is the normalised volume fraction of bainite (with $\xi_{\alpha_b} = \frac{V_{\alpha_b}}{\theta_{\alpha_b}}$ where V_{α_b} is the actual volume of bainite formed) and θ_{α_b} is the maximum volume fraction of bainite that can form (equation 4.1). Converting extended volume into actual volume, the increment in bainite volume fraction between times t and $t + dt$ can be expressed as [80]:

$$d\xi_{\alpha_b} = \frac{uK_1}{\theta_{\alpha_b}}(1 - \xi_{\alpha_b})(1 + \beta\theta_{\alpha_b}\xi_{\alpha_b}) I_{\alpha_b}\, dt \tag{4.32}$$

The equation was rewritten to calculate time t as a function of the normalised volume fraction, and optimised over a set of experimental data [79] to determine the unknown constants K_1', K_2, λ_1 and λ_2 [80]. Their values are given in Table 4.1.

The predictions of the model for the evolution of bainite volume fraction with time were successfully tested against three different experimental steels – 0.22 C 2.03 Si 3.0 Mn wt.%, 0.39 C 2.05 Si 4.08 Ni wt.% and a 300M steel – isothermally transformed at a series of different temperatures [80].

4.2 The Martensite Transformation

Martensite can be a very hard phase often formed by rapid quenching of austenite to room temperature. It commonly consists of a supersaturated solid solution of carbon in ferritic iron. The ferrite forms with the same composition as the austenite by a diffusionless shear mechanism, with not even the carbon atoms able to partition. The carbon trapped in the interstices distorts the ferrite lattice, leading to strains which harden the material. Optically, martensite has a lath-like or lenticular morphology. In the low alloy steels of interest in this work, it generally forms at fast cooling rates where there is insufficient time for diffusional transformation and other displacive transformations are suppressed.

4.2.1 Thermodynamics of the Martensite Transformation

The martensite transformation during continuous cooling is athermal, depending only upon temperature rather than the time at that temperature. It starts at a well-defined M_s temperature and continues whilst temperature decreases until the martensite finish temperature, M_f. The well-known Andrews formula [89], verified by many workers over the years, can be used to calculate M_s as a function of the alloy content of the steel:

$$M_s(^\circ C) = 539 - 423\mathrm{C} - 30.4\mathrm{Mn} - 17.7\mathrm{Ni} - 12.1\mathrm{Cr} - 7.5\mathrm{Mo} \quad wt.\% \tag{4.33}$$

A less empirical approach requires the calculation of the free energy change for the formation of ferrite of the same composition as austenite, $\Delta G^{\gamma\rightarrow\alpha'}$. Hsu and Hongbing [90] determined M_s from:

$$\Delta G^{\gamma\rightarrow\alpha'} = -1394 - 5880\overline{x} + 0.42M_s \tag{4.34}$$

Bhadeshia [91] derived an expression for the driving force for the martensitic transformation based on the Lacher, Fowler and Guggenheim formalisms as applied by Aaronson *et al.* [20] with corrections by Shiflet *et al.* [92]. The M_s can then be evaluated by balancing this driving force against the available chemical free energy change accompanying the transformation at the M_s temperature, $\Delta G^{\gamma\rightarrow\alpha'}_{M_s}$, and solving for the absolute temperature, T, Figure 4.6.

4.2.2 Kinetics of the Martensite Transformation

Martensite can grow at speeds approaching the speed of sound in steels and is not strongly thermally activated [12]. Nucleation begins at M_s, and its mechanism is still the subject of much research. If the classical nucleation theory of random fluctuations is applied, the activation energy barrier for nucleation would be too large to be feasible [95]. The theory

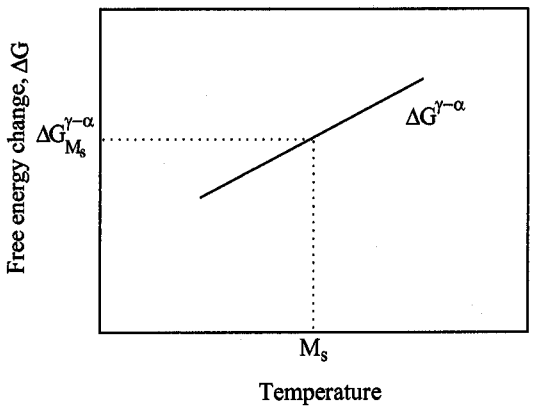

Figure 4.6: Schematic illustration of how the M_s temperature can be determined.

of pre-existing embryos discussed in Section 4.1.3.2 has been postulated instead [78], in which an array of defects already present in the lattice becomes unstable and dissociates to form regions of the new phase.

A general equation to describe the extent of the overall austenite-martensite transformation in plain carbon steels was derived by Koistinen and Marburger [96]. They measured the volume fraction of retained austenite, V_γ, in a series of steels quenched at various temperatures, T_q, below M_s and found that the results could be fitted to a straight line. The rest of the steel was considered to have transformed to martensite, volume fraction V_m. Thus:

$$V_\gamma = 1 - V_m = \exp\{-0.011(M_s - T_q)\} \tag{4.35}$$

for $M_s > T_q > -80°C$. The simple form of the equation implies that factors such as steel composition and austenite state affect the fraction of martensite only through their effect on M_s, the actual amount of martensite depending only on the degree of undercooling below M_s. Magee [83] presented a theoretical justification of this equation, in which it is assumed that the number of new martensite plates, N_m, that form per unit volume of austenite is proportional to the driving force $\Delta G^{\gamma\rightarrow\alpha'}$:

$$dN_m = -C_2\, d(\Delta G^{\gamma\rightarrow\alpha'}) \tag{4.36}$$

where C_2 is a constant. If $\overline{V}$ is the average volume of a newly formed plate, it can be shown that:

$$1 - V_m = \exp\left\{\overline{V}C_2\frac{d(\Delta G^{\gamma\rightarrow\alpha'})}{dT}(M_s - T_q)\right\} \tag{4.37}$$

assuming that the rate of change of driving force with temperature is constant. The above relationship has a similar form to equation (4.35). Khan and Bhadeshia [97] re-evaluated

the Koistinen and Marburger equation with new experimental data. They found a good fit apart from at the early stages of reaction where the data deviated from linearity. It was suggested that this was due to the neglection of autocatalysis effects by the theory, the number of pre-existing defects in austenite not being large enough to account for the very rapid transformation kinetics of martensite. The additional defects required were attributed to autocatalysis, in which the martensite plates induce new embryos into the austenite which can then also transform. On this basis, Khan and Bhadeshia derived a new relation between martensite fraction and undercooling:

$$-\frac{\ln(1-V_m)}{V_m} = 1 + C_6\overline{V}(M_s - T_q) \tag{4.38}$$

where C_6 is a constant. A slightly better correlation was found with the experimental data than when using equation (4.35).

4.3 Summary

The application of displacive transformation theory to the decomposition of austenite to Widmanstätten ferrite, bainite and martensite has been reviewed.

The criteria for nucleation of Widmanstätten ferrite and bainite are considered to be the same, and utilise a universal function to determine the driving force for a detectable degree of transformation. The energy subsequently available for growth of a nucleus determines into which phase it develops. The growth of both phases involves an IPS shape change and thus a stored strain energy. The activation energy barrier for displacive nucleation has been found to have a linear dependence on the chemical driving force, in contrast to the classical theory of nucleation. A different nucleation rate equation is therefore utilised for displacive transformations.

A theory for the carbon diffusion-controlled growth of Widmanstätten ferrite plates has been described, which enables rapid lengthening rates as carbon is rejected to the sides of the plates. The bainite transformation is considered to be diffusionless, the carbon being partitioned from the sub-units after transformation is complete. Bainite growth ceases when the T_o' composition is reached. The driving force for the diffusionless transformation is that of austenite to ferrite of the same composition.

Existing models for the overall transformation kinetics of Widmanstätten ferrite and bainite have been described. The Widmanstätten ferrite model assumes that allotriomorphic ferrite formation ceases at W_s. The bainite model includes an autocatalytic nucleation mechanism for the sub-units which make up the bainite sheaves. The extent of the martensite transformation can be simply determined from the degree of undercooling

below M_s. Therefore, there are suitable theories on which to base transformation models for the displacive phases.

Chapter 5

Existing Phase Transformation Models

The large advances in computing technology over the past 20 years have had a significant impact on modelling work, enabling rapid solution of iterative equations and making possible the development of powerful models. Many researchers have created models based on the fundamental physical and metallurgical principles of phase transformations, utilising some of the thermodynamic and kinetic theories described in preceding chapters, with the aim of developing a generally applicable model for a wide range of steels. Some of these models are so-called "complete" models, often encompassing the thermomechanical processing and recrystallisation of austenite prior to cooling, as well as the transformation products – allotriomorphic ferrite, pearlite, Widmanstätten ferrite, bainite and martensite. Such models can form a basis for property prediction such as Jominy hardenability [99] or yield strength. Other workers have concentrated on detailed analyses of transformation to particular phases, such as allotriomorphic ferrite [69, 98] or pearlite [99], or have produced models to predict time-temperature-transformation (TTT) diagrams [2, 25, 100, 102]. As this thesis is concerned primarily with the computation of the whole microstructure after hot-rolling of austenite, an overview of some of the "complete" physical models in the literature is provided in this chapter.

5.1 "Complete Models"

Several researchers, notably in Japan, have developed models encompassing all the possible phase transformations from austenite during cooling, often coupled with models for thermomechanical processing in the austenite field. The structure of these models typically

follows that outlined in Figure 1.4. Many of the models are concerned with transformation during isothermal holding at temperatures below the Ae_3 temperature, as well as continuous cooling and some have been extended to predict mechanical properties, such as hardness and tensile strength.

Umemoto *et al.* [70] developed a methodology to simulate the phase transformations from work-hardened austenite, considering both continuous cooling and isothermal transformation. The Scheil analysis was used to approximate continuous cooling as the sum of short isothermal holding times at successive temperatures, and the extended and overall volume fraction of each phase was computed at every temperature, using Cahn's theory of boundary nucleation kinetics [46]. Models for allotriomorphic ferrite, Widmanstätten ferrite, pearlite, bainite and martensite were incorporated. The Hillert-Staffanson regular solution model was used to calculate the thermodynamics for 10 elements under paraequilibrium conditions. Classical nucleation theory was applied for allotriomorphic ferrite and pearlite, followed by parabolic and linear growth, respectively. The displacive nucleation thermodynamic criteria used to determine the start of Widmanstätten ferrite and bainite transformation were slightly different from those of Bhadeshia in Chapter 4, based on different thermodynamic data. The universal nucleation function was evaluated as:

$$G_N = 4204 - 5.96(T - 273) \quad \text{J mol}^{-1} \tag{5.1}$$

and the stored energies for growth of Widmanstätten ferrite and bainite were 300 and 600 J mol^{-1}, respectively. Growth kinetics were derived from Trivedi's solution for diffusion-controlled growth of plates [84]. Martensite transformation followed Koistinen and Marburger's equation [96]. The program was designed primarily for thermomechanically processed high strength, low alloy steels and allowed for the effect of the deformation on austenite transformation kinetics and ferrite nucleation sites. The free energy of the work-hardened austenite was evaluated by adding the strain energy associated with the dislocations to the energy of the undeformed austenite. The strain energy per unit volume was:

$$W = V_\gamma^m \rho \frac{\mu b^2}{4\pi K} \ln \frac{R_d}{b} \tag{5.2}$$

where V_γ^m is the molar volume of austenite, ρ the dislocation density, μ the shear modulus, b the magnitude of the Burgers vector of the dislocation, R_d the dislocation spacing and K a constant.

Saito and Shiga [104] similarly produced a simulation for microstructural evolution during thermomechanical processing of Nb-containing HSLA plates. They considered the evolution of the austenite grain structure during deformation and recrystallisation, austenite grain boundary precipitation and dissolution of carbonitrides (using a classical nucleation model), followed by transformation to allotriomorphic ferrite, pearlite and

bainite. The quasichemical model was used to evaluate the thermodynamics under paraequilibrium conditions. Parabolic growth of allotriomorphic ferrite and volume diffusion-controlled pearlite growth kinetics were applied. Bainite transformation initiated once the 400 J mol^{-1} stored energy for growth was exceeded, but the rest of the bainite model just used similar equations to those for pearlite. Overall transformation kinetics were modelled with the Johnson-Mehl-Avrami (JMA) theory. The program can predict continuous cooling transformation (CCT) diagrams and ferrite grain size.

The model of Anelli and co-workers [57] allows a stepped cooling/holding profile to be considered as well as linear cooling. It predicts the phase transformations of thermomechanically processed steels from the austenite region, focussing on accelerated cooling schedules in a plate mill and low C-Mn or Nb microalloyed steels. The elements considered were C, Si, Mn, Ni, Mo and Nb. The effect of austenite deformation was considered as an increase in the dislocation density per unit area, ρ, and thus strain energy per unit volume, W, where $W = -\tau_d \rho$ and τ_d is the energy per unit length of the dislocation line. Both dynamic and static recovery were allowed for in a limited way, but not recrystallisation. The cooling schedule was divided into small time increments and the volume fractions of all five phases were determined as a function of time and temperature in each interval using standard transformation kinetics theory. Classical nucleation theory with a coherent "pill-box" shaped nucleus was applied for allotriomorphic ferrite transformation. A statistical distribution model due to Abbruzzese [55] was invoked to follow the nucleation and growth of ferrite nuclei, thus a ferrite grain size distribution could be obtained throughout the transformation. Pearlite transformation started when the enriched austenite composition exceeded the austenite/cementite phase boundary, and growth proceeded under boundary diffusion control. Widmanstätten ferrite and bainite formed when the appropriate displacive nucleation criteria were satisfied (as in Umemoto's model) and grew according to Trivedi's solution for diffusion controlled growth of plates. Widmanstätten ferrite was nucleated according to classical heterogeneous kinetic theory whereas bainite was assumed to nucleate homogeneously within the austenite grains. Koistinen and Marburger's equation was again applied for martensite transformation. The model was successfully validated with both laboratory and industrial data.

Lee and co-workers [105] developed a mathematical model for transformation in Nb microalloyed steels, considering Fe, C, Mn and Nb. They used the Hillert-Staffanson two sub-lattice model [106] to determine phase boundaries and free energies under local and paraequilibrium conditions. Stored energies of 300 and 600 J mol^{-1} determined by Nanba *et al.* [107] were used to determine W_s and B_s, respectively. Classical nucleation theory was applied for ferrite and a coherent pillbox nucleus was assumed for ferrite, pearlite and

bainite. Precipitation of spherical NbC nuclei was also included. The austenite grains were taken to be spheres and grain edge nucleation was assumed to dominate. The overall transformation kinetics were calculated using the JMA theory. Allotriomorphic ferrite ellipsoids of aspect ratio 3:1 grew at a parabolic rate controlled by bulk diffusion of carbon in austenite. Under local equilibrium, Mn boundary diffusion was rate controlling during nucleation, whereas under paraequilibrium bulk carbon diffusion was preferred. Widmanstätten ferrite and bainite formed as ellipsoids with an aspect ratio of 10:1, under carbon boundary diffusion control during both nucleation and growth. The bainite thickening kinetics were taken to be 5 times faster than those of Widmanstätten ferrite. Pearlite was assumed to form under paraequilibrium, with carbon boundary diffusion control during nucleation and bulk carbon diffusion control during growth. Calculated TTT and CCT curves were compared successfully with dilatometric results for C-Mn and C-Mn-Nb steels.

Suehiro *et al.* [108] produced a model for hot rolling of low carbon Si-Mn steels, the effects of composition on the thermodynamic parameters being included by the methods of Uhrenius. Classical nucleation was assumed for allotriomorphic ferrite with the Zener-Hillert theory used for ferrite and bainite growth. Pearlite growth was volume diffusion controlled. The transformation was divided into two stages, in which different overall transformation kinetics equations applied. In the early stages, a nucleation and growth model was used, whilst at later stages site saturation was assumed. The model still relied on an experimentally determined B_s temperature and required empirical parameters in the kinetic equations, and thus is restricted to the low carbon steels for which it was designed. It was linked with models for hot deformation and strength prediction.

Denis *et al.* modelled transformations during cooling to allotriomorphic ferrite, pearlite, bainite and martensite [109]. Overall kinetics for the first three phases were based on the JMA theory, with the Koistinen and Marburger relation used for martensite. Phase boundary compositions were determined from the equilibrium phase diagram and the Hultgren extrapolation. Scheil's analysis was used to convert a series of small isothermal time steps into continuous cooling. A correction was made to account for non-additivity at the transition from pearlite to bainite transformation. The model was coupled with a similar one for transformation to austenite during heating.

5.2 Limitations of Existing Models

The "complete" models discussed calculate the transformation of austenite to at least allotriomorphic ferrite, pearlite and bainite. Their thermodynamics are based on variants

of the regular solution model. Several models considered some of the effects of deformed austenite on the driving force for subsequent transformation. Paraequilibrium was the chosen growth mode in all cases. Allotriomorphic ferrite was modelled using classical nucleation theory and parabolic, carbon diffusion-controlled growth. Pearlite growth was generally considered to be carbon volume diffusion-controlled. The universal nucleation function and displacive nucleation criteria were used to determine W_s and B_s, although the values of the stored energies and the approach for the subsequent growth kinetics of bainite varied between models. The JMA overall transformation kinetics theory was consistently adopted for all phases except martensite, where Koistinen and Marburger's theory was preferred.

A complete metallurgical model for transformation after hot rolling must consider all the phases that can form, which is not the case in several of the models described. A large number of different alloying elements are used in modern steels, so as many of these as possible should be included in the thermodynamic parameters of a model to enable application to a wide range of steels. Many existing programs focus only on certain elements such as C, Mn, Si and Nb, thus restricting their usage. The multiple effects of the austenite deformation on subsequent transformation must also be fully considered, as the driving forces for growth and nucleation, and the number of nucleation sites are all affected. Empirical equations, particularly for transformation-start temperatures, are still often used, but these could be replaced by considering the fundamental theory of the transformation. Ideally, the number of empirical parameters should be minimised to make the model generally applicable.

A key issue in all of these models is deciding when transformation of one phase stops and another begins. This is usually considered to occur at the transformation-start temperature of the new phase, as the overall transformation kinetics theory is only valid for formation of one phase at a time. The transformations are thus forced to occur sequentially, whereas in reality simultaneous transformation is possible and has been observed. Even if the thermodynamic criteria for the formation of a new phase are satisfied this does not necessarily require that the previous phase immediately ceases growing. Consideration of how to solve this problem was a major component of the new transformation model developed in this research.

Chapter 6

The Transformation Model

The overall aim of this research was to produce a computer-based model of the phase transformations which occur in low alloy steels on cooling from the austenite phase field, and thus to predict the final room temperature microstructure of the steel. Ideally, the model should contain as few empirical parameters as possible, instead using fundamental metallurgical theory so as to be applicable to a wide range of steel compositions. The starting point was a series of existing theories and models for different phases, which were to be extended, combined and validated to produce a coherent transformation model. The approach for each phase is described in turn in this chapter. Validation of the individual and combined models is discussed in a later chapter.

6.1 Allotriomorphic Ferrite

The foundation of the work was a calculation of the allotriomorphic ferrite transformation at a constant cooling rate from austenite of specified composition and grain structure [69]. Allotriomorphic ferrite will be the first phase to form on cooling below the Ae_3 temperature, and thus it is expected to significantly affect subsequent transformations to other phases. It is also the dominant phase in the low carbon, low alloy steels with which this work is particularly concerned.

The effects of 11 elements are included – C, Si, Mn, Ni, Mo, Cr, V, Co, Cu, Al and W, for the purpose of (a) calculating the austenite/ferrite paraequilibrium phase diagram, (b) the associated free energy changes for both reconstructive and diffusionless transformations and (c) the effect of substitutional solutes on the diffusivity of carbon in austenite. The basic method is according to Zener and has been described in Section 3.1.1.

The austenite grains were assumed to be equiaxed and of uniform size, defined by the

grain size, d_γ, which is a mean lineal intercept measured at random on random planes of section. The necessary thermodynamic and kinetic parameters were calculated at fixed temperature steps below the Ae_3' (the paraequilibrium Ae_3 temperature) until transformation was completed or stopped. A flowchart of the model is provided in Figure 6.1, outlining the main operations.

The thermodynamic quantities, such as the driving force for transformation and the paraequilibrium phase boundaries, were evaluated using the quasichemical theory as presented by Aaronson, Domian and Pound [20, 24] and Shiflet, Bradley and Aaronson [92], allowing for the effect of the alloying elements *via* the free energy terms according to Zener [23]. The driving force for formation of a ferrite nucleus was determined by the parallel tangent construction described in Section 3.1.1.1, the optimum ferrite nucleus composition being assumed to occur at the maximum free energy change. The paraequilibrium mode means that only the diffusion of carbon has to be considered as the substitutional elements do not partition; they simply affect the relative stabilities of the phases concerned. The carbon diffusivity in austenite was evaluated by the method of Siller and McLellan [32], which considers nearest neighbour interactions and the concentration dependence of the diffusivity. Parabolic growth of ferrite allotriomorphs was assumed, and the rate constant for one-dimensional thickening, α_1, was found by numerical solution of equation 3.21.

Classical nucleation theory as described in Section 3.1.4 was used to describe the heterogeneous nucleation rate on the austenite grain boundaries, $I_{\alpha,b}$. Separate equations for nucleation on each of the three types of grain boundary site were used, with different values inserted for the site density and interfacial energy shape factors at face, edge and corner sites. The volume fraction of allotriomorphic ferrite formed at each temperature was determined with the Johnson-Mehl-Avrami theory for overall heterogeneous transformation kinetics (Section 3.2.2.2). The extent of isothermal reaction ξ_α at a time t is given by:

$$\xi_\alpha = 1 - \exp\left\{-S_v\alpha_1 t^{\frac{1}{2}}\left[\int_0^1 1 - \exp\left\{-\frac{\pi}{2}I_{\alpha,b}\eta_\alpha^2\alpha_1^2 t^2(1-\phi^4)\right\}\,d\phi\right]\right\} \qquad (6.1)$$

where η_α is the aspect ratio of the disc-shaped allotriomorphs, taken as 3 [35, 36], $\phi = \frac{y}{\alpha_1 t^{\frac{1}{2}}}$ and y is the distance to an arbitrary plane parallel to the boundary with which intersection of the discs is considered. ξ_α is normalised with respect to the equilibrium volume of allotriomorphic ferrite $V\Omega_\alpha$, where V is the total volume and Ω_α the equilibrium ferrite fraction determined by the lever rule from the phase diagram (equation 3.1).

Hard impingement due to overlap of particles growing along the grain boundary and from adjacent boundaries is accounted for in this theory. However, soft impingement due to the partitioning of carbon is only approximated by assuming that the carbon is always uniformly distributed in the untransformed austenite. The mean carbon content of the

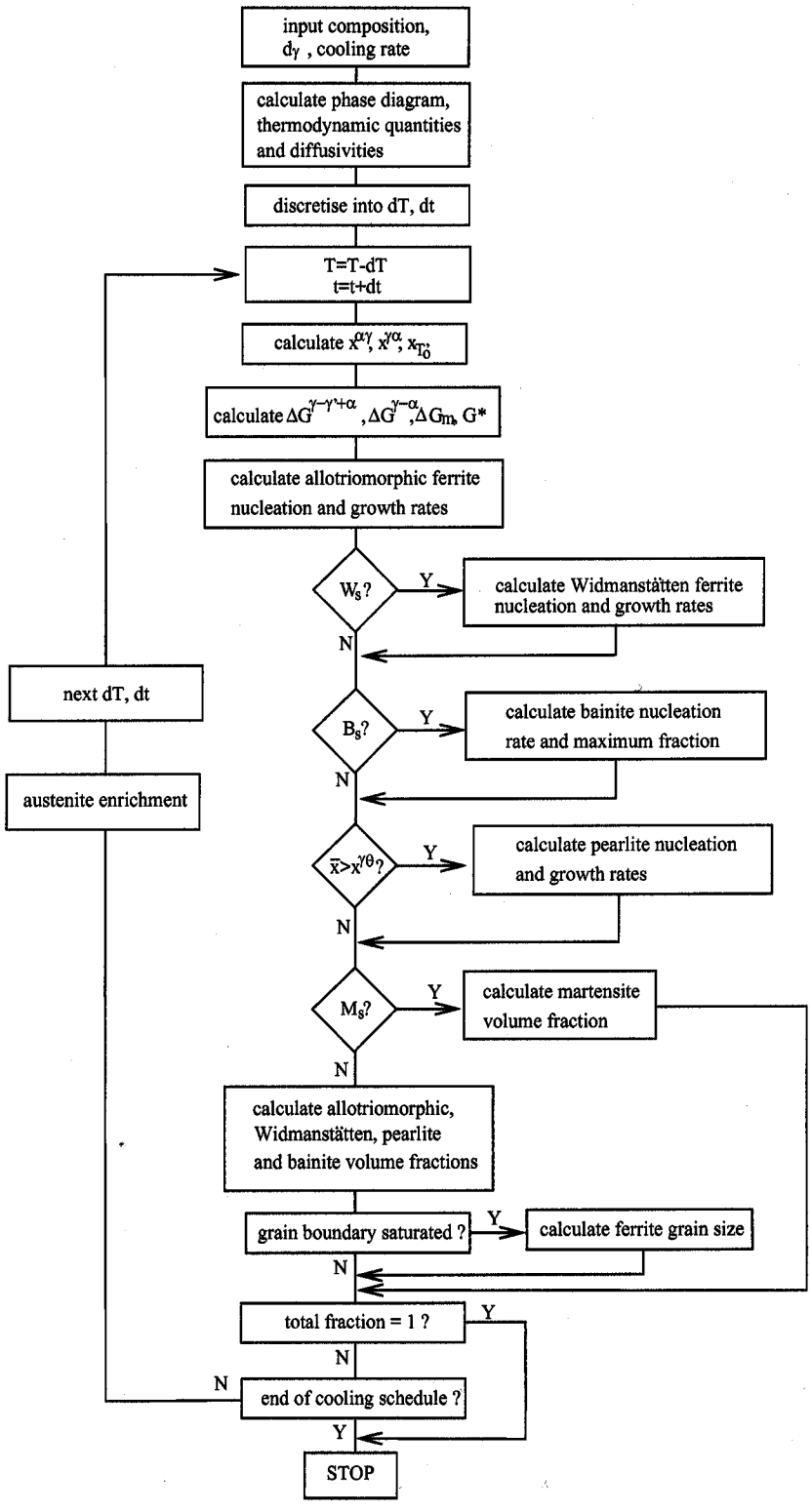

Figure 6.1: Flowchart outlining the operation of the new transformation model.

enriched austenite, $\overline{x}'$, at each temperature is given by a mass balance equation:

$$\overline{x}' = \frac{\overline{x} - x^{\alpha\gamma} V_\alpha}{1 - V_\alpha} \tag{6.2}$$

where V_α is the volume of ferrite formed, $x^{\alpha\gamma}$ is the carbon content of the ferrite and $\overline{x}$ is the mean carbon content of the alloy as a whole. In reality the carbon distribution in the austenite would obviously not be uniform but the problem cannot be rigorously treated unless the microstructure is determined from $t = 0$, with the location of every particle fixed in space. Once the boundary is saturated (*e.g.* after 90% of the boundary area is decorated with ferrite) then the number density of ferrite grains ceases to change. This limiting number density can then be used to estimate the mean ferrite grain size (equation 3.41) if it is assumed that each grain occupies an equal volume.

In the initial model, the total volume of ferrite present at each temperature step during continuous cooling at a constant rate was determined using the additivity principle [113]. The cooling curve was divided into a series of small, equal, isothermal time steps, dt. The transformed volume V_2 at a particular temperature, T_2, was determined by calculation of the volume that would have formed if all the transformation had actually occurred by isothermal holding at T_2. The holding time, t_2, is the equivalent amount of time that must be spent at T_2 to transform the total volume present at the previous temperature plus the small time step, dt. Thus, the volume of allotriomorphic ferrite predicted by the model was dependent on the accuracy of the Scheil approximation as well as the underlying theory of transformation kinetics. The work described in Chapter 7 avoids this approximation by numerically calculating only the increment in extended and real volume at each step.

6.2 Widmanstätten Ferrite

The formation of Widmanstätten ferrite from austenite was modelled using the theory introduced in Chapter 4. The Widmanstätten ferrite start temperature, W_s, was determined from the driving force for the transformation, allowing for the 50 J mol^{-1} stored energy for growth, and the universal nucleation function, G_N, using the criteria embodied in equations 4.3 and 4.4. Below this temperature, displacive nucleation of Widmanstätten ferrite plates can occur at a rate described by equation 4.17. Subsequent growth into the austenite grains was modelled with Trivedi's theory for diffusion-controlled growth of parabolic cylinders assuming that the plates grow with a tip radius which maximises the lengthening rate [84].

The original model due to Bhadeshia, Svensson and Gretoft [87] was specifically for weld deposits where the austenite grains are columnar in shape. It also did not deal properly with the initiation of the Widmanstätten ferrite transformation, which was considered

to occur when the "C"-curves on the TTT diagram for the reconstructive and displacive transformations intersected. The present treatment avoids many of these difficulties. Consider a Widmanstätten ferrite plate, nucleated on an austenite boundary at a time τ and growing at a constant rate G_w. At a later time, t, the height of the plate above the boundary will be $q_w = G_w(t-\tau)$ and its width $r_w = \eta_w q_w$ where η_w is the plate aspect ratio, taken as 0.05. The area of intersection of the plate with a plane parallel to the boundary is then $A_w = \eta_w G_w^2 (t-\tau)^2$. Following the heterogeneous nucleation theory described in Section 3.2.2.2, the change in extended area on one plane due to plates emanating from one boundary in the time interval from τ to $\tau + d\tau$ is:

$$dO^e_{\alpha_w} = \eta_w O_b I_{w,b} G_w^2 (t-\tau)^2 \, d\tau \tag{6.3}$$

where O_b is the total boundary area and $I_{w,b}$ is the Widmanstätten ferrite nucleation rate per unit area of grain boundary. Noting that only particles for which $q_w > y$ can contribute to the area and hence $\tau < t - \frac{y}{G_w}$, integrating over all times from $\tau = 0$ to $\tau = t - \frac{y}{G_w}$ and substituting $\phi_w = \frac{y}{G_w t}$, where y is the perpendicular distance of the plane from the boundary, we obtain the total extended area of α_w on one plane:

$$O^e_{\alpha_w} = \frac{1}{3} \eta_w O_b I_{w,b} G_w^2 t^3 (1-\phi_w^3) \tag{6.4}$$

Proceeeding as for allotriomorphic ferrite and integrating over all planes y from zero to infinity, the extent of the Widmanstätten ferrite reaction, ξ_{α_w}, is found to be:

$$\xi_{\alpha_w} = 1 - \exp\left\{-S_v G_w t \left[\int_0^1 1 - \exp\left\{-\frac{1}{3}\eta_w O_b I_{w,b} G_w^2 t^3 (1-\phi_w^3)\right\} d\phi_w\right]\right\} \tag{6.5}$$

Widmanstätten ferrite can form competitively with allotriomorphic ferrite and its kinetics are strongly influenced by the amount of prior allotriomorphic ferrite transformed. The carbon partitioned during allotriomorphic ferrite formation affects the growth and nucleation rates of Widmanstätten ferrite. Hence, the models for the two phases were tested together.

6.3 Pearlite

In the model, pearlite was allowed to form once the carbon content of the enriched austenite fell within the area of the phase diagram defined by the Hultgren extrapolation of the austenite/cementite and austenite/ferrite phase boundaries, Figure 6.2. The compositions $x^{\gamma\theta}$, the carbon content of the austenite in equilibrium with cementite, and $x^{\gamma\alpha}$, the carbon content of austenite in equilibrium with ferrite, on the diagram define the limits of this region at the temperature T. The phase boundaries and growth kinetics were

determined using an existing model due to Takahashi and Bhadeshia [64]. The interface compositions were calculated assuming local equilibrium using a dilute solution method due to Kirkaldy and co-workers, based on the equality of the chemical potentials of Fe, C and a substitutional element X in ferrite, austenite and M_3C carbides [1, 118].

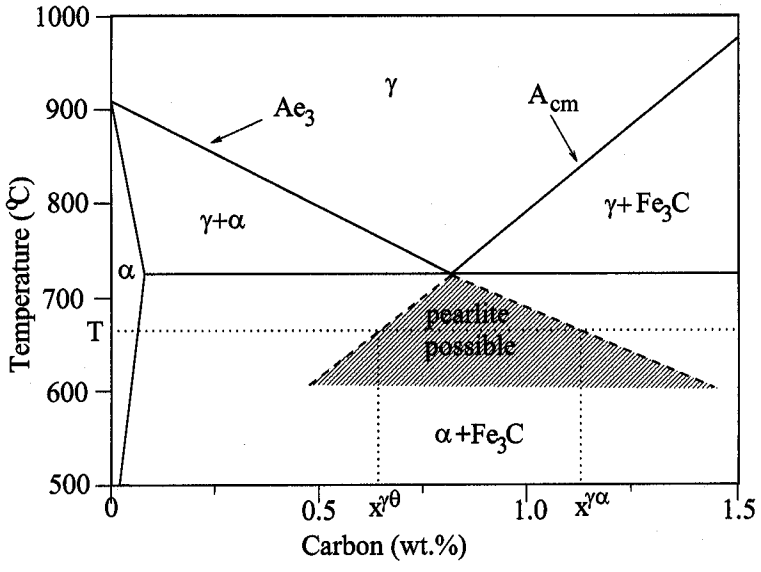

Figure 6.2: Hultgren extrapolation of the austenite/cementite and austenite/ferrite phase boundaries in the Fe-C phase diagram, indicating the region where pearlite formation is possible (after [63]).

Pearlite does not form under paraequilibrium conditions, unlike ferrite, and so diffusion of the substitutional elements must be considered. The model can allow for the diffusion of a single substitutional element. The equation for the boundary diffusion-controlled growth rate, as explained in Section 3.3.2, is given by:

$$G_p^b = 12KD_X^b\delta\left[\frac{S^2(x_X^{\gamma\alpha} - x_X^{\gamma\theta})}{S_\alpha S_\theta \overline{x}_X}\frac{1}{S^2}\left(1 - \frac{S_c}{S}\right)\right] \tag{6.6}$$

The factor $KD_X^b\delta$ was derived by expressing it in the form [119]:

$$KD_X^b\delta = C_K\{X\}\exp\left\{-\frac{Q_K\{X\}}{RT}\right\} \tag{6.7}$$

where $C_K\{X\}$ and $Q_K\{X\}$ are empirically determined constants for each alloying element X. The interlamellar spacing S and critical interlamellar spacing for zero growth rate S_c were estimated empirically [64] and it was assumed that S adopts a value consistent with the maximum growth rate such that $S = 2S_c$ with $S_c = \frac{2\sigma_{\alpha\theta}T_e}{\Delta H \Delta T}$. $\sigma_{\alpha\theta}$ is the ferrite/cementite interfacial energy, ΔH is the change in enthalpy between parent and product phases

and ΔT is the undercooling below the eutectoid temperature, T_e. The ratio between the ferrite and cementite lamella spacings, S_α and S_θ, was assumed to be 7. Figure 6.3 illustrates these lamellae within a pearlite colony. Takahashi found good agreement between calculated and experimental lamellar spacings and growth rates [64].

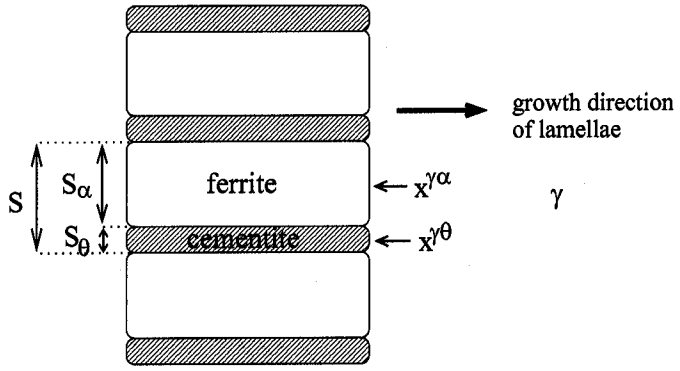

Figure 6.3: Illustration of a pearlite colony, showing the interlamellar spacings and compositions used in the growth model.

The nucleation rate of the pearlite was treated classically, using the same equations as for allotriomorphic ferrite, and considering face, edge and corner nucleation sites with the same values of site density and shape factors. The overall transformation kinetics of pearlite were again described by the JMA theory, adapted for hemispherical particles of radius r_p nucleating at the grain boundaries at a rate $I_{p,b}$ and growing with a constant rate G_p. The equations are the same as for spherical particles (Section 3.2.2.2), apart from the factor of two which accounts for the growth of spheres on both sides of the grain boundary. Both spheres and hemispheres intersect a plane at y parallel to the boundary in a disc of area $A_p = \pi[G_p^2(t-\tau)^2 - y^2]$. The change in extended area on one plane due to hemispheres emanating from one boundary in the time interval from τ to $\tau + d\tau$ is then:

$$dO_p^e = \pi O_b I_{p,b}[G_p^2(t-\tau)^2 - y^2]\, d\tau \tag{6.8}$$

where O_b is the total boundary area and $I_{p,b}$ is the pearlite nucleation rate per unit boundary area. Integrating over all times from $\tau = 0$ to $\tau = t - \frac{y}{G_p}$ and substituting $\phi_p = \frac{y}{G_p t}$, we obtain the total extended area of pearlite on one plane:

$$O_p^e = \frac{\pi}{3} O_b I_{p,b} G_p^2 t^3 (1 - 3\phi_p^2 - 2\phi_p^3) \tag{6.9}$$

Proceeding as before and integrating over all planes y from zero to infinity, we find that the extent of reaction is:

$$\xi_p = 1 - \exp\left\{-S_v G_p t \left[\int_0^1 1 - \exp\left\{-\frac{\pi}{3} O_b I_{p,b} G_p^2 t^3 (1 - 3\phi_p^2 - 2\phi_p^3)\right\} d\phi_p\right]\right\} \tag{6.10}$$

In the steels of interest in this work, pearlite usually grows from the enriched austenite after allotriomorphic ferrite and Widmanstätten ferrite have formed. Thus, the pearlite model needed to be validated in conjunction with the other two phases.

6.4 Bainite

The model for the decomposition of austenite to bainite was based on that of Bhadeshia [79] as modified by Rees [80] and described in Chapter 4. The bainite-start temperature, B_s, was determined from the driving force for the transformation, allowing for the 400 J mol^{-1} stored energy, and the universal nucleation function, G_N, as per the criteria in equations 4.3 and 4.5. Below this temperature, bainite sub-units can nucleate at a rate per unit volume of:

$$I_{\alpha_b} = K_1 \exp\left\{-\frac{K_2}{RT}\left(1+\frac{\Delta G_m}{K_4}\right)\right\} \tag{6.11}$$

This is the same nucleation rate as for Widmanstätten ferrite, but for bainite it was enhanced by the factor $(1+\beta\theta_{\alpha_b}\xi_{\alpha_b})$ to accommodate autocatalytic nucleation of sub-units. In this original model, the sub-units were considered to be effectively nucleating randomly, rather than heterogeneously on the austenite grain boundaries. The driving force ΔG_m was recomputed at each stage of the transformation to incorporate the effects of carbon enrichment of the austenite. Bainite grows at a rate much faster than expected from carbon diffusion-controlled lengthening [86]. Furthermore, the lengthening of each sub-unit is arrested by the breakdown of coherency as the shape deformation causes plastic strain in the adjacent austenite. Thus, the growth of a sheaf can be considered to occur at a rate controlled by the nucleation of sub-units, each of which grows very rapidly to transform a fixed volume of austenite, u [88]. The model therefore does not require a bainite growth rate. Further refinement of the model led to the incorporation of a temperature dependent bainite sub-unit width, based on the experimental measurements of Chang on steels containing between 0.095–0.5 wt.% C isothermally transformed between 250 and 500 °C [121]. The sub-unit volume then became:

$$u' = u \times \frac{(T-528)}{150} \tag{6.12}$$

A lower limit of $u' = 0.3u$ was fixed at 300 °C to ensure realistic sub-unit sizes below this temperature. The overall transformation kinetics were derived from Rees and Bhadeshia's model. The increment in the normalised bainite volume fraction between times t and $t+dt$ in the present work was expressed as:

$$d\xi_{\alpha_b} = \frac{u'K_1}{\theta_{\alpha_b}}(1-\xi_{\alpha_b})I_{\alpha_b}(1+\beta\theta_{\alpha_b}\xi_{\alpha_b})\,dt \tag{6.13}$$

where θ_{α_b} is the maximum bainite fraction determined from the phase diagram. The T'_o line was calculated within the model and bainite transformation was halted when the austenite carbon content reached this composition.

6.5 Martensite

The martensite transformation was modelled very simply, using the well-established theory of Koistinen and Marburger [96] to compute the volume fraction as a function of undercooling below the M_s. The start temperature was determined by solution of the equation for the driving force for the $\gamma \rightarrow \alpha'$ transformation [93]. Once the martensite transformation was initiated transformation to all other phases ceased. This is a reasonable approximation given the rapid rate at which martensite forms.

6.6 Combination of Phase Models

In the early work [87], transformations were modelled unrealistically as occurring in sequence with only one phase forming at any given time. The allotriomorphic ferrite calculations were started once the two-phase $\alpha + \gamma$ field was entered at the Ae'_3 temperature; for pearlite, when $\overline{x}' \geq x^{\gamma\theta}$, whilst Widmanstätten ferrite, bainite and martensite were initiated below the calculated W_s, B_s and M_s temperatures, respectively. As emphasised earlier, these were treated as sequential transformations occurring in isolation. For example, allotriomorphic ferrite nucleation and growth ceased once W_s was reached. In reality, allotriomorphic ferrite formation can often continue below W_s, and the transformations are simultaneous rather than sequential. In the next chapter, recent theory which enables this competitive formation of the phases to be more accurately modelled is described.

Chapter 7

Simultaneous Transformation Kinetics

In many situations, phase transformations do not occur singly, or one at a time in sequence. The decomposition of austenite in steels can involve the competitive formation of at least five different phases. For example, overlapping ferrite and pearlite reactions have been observed by differential scanning calorimetry and verified by metallography [122]. Standard Avrami theory as described in Chapter 3 can be invoked to model each phase in turn, the "switching over" from the calculation of one phase to another occurring at predefined points (temperatures, compositions). However, if the complete decomposition of austenite is to be comprehensively and successfully modelled then it would be desirable to allow *simultaneous, competitive* reactions to occur. A recent adaptation of the JMA theory [123, 124] enables us to do precisely this.

7.1 Basic Theory

Consider first the decomposition of a parent phase γ to two phases α and β, with nucleation and growth rates I_α, I_β and G_α, G_β respectively. Assuming spherical particles and constant nucleation and growth rates with the particles forming at random locations as before, it follows from equation 3.47 that the change in extended volume of α between τ and $\tau + d\tau$ is given by:

$$dV_\alpha^e = \frac{4\pi}{3} G_\alpha^3 (t-\tau)^3 I_\alpha V \, d\tau \tag{7.1}$$

where V is the total volume of the system. By analogy, the change in extended volume of β over the same time interval is:

$$dV_\beta^e = \frac{4\pi}{3} G_\beta^3 (t-\tau)^3 I_\beta V \, d\tau \tag{7.2}$$

To convert the extended volumes into actual volumes, we once again allow for the probability that some transformation has occurred in previously transformed material. Thus the actual change in volume of each phase due to particles nucleated in the interval τ to $\tau+d\tau$ is:

$$dV_\alpha = \frac{4\pi}{3} G_\alpha^3 (t-\tau)^3 I_\alpha V \left(1 - \frac{V_\alpha}{V} - \frac{V_\beta}{V}\right) d\tau \tag{7.3}$$

$$dV_\beta = \frac{4\pi}{3} G_\beta^3 (t-\tau)^3 I_\beta V \left(1 - \frac{V_\alpha}{V} - \frac{V_\beta}{V}\right) d\tau \tag{7.4}$$

Therefore,

$$dV_\alpha = \left(1 - \frac{V_\alpha}{V} - \frac{V_\beta}{V}\right) dV_\alpha^e \tag{7.5}$$

$$dV_\beta = \left(1 - \frac{V_\alpha}{V} - \frac{V_\beta}{V}\right) dV_\beta^e \tag{7.6}$$

Comparing with equation 3.49, we can see that unlike the case for one phase, these equations cannot in general be integrated directly to obtain the total volume and extent of reaction for each phase. This is because V_α and V_β are unspecified functions of one another and thus the variables cannot be separated. Therefore, the integration over all incubation times τ has to be performed numerically. The values of dV_α and dV_β are evaluated using a pair of nested loops, the inner loop allowing increments in the incubation time, τ, the outer one changes in transformation time, t. V_α and V_β are initially set to zero and are then updated at the end of each outer loop. The change in the extended volume of α (and likewise β) in the i-th time interval after the start of the transformation is calculated in two stages. Firstly, consider the change in volume due to new particles nucleated in the current time interval, Δt:

$$dV_{\alpha,i}^e = \frac{4\pi}{3} G_\alpha^3 (\Delta t)^3 I_\alpha V \, d\tau \tag{7.7}$$

Then, consider the change in volume contributed by the growth in the current time interval of particles nucleated in all previous time intervals, $j = 1$ to $j = i-1$. The rate of change of volume of a spherical particle of volume $v_\alpha = \frac{4\pi}{3} G_\alpha^3 (t-\tau)^3$ is:

$$\frac{dv_\alpha}{dt} = 4\pi G_\alpha^3 (t-\tau)^2 \tag{7.8}$$

For an infinitessimally small time interval, dt, $dv_\alpha = 4\pi G_\alpha^3 (t-\tau)^2 \, dt$. However, in a finite time interval, Δt, we must integrate to find the small change in volume Δv_α. In the time interval from $t = 0$ to $t = \Delta t$, for an incubation time τ:

$$\begin{aligned}
\int_0^{\Delta v_{\alpha,1}} dv_\alpha &= \int_0^{\Delta t} 4\pi G_\alpha^3 (t-\tau)^2 \, dt \\
\Delta v_{\alpha,1} &= \left[\frac{4\pi}{3} G_\alpha^3 (t-\tau)^3\right]_0^{\Delta t} \\
&= \frac{4\pi}{3} G_\alpha^3 \left[(\Delta t - \tau)^3 + \tau^3\right] \\
&= \frac{4\pi}{3} G_\alpha^3 \left[(\Delta t)^3 - 3\Delta t \tau (\Delta t - \tau)\right]
\end{aligned} \tag{7.9}$$

In the time interval from $(i-1)\Delta t$ to $i\Delta t$, for an incubation time $j\Delta\tau$,

$$\begin{aligned}
\Delta v_{\alpha,i} &= \int_{(i-1)\Delta t}^{i\Delta t} 4\pi G_\alpha^3 (t - j\Delta\tau)^2 \, dt \\
&= \left[\frac{4\pi}{3} G_\alpha^3 (t - j\Delta\tau)^3\right]_{(i-1)\Delta t}^{i\Delta t} \\
&= \frac{4\pi}{3} G_\alpha^3 \left[(i\Delta t - j\Delta\tau)^3 - ((i-1)\Delta t - j\Delta\tau)^3\right] \\
\Rightarrow \Delta v_{\alpha,i} &= \frac{4\pi}{3} G_\alpha^3 \left[(\Delta t)^3(3i^2 - 3i + 1) - 3(\Delta t)^2 j\Delta\tau(2i-1) + 3\Delta t(j\Delta\tau)^2\right] \quad (7.10)
\end{aligned}$$

This reduces to equation 7.9 when $i = 1$. For $\Delta t = \Delta\tau$, we get:

$$\Delta v_{\alpha,i} = \frac{4\pi}{3} G_\alpha^3 (\Delta t)^3 [1 + 3(i-j)(i-j-1)] \quad (7.11)$$

Thus, the change in extended volume of α between $t = (i-1)\Delta t$ and $t = i\Delta t$ due to the growth of previously nucleated particles at a constant time step is:

$$\begin{aligned}
dV_{\alpha,i}^e &= I_\alpha V \, \Delta\tau \sum_{j=0}^{i-1} \Delta v_{\alpha,i} \\
&= \frac{4\pi}{3} G_\alpha^3 I_\alpha V (\Delta t)^4 \sum_{j=0}^{i-1} [1 + 3(i-j)(i-j-1)] \quad (7.12)
\end{aligned}$$

The change in actual volume of α, $dV_{\alpha,i}$ is calculated at the end of each time interval, when the total change in extended volume due to nucleation of new particles and growth of existing ones in that time interval is multiplied by $\left(1 - \frac{V_{\alpha,i-1}}{V} - \frac{V_{\beta,i-1}}{V}\right)$, the total untransformed volume remaining at the end of the previous time interval. Combining equations 7.7 and 7.12, gives:

$$dV_{\alpha,i} = \left(1 - \frac{V_{\alpha,i-1}}{V} - \frac{V_{\beta,i-1}}{V}\right) \left[\frac{4\pi}{3} G_\alpha^3 I_\alpha V (\Delta t)^4 \left(1 + \sum_{j=0}^{i-1} [1 + 3(i-j)(i-j-1)]\right)\right] \quad (7.13)$$

The total volume of allotriomorphic ferrite present in the i-th time interval can be determined by addition of the change in the current time interval to the previous total:

$$V_{\alpha,i} = V_{\alpha,i-1} + dV_{\alpha,i} \quad (7.14)$$

Analogous calculations can be performed for the β phase.

Some example calculations which illustrate the fundamental theory are presented in Figure 7.1, showing the evolution of phase volume fraction with transformation time for isothermal transformation of two phases with constant nucleation and growth rates. When the nucleation and growth rates of α and β are set to be identical, the resulting curves

are exactly superimposed and the final volume fraction of each phase is 0.5 (Figure 7.1a). If the nucleation rate of α is set to be twice that of β then, for identical growth rates, the final fraction of α is twice that of β as would be expected (Figure 7.1b). Finally, an example where the nucleation rates of both phases are identical but the growth rate of α is twice that of β is given (Figure 7.1c). The final volume fraction of α is 8 times that of β because the growth rate is cubed in the volume fraction equation.

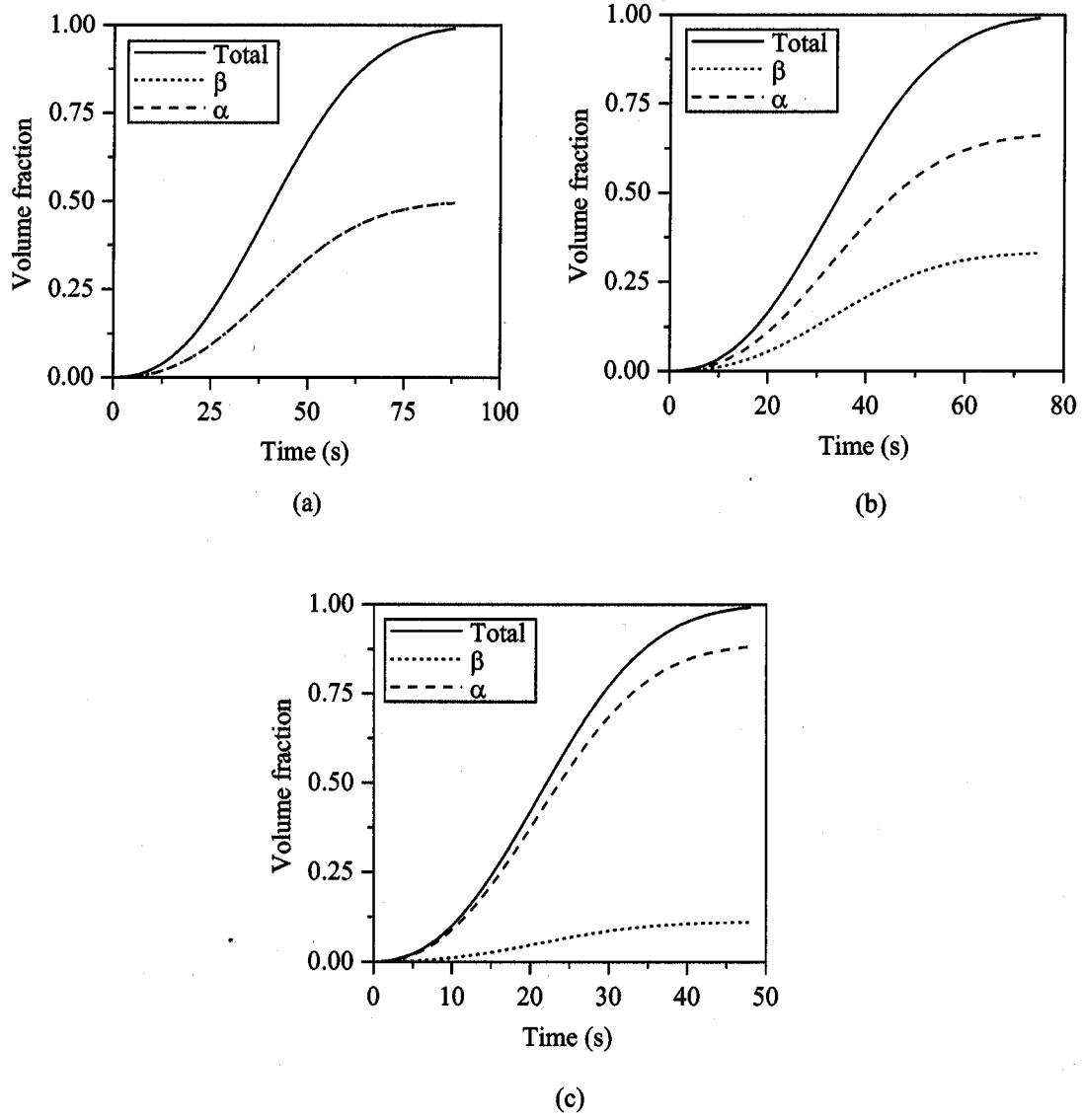

Figure 7.1: Example calculations for the simultaneous transformation kinetics of two phases, α and β, with (a) identical nucleation and growth rates, $I_\alpha = I_\beta = 1\times10^{14}$ m^{-3} s^{-1}, $G_\alpha = G_\beta = 1 \times 10^{-6}$ m s$^{-\frac{1}{2}}$ (b) identical growth rates but nucleation rate of α twice that of β, $I_\alpha = 2 \times 10^{14}$ m^{-3} s^{-1} and (c) identical nucleation rates but growth rate of α twice that of β, $G_\alpha = 2 \times 10^{-6}$ m s$^{-\frac{1}{2}}$.

7.2 Heterogeneous Nucleation

Just as the original single phase JMA theory could be extended to heterogeneous nucleation, so can the simultaneous transformation version. The change in extended area in each time interval is again composed of the contributions from the nucleation of new particles and the growth of previous nuclei. However, in this case, three nested loops are required for the calculation. The outer loop again allows changes in the overall transformation time, t. The second loop considers the set of planes, y_{iy}, (where the subscript iy denotes the specific plane under consideration), parallel to the plane containing the grain boundary, with which the intersections of particles growing from the boundary are calculated, whilst the innermost loop iterates for each incubation time, τ. Therefore, in each new time interval, the total extended volume is found by integrating, over all the planes, the transformed area on each plane due to new nuclei plus the growth of all particles nucleated in each previous time interval.

7.2.1 Linear Growth

Consider a disc-shaped particle, nucleated at time τ and growing at a constant rate G_α. Its height above the boundary at a later time t is:

$$q_\alpha = G_\alpha(t-\tau). \tag{7.15}$$

The rate of change of height with time is $\frac{dq_\alpha}{dt} = G_\alpha$. Therefore, the small change in q_α over the small time interval Δt from $t = (i-1)\Delta t$ to $t = i\Delta t$ is:

$$\begin{aligned} \int_0^{\Delta q_{\alpha,i}} dq_\alpha &= \int_{(i-1)\Delta t}^{i\Delta t} G_\alpha \, dt \\ \Delta q_{\alpha,i} &= G_\alpha[i\Delta t - (i-1)\Delta t] = G_\alpha \Delta t \end{aligned} \tag{7.16}$$

The area of intersection with a plane at y_{iy} for $q_{\alpha,i} \geq y_{iy}$, is $A_\alpha = \pi G_\alpha^2 (t-\tau)^2$. The change in area on the plane due to discs reaching it for the first time in the current time interval, *i.e.* for $q_{\alpha,i-1} < y_{iy}$, for $\Delta t = \Delta\tau$, is:

$$dO^e_{\alpha,i,iy} = \pi G_\alpha^2 O_b I_{\alpha,b} (\Delta t)^3 \tag{7.17}$$

The rate of change of area of intersection with time is $\frac{dA_\alpha}{dt} = 2\pi G_\alpha^2 (t-\tau)$. Proceeding as for equation 7.10, in the time interval from $(i-1)\Delta t$ to $i\Delta t$, at an incubation time $j\Delta\tau$, the small change in intersected area for particles which have previously reached the plane at y_{iy} is:

$$\begin{aligned}\int_0^{\Delta A_{\alpha,i}} dA_\alpha &= \int_{(i-1)\Delta t}^{i\Delta t} 2\pi G_\alpha^2 (t - j\Delta\tau)^2\, dt \\ \Delta A_{\alpha,i} &= \left[\pi G_\alpha^2 (t - j\Delta\tau)^2\right]_{(i-1)\Delta t}^{i\Delta t} \\ &= \pi G_\alpha^2 \left[(i\Delta t - j\Delta\tau)^2 - ((i-1)\Delta t - j\Delta\tau)^2\right] \\ &= \pi G_\alpha^2 [(2i-1)(\Delta t)^2 - 2j\Delta\tau\Delta t] \end{aligned} \tag{7.18}$$

If $\Delta t = \Delta\tau$ then:

$$\Delta A_{\alpha,i} = \pi G_\alpha^2 (\Delta t)^2 [2(i-j) - 1] \tag{7.19}$$

The change in extended area on the iy-th plane in the time interval from $t = (i-1)\Delta t$ to $t = i\Delta t$, due to particles nucleated at all incubation times from $\tau = 0$ to $\tau = (i-1)\Delta\tau$, with reference to equation 3.53 is thus:

$$\begin{aligned} dO^e_{\alpha,i,iy} &= O_b I_{\alpha,b}\, \Delta t \sum_{j=1}^{i-1} \Delta A_{\alpha,j} \\ &= \pi G_\alpha^2 O_b I_{\alpha,b}\, \Delta t \sum_{j=1}^{i-1} (2i-1)(\Delta t)^2 - 2j\Delta\tau\Delta t \\ &= \pi G_\alpha^2 O_b I_{\alpha,b} (\Delta t)^3 \sum_{j=1}^{i-1} 2(i-j) - 1 \end{aligned} \tag{7.20}$$

for $\Delta t = \Delta\tau$, where O_b is the total area of the plane and $I_{\alpha,b}$ is the nucleation rate of α per unit area of boundary. Therefore, the total change in extended area on the iy-th plane due to new particles and the growth of existing ones, for $q_{\alpha,i} \geq y_{iy}$, is:

$$dO^e_{\alpha,i,iy} = \pi G_\alpha^2 O_b I_{\alpha,b} (\Delta t)^3 \left[1 + \sum_{j=1}^{i-1} 2(i-j) - 1\right] \tag{7.21}$$

This change in extended area on a particular plane is converted into the actual change in area by allowing for the probability that some transformation has occurred in previously transformed material, taking into account the prior amount of all the other phases on this plane.

$$dO_{\alpha,i,iy} = \left(1 - \frac{O_{\alpha,i-1,iy}}{O_b} - \frac{O_{\beta,i-1,iy}}{O_b}\right) dO^e_{\alpha,i,iy} \tag{7.22}$$

The total actual area of α on the plane is then:

$$O_{\alpha,i,iy} = O_{\alpha,i-1,iy} + dO_{\alpha,i,iy} \tag{7.23}$$

Similar computations are performed on each plane for the other phases. After the calculations for all the planes have been completed, the total extended volume of α at the time

$i\Delta t$ can be determined by numerical integration of $O_{\alpha,i,iy}$ with respect to y_{iy}. The *change* in extended volume in the current time interval is found by subtracting the total extended volume at the end of the previous time interval from the new total:

$$dV^e_{\alpha,i} = V^e_{\alpha,i} - V^e_{\alpha,i-1} \tag{7.24}$$

and thus the actual change in volume is:

$$dV_{\alpha,i} = \left(1 - \frac{V_{\alpha,i-1}}{V} - \frac{V_{\beta,i-1}}{V}\right) dV^e_{\alpha,i} \tag{7.25}$$

The total actual volume of α at the end of the current time interval is given by:

$$V_{\alpha,i} = V_{\alpha,i-1} + dV_{\alpha,i} \tag{7.26}$$

and similarly for the other phases. This whole process is then iterated for subsequent time intervals until the transformation is stopped or completed.

7.2.2 Parabolic Growth

Now consider particles growing parabolically rather than linearly with time, such as allotriomorphic ferrite grains from austenite. For a disc-shaped particle of aspect ratio (for lengthening to thickening) η_α, the radius of a particle nucleated at τ at a later time t is given by:

$$r_\alpha = \eta_\alpha G_\alpha (t-\tau)^{\frac{1}{2}} \tag{7.27}$$

The height is expressed by the same equation but with $\eta_\alpha = 1$:

$$q_\alpha = G_\alpha (t-\tau)^{\frac{1}{2}} \tag{7.28}$$

The rate of change of height is:

$$\frac{dq_\alpha}{dt} = \frac{1}{2} G_\alpha (t-\tau)^{-\frac{1}{2}} \tag{7.29}$$

The small change in height, Δq_α in the small time interval from $(i-1)\Delta t$ to $i\Delta t$ of a particle nucleated at $j\Delta\tau$ is given by:

$$\begin{aligned} \int_0^{\Delta q_{\alpha,i}} dq_\alpha &= \int_{(i-1)\Delta t}^{i\Delta t} \frac{1}{2} G_\alpha (t-\tau)^{-\frac{1}{2}}\, dt \\ \Delta q_{\alpha,i} &= G_\alpha \left[(i\Delta t - j\Delta\tau)^{\frac{1}{2}} - ((i-1)\Delta t - j\Delta\tau)^{\frac{1}{2}} \right] \end{aligned} \tag{7.30}$$

The area of intersection with a plane at y_{iy} for a disc of height greater than y_{iy} is:

$$A_\alpha = \pi r_\alpha^2 = \pi \eta_\alpha^2 G_\alpha^2 (t-\tau) \tag{7.31}$$

The rate of change of area is:

$$\frac{dA_\alpha}{dt} = \pi\eta_\alpha^2 G_\alpha^2 \tag{7.32}$$

Thus, in the small time step $t = (i-1)\Delta t$ to $t = i\Delta t$, for particles nucleated at $\tau = j\Delta\tau$,

$$\begin{aligned} \Delta A_{\alpha,i} &= \left[\pi\eta_\alpha^2 G_\alpha^2 (t - j\Delta\tau)\right]_{(i-1)\Delta t}^{i\Delta t} \\ &= \pi\eta_\alpha^2 G_\alpha^2 \Delta t \end{aligned} \tag{7.33}$$

Unlike the case for linear growth, $\Delta A_{\alpha,i}$ is independent of both i and j when Δt is constant. (When Δt is not constant, $\Delta A_{\alpha,i} = \pi\eta_\alpha^2 G_\alpha^2 [t_i - t_{i-1}]$). Therefore, the total change in extended area on the iy-th plane in the i-th time interval is:

$$\begin{aligned} dO^e_{\alpha,i,iy} &= O_b I_{\alpha,b} \Delta t \Delta A_{\alpha,i} \\ &= O_b I_{\alpha,b} \pi G_\alpha^2 (\Delta t)^2 \end{aligned} \tag{7.34}$$

The total area transformed on each plane and the overall volume of α formed are then determined as for linear growth.

7.3 Application to the Transformation of Austenite

In the new transformation model, allotriomorphic ferrite, Widmanstätten ferrite and pearlite were modelled with the simultaneous transformation theory as explained above, replacing the single phase JMA kinetics theory discussed for each phase in Chapter 6. Figure 7.2 illustrates the particle dimensions for these three phases. The theory for the bainite transformation is similar, but due to differences in its growth mechanism further modifications were necessary. The contributions to the overall transformation from each phase were combined at the extended area and extended volume stages of the transformation. The martensite transformation was calculated simply as a function of the undercooling below the martensite start temperature. In the low-alloy steels that are of particular interest here, it is the last phase to form and transformation of the other phases can be considered to cease once the M_s is reached. Thus, a simultaneous kinetics approach was not required for martensite.

7.3.1 Allotriomorphic Ferrite

The allotriomorphs were modelled as discs, growing parallel to the boundary plane, with an aspect ratio for lengthening to thickening of 3:1 [35, 36]. The equations in Section 7.2.2 therefore apply, with G_α replaced by α_1, the one-dimensional parabolic rate thickening constant, and $\eta_\alpha = 3$. Allotriomorphic ferrite grows from both sides of the grain boundaries

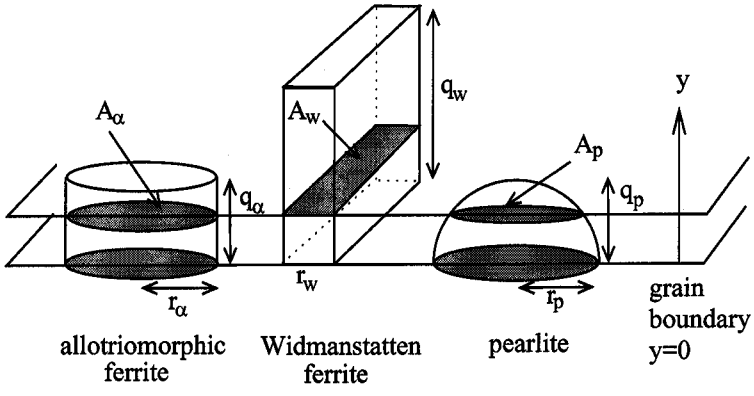

Figure 7.2: Illustration of the particle shapes and dimensions for allotriomorphic ferrite, Widmanstätten ferrite and pearlite used in the transformation model.

so the result of the integration of $O_{\alpha,i,iy}$ over y_{iy} was doubled when calculating the extended volume.

7.3.2 Widmanstätten Ferrite

Widmanstätten ferrite was modelled as plates growing at a constant rate from the austenite grain boundaries. The equations of Section 7.2.1 were adapted for the plate morphology. Consider a plate of aspect ratio η_w, (where η_w is typically 0.05), its height given by $q_w = G_w(t-\tau)$ and its width by $r_w = \eta_w q_w$. The area of intersection of one plate with a plane parallel to the boundary is $A_w = r_w q_w = \eta_w G_w^2 (t-\tau)^2$. By analogy with equation 7.19 this gives:

$$\Delta A_{w,i} = \eta_w G_w^2 (\Delta t)^2 [2(i-j)-1] \tag{7.35}$$

for the small change in A_w between $t = (i-1)\Delta t$ and $t = i\Delta t$ for particles nucleated at $\tau = j\Delta\tau$, when $\Delta\tau = \Delta t$. The change in extended area on the iy-th plane in the i-th time interval due to particles nucleated in all previous time intervals is then:

$$dO^e_{w,i,iy} = \eta_w G_w^2 O_b I_{w,b} (\Delta t)^3 \sum_{j=1}^{i-1} 2(i-j) - 1 \tag{7.36}$$

The rest of the equations follow as before.

7.3.3 Pearlite

As in the original model, the pearlite grains were taken to be hemispheres with a linear growth rate, which intersect the plane at y_{iy} in discs of area:

$$A_p = \pi(r_p^2 - y_{iy}^2) = \pi(G_p^2(t-\tau)^2 - y_{iy}^2) \tag{7.37}$$

Proceeding as in 7.2.1, we find that:

$$\Delta A_{p,i} = \pi G_p^2(\Delta t)^2[2(i-j)-1] \tag{7.38}$$

which is the same as for discs (equation 7.19), and the rest of the equations follow accordingly.

7.3.4 Bainite

The existing bainite overall kinetics model was adapted for simultaneous transformations. The change in the actual volume of bainite in each time step, dV_{α_b}, was calculated as before but with the factor $(1-\xi_{\alpha_b})$ replaced by $(1-\xi)$, where ξ represents the *total* extent of transformation to all phases not just bainite, *i.e.* $\xi = \xi_\alpha + \xi_{\alpha_w} + \xi_p + \xi_{\alpha_b}$, where the ξ_n represent the absolute fraction of each phase n. This is to allow for the fact that a lot of the austenite will have been consumed by the time bainite begins to form. Thus from equation 4.32,

$$dV_{\alpha_b} = \theta_{\alpha_b} d\xi_{\alpha_b} = uK_1(1-\xi)(1+\beta\theta_{\alpha_b}\xi_{\alpha_b})I_{\alpha_b}\,dt \tag{7.39}$$

Bainite, in common with the other phases, often nucleates heterogeneously at the austenite grain boundaries. The original model only considered random nucleation of bainite sheaves within the volume, so a new model for boundary nucleation was developed. The inverse grain size dependence of the bainite nucleation rate (equation 4.18) is consistent with boundary nucleation (smaller grain size leads to a larger available boundary area per unit volume and thus a higher nucleation rate). The theory had to be modified to calculate an extended area of transformation from which to determine the extended volume. The bainite sub-units were assumed to be plates, of width 0.2 μm modified by the temperature dependence $(T-528)/150$ (where T is the absolute temperature) [121], and length 10 μm. The number of sub-units nucleated in each time interval was given by:

$$N_{\alpha_b} = I_{\alpha_b} O_b\,dt \tag{7.40}$$

where O_b is the total boundary area. It was assumed that each sub-unit attained its full size almost instantaneously, due to the high growth rate of bainite. The bainite sheaves were built up by successive autocatalytic nucleation of sub-units and their length was increased

in each time interval if the bainite nucleation and growth criteria were satisfied. Therefore, there was no need for the autocatalysis factor in the nucleation rate equation ($\beta = 0$) – the nucleation rate only concerned new sheaves starting on the boundary, whilst existing sheaves were automatically allowed to continue growing by addition of a new sub-unit to every existing sub-unit in each time interval. The height of the sheaves was compared with the distances y_{iy} of a series of parallel planes from the grain boundary. When the sheaf height first exceeded y_{iy} then the area of its intersection with the plane was added to the total extended area previously transformed on that plane. The cross-sectional area of each sub-unit was taken as the width times length,

$$A_{\alpha_b} = 0.2 \times 10^{-6} \frac{(T - 528)}{150} \times 10.0 \times 10^{-6} \quad \mathrm{m}^2 \tag{7.41}$$

and did not increase with time. Thus, the total increase in extended area of bainite on one plane in the time interval from $t = (i-1)\Delta t$ to $t = i\Delta t$ was:

$$dO^e_{\alpha_b} = \sum_{j=0}^{i} A_{\alpha_b} N_{\alpha_b,j} \tag{7.42}$$

where the summation over j allows for growth of sheaves nucleated in all previous time intervals. The total change in extended volume in one time interval was determined by integrating $dO^e_{\alpha_b}$ over all y_{iy}. This was then converted to the real volume as for the other phases, allowing for the probability that some of the transformation had occurred in previously transformed material, and thus multiplying by $(1 - \xi)$.

7.4 Summary

A recent adaptation of the Johnson-Mehl-Avrami overall transformation kinetics theory which enables the simultaneous transformation of multiple phases has been described. Equations for both homogeneous and heterogeneous nucleation and their application to transformations from austenite have been explained. Allotriomorphic ferrite was modelled by the parabolic growth of discs, Widmanstätten ferrite by linear growth of plates and pearlite by linear growth of hemispherical particles. The bainite sub-unit model was adapted to fit into the simultaneous framework and modified for boundary nucleation. Validation of these models will be considered in a following chapter.

The above equations were derived assuming isothermal transformation kinetics. Under non-isothermal conditions, where the growth and nucleation rates differ at each time interval, the current radius or height of the particles must be used to determine the change in area and volume in each interval, rather than G_α and $t - \tau$ directly.